Modelling And Design Optimization of Compound Thick-Walled Cylinders Treated with Autofrettage, Shrink-Fit, And Wire-Winding Processes

Mohamed Ghanem Youssef Elfar

A Thesis
In The department
of
Mechanical and Industrial Engineering

Presented in Partial Fulfillment of the Requirements
for the Degree of
Doctor of Philosophy (Mechanical and Industrial Engineering) at
Concordia University
Montreal, Quebec, Canada

November 2023

CONCORDIA UNIVERSITY
SCHOOL OF GRADUATE STUDIES

This is to certify that the thesis prepared

By: Mohamed Elfar

Entitled: **Modelling and Design Optimization of Compound Thick-Walled Cylinders Treated with Autofrettage, Shrink-Fit, And Wire-Winding Processes**

and submitted in partial fulfillment of the requirements for the degree of

DOCTOR OF PHILOSOPHY (Mechanical Engineering)

complies with the regulations of the University and meets the accepted standards with respect to originality and quality.

Signed by the final examining committee:

_____ Chair
Dr.

_____ Examiner
Dr. Kamran Behdinan

_____ Examiner
Dr. Khaled Galal

_____ Examiner
Dr. Ion Stiharu

_____ Examiner
Dr. Farjad Shadmehri

_____ Thesis Supervisor
Dr. Ramin Sedaghati

Approved by _____
Dr. Muthukumaran Packirisamy
Graduate Program Director

_____
Dr. Mourad Debbabi,
Dean Gina Cody School of Engineering and Computer Science

Date November 2023

ABSTRACT

Modelling And Design Optimization of Compound Thick-Walled Cylinders Treated with Autofrettage, Shrink-Fit, And Wire-Winding

Mohamed Ghanem Elfar, Ph.D.
Concordia University, 2023

Thick-walled cylinders are crucial in various industrial applications, including mechanical, aerospace, naval, offshore, petrochemical, military, and electronics industries. These cylinders function as pressure vessels in diverse structures under different loading conditions. Some applications, such as steam boilers and aerospace propulsion systems, encounter severe cyclic thermo-mechanical loading conditions. Modeling the impact of these cyclic conditions is challenging due to the limited time between successive loads, preventing adequate cooling and resulting in thermal accumulation within the cylinder material. Thus, stress and temperature distributions within the cylinder thickness are altered, affecting mechanical and thermal properties. Existing models commonly assume temperature-independent material properties, utilizing the uncoupled thermo-elasticity approach. However, it is essential to adopt temperature-dependent material properties and a coupled thermo-elasticity approach for a precise estimation of residual temperature and stress distributions throughout the cylinder wall, significantly influencing thick-walled cylinder design.

Moreover, under severe loading conditions, simple virgin cylinders may fail to sustain applied loads without undesirable increases in thickness and weight. Consequently, various surface treatment manufacturing processes, such as shrink-fitting, wire-winding, and autofrettage, have been developed to enhance durability and load-bearing capacity. These processes induce beneficial compressive stresses near the bore region, countering tensile stresses that would normally develop during loading, thus improving their fatigue lifetime. Accurate prediction of residual stresses resulting from these processes is pivotal for optimal cylinder design. However, due to several limitations associated with each individual reinforcement process, different combinations of reinforcement processes are proposed to alleviate these limitations. Estimating residual stresses due to such combinations is complicated, leading many studies to avoid analytical models.

In response to these challenges, this thesis explores the behavior of temperature-dependent thick-walled cylinders treated with various reinforcement processes under cyclic thermomechanical loads. The classical coupled thermo-elasticity approach estimates thermal and mechanical responses, highlighting the significance of considering temperature-dependent material properties. Furthermore, an efficient analytical method is developed for estimating the residual stress profiles in cylinders with diverse reinforcement processes. This method forms the basis for a machine learning-based design optimization, streamlining the process and reducing computational costs significantly. Fatigue life assessment of the optimal configuration underscores the improvement achieved.

DEDICATION

Dedicate this dissertation to my parents, my kids, and my wife.

Acknowledgment

First and foremost, I would like to praise Allah the Almighty, the Most Gracious, and the Most Merciful for His blessing given to me during my study and in completing this thesis.

After finishing my thesis, I've found that the most challenging part is writing the acknowledgements because there are so many more things to include than just the technical details. There are many people to thank, but there is not enough room here. I owe a massive thank you to my thesis supervisor, Prof. Ramin Sedaghati. Being a part of his research group has been an incredible journey. He's been patient, motivating, and super supportive, providing me with crucial guidance and a wealth of knowledge. His encouragement has been my driving force, and his feedback has helped me dive deeper into my research, polish my writing, and really level up my work. I truly look up to him and feel blessed to have had such an inspiring mentor.

A big shoutout also goes to the Egyptian government; their financial support made it possible for me to chase my graduate school dreams at Concordia University in Canada, and I can't thank them enough for that.

I want to give a virtual high-five to my local supervisor, Dr. Ossama Ramy, for being a constant source of support and sharing valuable insights throughout my research journey. And let's not forget the awesome professors at the Military Technical College in Cairo, Egypt. They've been like academic superheroes, setting me up with a strong foundation for both undergrad and graduate studies and helping me thrive in this thesis program.

Finally, a big thank you to my family for always supporting me, understanding me, and encouraging me all the time. They mean a lot to me.

Table of Contents

LIST OF FIGURES

LIST OF TABLES

NOMENCLATURE

$\sigma_{T\theta}$	Resultant hoop stress	p^*	Permissible pressure
p_i	Internal pressure	α	Wall ratio
ε_r	Radial strain	ε_θ	Hoop strain
ε_z	Axial strain	γ_{ij}	Shear strain
σ_r	Radial stress	σ_θ	Hoop stress
E	Young modulus of elasticity	υ	Poisson's ratio
α	Thermal expansion	T	Temperature
$\ddot{u}_r$	Radial acceleration	r	Radial position
ρ	Density	v	Stress wave velocity
q_r	Heat flux vector in the radial direction	T_o	Reference temperature
k	Thermal conductivity	S	Entropy
C	Specific heat	t	Time
α^*	Thermal diffusivity	h_f	Flow convection coefficient
T_f	Flow temperature	p_f	Flow pressure
h_∞	Free convection coefficient,	T_∞	Ambient temperature
p_∞	Ambient pressure	u_r	Radial displacement
σ_r	Radial stress	σ_θ	Hoop stress
ε_{eq}^p	Plastic equivalent strain	ε_θ^p	Plastic hoop strain
σ_{eq}	Equivalent stress	σ_Y	Yield strength
E_P	Plastic modulus	R_i	Inner radius
R	Interface radius between the two layers	R_o	Outer radius
δ	Shrink-fit clearance	R_w	Outer radius of the wounded layer
$\sigma_{\theta W}$	Winding hoop stress	t_w	Wire thickness
Y	Objective function	t_1	Inner layer thickness
p_s	Shrink-fit pressure	R_c	Elastoplastic radius
$\bar{p}_x$	Critical shrink-fit pressure	G_{0-3}	Free surface correction factors
C_f	Crack growth rate factor	m_f	Crack growth rate factor
K_I	Stress Intensity Factor	R_K	Stress intensity ratio
ΔK_I	stress intensity factor range		

CHAPTER 1

INTRODUCTION

This dissertation aims to study the behaviour of thick-walled cylinders under cyclic nonlinear thermomechanical loads. The primary purpose of this chapter is to introduce the reader to the research topic. It begins with a brief background on thick-walled cylinders and their practical applications. Subsequently, it outlines the motivation behind this research, along with the specific aims, objectives, and contributions to knowledge that this dissertation seeks to make. Then, a comprehensive literature review is presented, critically analyzing the existing studies and identifying research gaps in the field of thick-walled cylinders subjected to cyclic nonlinear thermomechanical loads. This literature review serves as a solid foundation for the subsequent chapters, enabling a better understanding of the research's originality and significance. Lastly, an overview of the subsequent chapters' organization is provided, giving a clear structure to the overall dissertation.

1.1 Background

The history of thick-walled cylinder technology traces its roots back to the early 14^{th} century, when Berthold Schwarz, a German scientist, made a groundbreaking invention—the gun [1]. This marked a significant milestone in the practical application of thick-walled cylinders as a means to contain high-pressure forces. For several centuries, the gun remained the only example of utilizing thick-walled cylinders to withstand severe pressure.

However, as industrialization progressed and technology advanced, the practical applications of thick-walled cylinders expanded exponentially. In today's contemporary world, these robust structures find widespread use across various industries, playing a crucial role in ensuring the safety and efficiency of critical processes.

One such realm where thick-walled cylinders have become crucial is the petrochemical industry. In petrochemical plants, these cylinders are employed in a range of applications, including high-pressure storage tanks for flammable liquids and gases. The ability of thick-walled cylinders to withstand the severe pressure and temperature variations prevalent in these

environments makes them an ideal choice for ensuring the safe containment of hazardous substances.

Moreover, thick-walled cylinders have also become integral components in the automotive and transportation sectors. In the automotive industry, they serve as pressure vessels in hydraulic systems, pneumatic systems, and air compressors. These cylinders play a crucial role in providing reliable and efficient power transmission in various vehicle mechanisms, ranging from braking systems to suspension components.

Furthermore, the significance of thick-walled cylinders extends into the realm of nuclear power plants. These critical facilities, responsible for generating clean and sustainable energy, require pressure vessels that can endure the extreme conditions present within the reactors. Thick-walled cylinders play a vital role in the containment of high-pressure nuclear coolant and are designed to withstand the challenging thermal and mechanical loads experienced during reactor operation.

In these diverse applications, thick-walled cylinders face arduous dynamic loading conditions. The design and engineering of modern thick-walled cylinders for these specific uses revolve around maximizing their load-bearing capacity and fatigue life while optimizing their size and weight. Engineers must consider factors such as material selection, manufacturing processes, and safety standards to ensure the structural integrity and reliability of these cylinders under repetitive harsh loading conditions.

In conclusion, the journey of thick-walled cylinder technology from its humble beginnings with Berthold Schwarz's gun to its present-day popularity in various industrial applications exemplifies its enduring significance in engineering and technology. As industries continue to evolve, so will the development and implementation of these robust structures to meet the ever-growing demands of modern engineering challenges.

1.2 Motivation and Statement of the Problem

Structures like steam boilers in power plants, aerospace propulsion tanks, machine gun barrels, and nuclear reactors are generally subjected to repeated thermo-mechanical loads. These structures have limited time for cooling between cycles, resulting in thermal accumulation within the cylinder

material. As a consequence, there are variations in stress, temperature distributions, and material characteristics through the cylinder's wall. Also, designing such structures is a complex task as it involves considering coupled multi-physics design considerations in addition to considering the nonlinear response of materials to mechanical and thermal loads. Additionally, there is a renewed interest in understanding stress distribution within thick-walled cylinders due to the harsh loading conditions they endure. Accurately predicting the response behaviour of thick-walled cylinders under their loading conditions is of paramount importance for the optimal design of reliable cylinders with enhanced fatigue life.

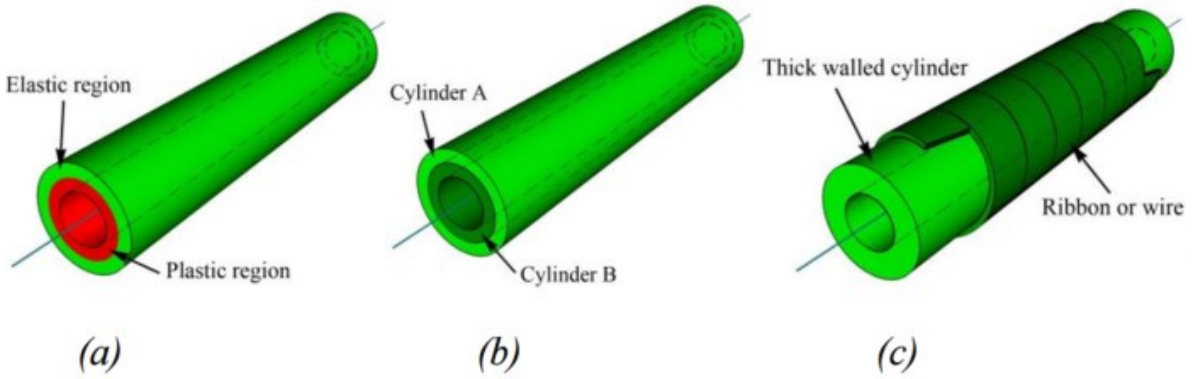

Figure 1-1. Methods of strengthening thick-walled cylinders, (a) Autofrettage thick-walled cylinder, (b) Shrink-fit two-layers cylinder, and (c) Wire-wounded thick-walled cylinder [2].

Under repeated harsh thermo-mechanical loading conditions, virgin monoblock thick-walled cylinders are unable to withstand the applied load effectively. Consequently, researchers have introduced innovative manufacturing processes to reinforce thick-walled cylinders, such as shrink-fit, wire-winding, and autofrettage processes (as shown in Figure 1-1). These processes aim to increase safe bearing capacities, extend the lifetime, and improve durability. By combining these reinforcement techniques, the distribution and magnitude of residual stresses are controlled, leading to enhanced mechanical properties and overall performance of the thick-walled cylinders.

In this research field, optimizing the design of thick-walled cylinders and accurately assessing their fatigue life under cyclic nonlinear thermo-mechanical loads are crucial aspects. Achieving an optimal residual stress profile through the cylinder wall using the appropriate combination of reinforcement processes is essential for enhancing the overall performance. As various combinations of reinforcement processes influence stress distribution and subsequently impact

fatigue behaviour, thus, accurate assessment of the fatigue life under repeated thermo-mechanical loads is of utmost importance to select the optimum design.

In conclusion, the challenges in the design and analysis of thick-walled cylinders under repeated harsh thermo-mechanical loading demand further exploration in this research field. Accurate modelling and prediction techniques are essential due to the complexities arising from factors such as thermal accumulation, stress and temperature variations, and material behaviour. Future work in this area should focus on leveraging state-of-the-art methodologies related to optimization to investigate the best combinations of reinforcement processes for optimizing the design and enhancing the overall performance of thick-walled cylinders. Addressing these challenges will lead to significant advancements in the field of thick-walled cylinder design, ultimately contributing to improved structural integrity, durability, and safety in various engineering applications.

1.3 State of the Art

The most crucial characteristics of contemporary thick-walled compound cylinders that operate in harsh thermo-mechanical conditions are their ability to safely withstand these demanding loads for a long time with a small wall thickness compared to their virgin monobloc counterpart. That's why it's crucial to strengthen these cylinders by adding beneficial compressive stresses near their bore before they go into service. Different methods like wire winding, shrink-fit, and autofrettage are effectively used to induce these beneficial compressive stresses and therefore improve the load-bearing capacity and fatigue life of thick-walled cylinders.

The wire-winding process generates compressive stress near the bore region by wrapping wire around the outer surface of the cylinder. In the shrink-fit process, the outer layer compresses the inner layer, generating compressive stress near the bore region. Unlike wire-winding and shrink-fit, the autofrettage process involves overloading the bore of a thick-walled cylinder, leading to permanent deformation near the bore region. After removing the load, the elastic recovery of the outer part creates a compressive residual stress near the bore area. Besides accurate evaluation of induced residual stress distribution due to reinforcement processes, it is essential to accurately evaluate the response of compound cylinders under their loading conditions to verify the effectiveness of such surface treatments.

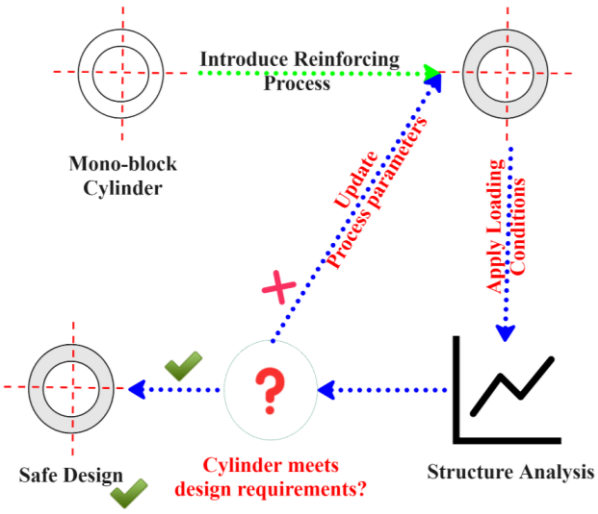

Figure 1-2. Flow chart for the thick-walled cylinder design

Numerous studies have focused on determining the residual stress distribution across the wall of thick-walled cylinders that have been treated with either wire winding, shrink-fit, autofrettage, or a combination of them. Then, the response of thick-walled cylinders subjected to thermo-mechanical loading conditions is estimated based on the thermo-elasticity theory. It is worth noting that the common flow of work for these studies typically follows the procedure depicted in Figure 1-2, in which a thick-walled cylinder is analyzed to investigate if it satisfies the design requirements after introducing the compressive stresses.

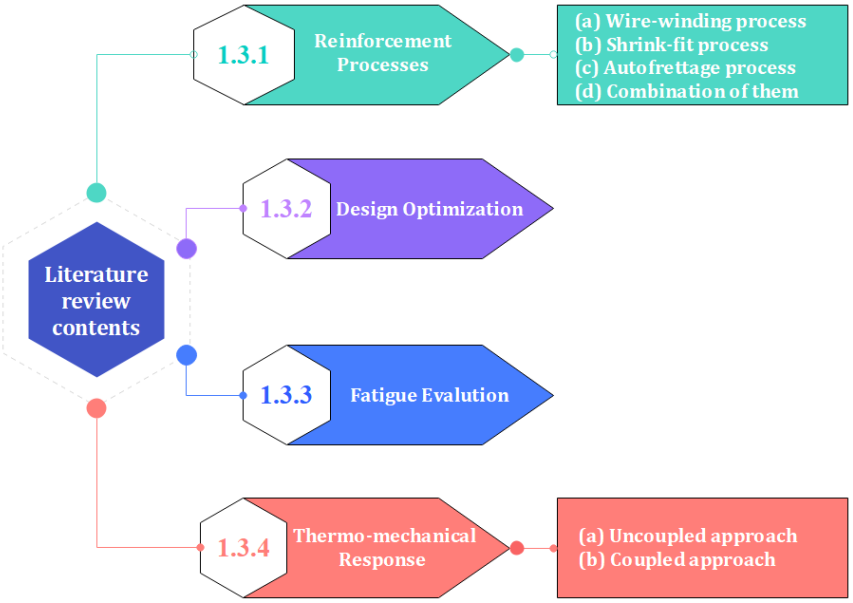

Figure 1-3. Structure of the literature review.

To establish a comprehensive theoretical foundation and define the boundaries of this dissertation research, an extensive examination of relevant studies has been conducted. A systematic review of these studies has been undertaken to gather essential knowledge and gain a clear understanding of the research scope. The findings of these reviewed studies, which have been categorized according to their respective topics, are presented in four distinct sections: 1.3.1, 1.3.2,1.3.3, and 1.3.4, as depicts in Figure 1-3.

In Section 1.3.1, the reinforcement processes employed in manufacturing thick-walled cylinders are explored, encompassing a) the wire-winding process, b) the shrink-fit process, c) the autofrettage process, and d) combination of reinforcement processes. Section 1.3.2 addresses the optimization of thick-walled cylinder designs through the integration of these processes to attain the most favourable configuration, aiming to improve their fatigue life performance. Then, the fatigue life evaluation of the thick-walled cylinder under various loading conditions is discussed in section 1.3.3. Lastly, Section 1.3.4 examines the modelling and analysis of thick-walled cylinders under thermal and mechanical loads using thermo-elasticity theory, which can be approached in two distinct manners: a) the uncoupled approach, or b) the coupled approach.

1.3.1 Reinforcement processes

Simple metallic monoblock thick-walled cylinders, made of a single-layer material, have been widely used in different applications since the 14th century. The initial design of these thick-walled cylinders relied on trial and error, but in the 18th century, Lame´ and Clapeyron introduced a theoretical approach to calculate the elastic stresses for thick-walled cylinders under simple mechanical loads [3]. Then, researchers in the 19th century used this approach to design monoblock cylinders under thermo-mechanical loading conditions, replacing thermal loads with a particular safety factor estimated empirically based on the experimental data.

The Lame´ approach provides formulas to calculate the resultant hoop stress ($\sigma_{T\theta}$) and load-carrying capacity or the permissible pressure (p^*) for thick-walled cylinders with an open end under internal pressure (p) [3]. The equations can be expressed in terms of wall ratio ($\alpha = R_o/R_i$) and allowable material strength (σ_{all}) as:

$$\sigma_{T\theta} = \frac{2}{3}p\left(\frac{2+\alpha^{-2}}{1-\alpha^{-2}}\right) \tag{1-1}$$

$$p^* = \frac{3}{2}\sigma_{all}\left(\frac{1-\alpha^{-2}}{2+\alpha^{-2}}\right) \tag{1-2}$$

According to Eq. (1-2), to enhance the load-carrying capacity of the cylinder, one has two options: selecting a stronger material and/or increasing the wall thickness ratio. Figure 1-4 depicts the variation of the normalized permissible load-carrying capacity (p^*/σ_{all}) and the thick-walled cylinder weight ratio with respect to the wall ratio.

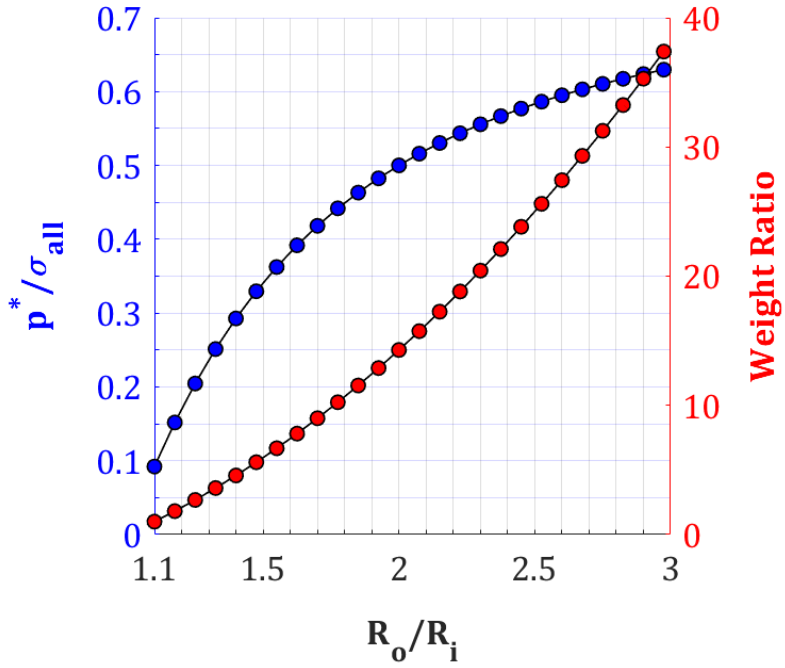

Figure 1-4. Variation of permissible pressure and weight ratio with wall ratio.

The weight ratio is defined as the cylinder weight divided by the reference weight, where the reference weight corresponds to the lower wall ratio of the thick-walled cylinder at α=1.1. The load-carrying capacity of the cylinder exhibits a non-linear increase with increasing wall ratio, as observed in Figure 1-4. However, the rate of increase diminishes beyond a wall ratio of 2.7 demonstrating the saturation of the load-carrying capacity at a high wall ratio. Conversely, the weight ratio shows a rapid rise in response to increasing wall ratio. For example, a wall ratio increases from 1.1 to 2.7 results in a 500% growth in load-carrying capacity while 3400% increase in weight ratio. Further increasing the ratio to 3 yields a slight rise of approximately 3% in load capacity, accompanied by an approximate 26% increase in weight ratio. In other words, according

to Equation (1-2), as the outer radius approaches infinity, the maximum permissible pressure approaches $0.75\ \sigma_{all}$, while the weight ratio approaches infinity.

In light of the aforementioned observations, it becomes clear that achieving a higher load-carrying capacity in monoblock thick-walled cylinders requires a significant increase in cylinder weight. As a result, the practical applications of monoblock cylinders in severe thermo-mechanical loading conditions are severely limited, as they would need to be excessively bulky to withstand such harsh environments. To address these limitations, researchers have introduced various reinforcement processes during the manufacturing of thick-walled cylinders, including shrink-fit, wire-winding, autofrettage, or a combination of them. These processes are employed in thick-walled cylinders to induce beneficial residual stresses near the bore area, aiming to enhance the load bearing capacity and fatigue life without significantly increasing the weight.

a) The wire-winding process

The wire-winding process is a safe and efficient technique employed for the reinforcement and strengthening of thick-walled cylinders. This method involves the encircling of a steel wire around the thick-walled cylinder, resulting in the development of residual compressive stresses near the inner surface. These compressive stresses effectively mitigate the impact of tensile stress induced by external loads, consequently enhancing the overall structural performance [4, 5]. Moreover, this process can be customized to meet specific engineering requirements and is suitable for both manufacturing new cylinders or improving existing structures.

Earlier studies often oversimplified the estimation of residual stress distribution in wire-wound thick-walled cylinders. This simplification involved assuming a constant tensile stress for all wire layers during the winding process. Consequently, the wire-winding process was reduced to a simple boundary condition that directly impacted the outer surface of the thick-walled cylinder. This simplification facilitated estimating the residual stress profile throughout the cylinder wall. However, it is important to acknowledge that this approach may lead to an overestimation of the generated residual stress and might not provide an entirely accurate representation of the actual induced residual stress distribution [6].

To overcome this limitation, Young [6] introduced a novel approach that involved calculating the wire tension for each layer during the winding process. This alternative approach provided a more accurate estimation of the residual stress distribution across the cylinder wall. Further improving wire-winding techniques, Maksimov [7] proposed the concept of the constant maximum shear stress theory. In a related area, Harkegard [8] presented a comprehensive procedure for analyzing and designing wire-wound pressure vessels. This procedure enabled a thorough evaluation of structural integrity and performance, leading to enhanced design outcomes.

Exploring alternative perspectives, Talako [9] introduced a new hypothesis that treated the cylindrical steel core as a thick-walled vessel and considered the wire layers as a thin-walled vessel. This approach yielded a deeper understanding of the structural behaviour and interactions between different components. Additionally, Fryer and Havery [10] employed Lame's relations and treated the wire-wound vessel as a multi-layer structure with substantial wall thickness. By comprehensively considering the vessel's characteristics and material properties, valuable insights into its overall performance were obtained.

Building upon these theoretical frameworks and design principles, the American Society of Mechanical Engineers (ASME) Code Section VIII Division 3, Article KD-9 [11] plays a crucial role in providing well-defined design requirements for high-pressure wire-wound vessels. These requirements encompass various aspects, including material selection, manufacturing processes, and structural analysis, ensuring the safety and reliability of wire-wound vessel designs.

Song et al. [12] conducted a finite element analysis to investigate the behaviour of wire-winding frames. This detailed numerical analysis enabled a comprehensive understanding of the structural response under different loading conditions, facilitating informed design decisions. In the field of simulation and virtual experimentation, Alegre et al. [13] proposed a simulation procedure specifically designed for high-pressure wire-wound vessels. This procedure utilized advanced computational techniques to simulate the structure's behaviour, enabling accurate predictions of its performance and durability. Furthermore, in another study, Alegre et al. [14] employed the ASME-API 579 [15] procedure for fatigue design of wire-wound pressure vessels. By integrating established industry standards, this approach ensured the robustness and reliability of the fatigue design process, ultimately enhancing the overall structural integrity.

In conclusion, the wire-winding process offers a safe and effective method for reinforcing and prestressing thick-walled cylinders. The development of various theories, analytical procedures, simulation techniques, and design standards has significantly contributed to the understanding, optimization, and reliable design of wire-wound thick-walled structures. By utilizing these advancements, engineers can confidently design and fabricate wire-wound thick-walled cylinders that meet tough safety requirements while demonstrating superior performance and durability.

b) Shrink-fit process

The shrink-fit process, known as compounding, is widely employed in the manufacturing of thick-walled cylinders due to its cost-effectiveness and simplicity. This technique involves the assembly of two or more virgin layers of relatively small thickness, creating an interference fit. During this process, the inner layer is placed under compression by the outer layer, resulting in the generation of beneficial compressive residual stresses near the bore of the compound cylinder. These residual stresses play a crucial role in enhancing the load-carrying capacity of the cylinder.

Several previous studies have extensively investigated the stress distribution within multi-layer shrink-fitted thick-walled cylinders [16– 25]. These studies have revealed that compounded thick-walled cylinders can exhibit either purely elastic or elastic-plastic material behaviour according to their shrinking interference. When dealing with purely elastic materials, researchers have explored stress distribution in a two-layer shrink-fitted thick-walled cylinder using the Lame´ approach. One such study, conducted by Pedersen [26], graphically illustrates the internal hoop and radial stress distribution within the wall of a compound thick-walled cylinder resulting from the shrink-fit process, as depicted in Figure 1-5. Furthermore, the study explored the stress distribution of the compound cylinder when subjected to internal pressure of 200 MPa. This analysis is illustrated in Figure 1-6.

It is noted that when shrinking interference is sufficiently large, the induced stress in the compound cylinder approaches the yield limit, rendering the Lame' elastic equations no longer valid for the yield region. In such cases, previous studies [27– 30] have addressed the stress distribution in an elastic-plastic shrink-fitted cylinder using different yielding approaches.

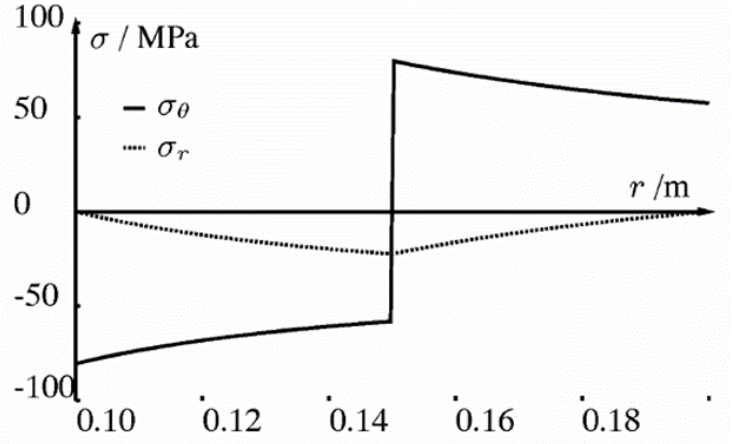

Figure 1-5. Residual stresses distribution through the compound cylinder wall due to shrink-fit interference only [26]

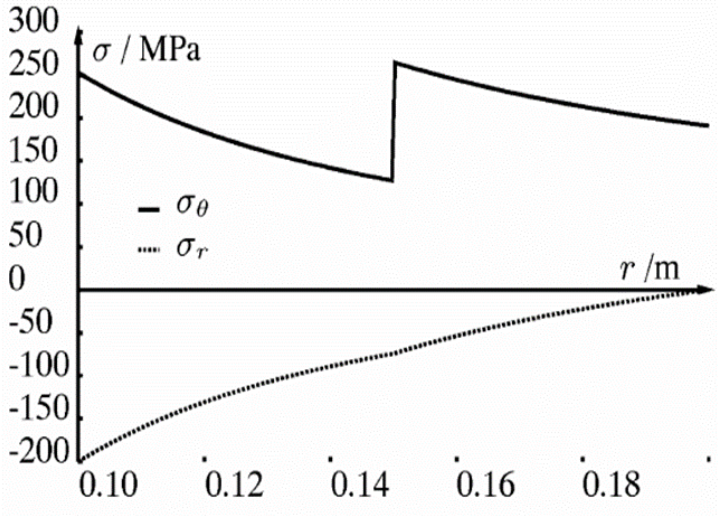

Figure 1-6. Residual stresses distribution through the compound cylinder wall due to shrink-fit interference and working pressure [26]

c) Autofrettage process

The autofrettage process is a specialized mechanical surface treatment technique that entails subjecting the inner or outer surface of a thick-walled cylinder to high pressure, resulting in permanent deformation. This technique introduces beneficial residual stresses near the bore region of the cylinder. Extensive research has been conducted to analyze the residual stress profile throughout the wall of thick-walled cylinders due to the autofrettage process [31– 49], encompassing different production methods based on the type of load applied: hydraulic, swage, explosive, thermal, and rotational.

In hydraulic autofrettage [50], high hydraulic oil pressure generates the desired residual stresses. Swage autofrettage employs an oversized mandrel to deform the cylinder's inner surface plastically [51]. Explosive autofrettage [52], on the other hand, utilizes detonations in a fluid medium within the cylinder to induce plastic deformation and pressure. Thermal autofrettage relies on temperature gradients to create the necessary residual stresses [53]. Lastly, rotational autofrettage involves spinning the cylinder at high speeds, causing centrifugal forces to deform the inner surface and introduce induced stresses [54]. In this study, the focus is on the analysis of hydraulic autofrettage.

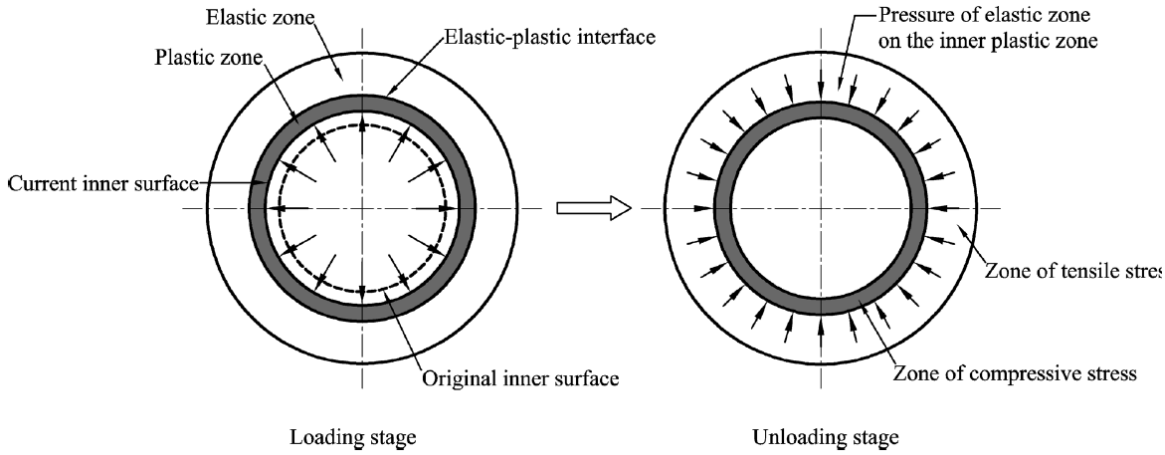

Figure 1-7. Manufacture stages of inner autofrettage process - demonstration of the working theory [55]

The autofrettage process can be classified into two distinct categories: inner autofrettage and outer autofrettage. Both processes consist of a two-stage procedure involving the loading stage and the subsequent unloading stage. In the inner autofrettage process, as shown in Figure 1-7, the thick-walled cylinder bore is subjected to excessive loading pressure, inducing permanent deformation within the inner bore region of the cylinder. Following the removal of the applied loads, the inner part of the cylinder experiences compression due to the elastic recovery of the outer part. Consequently, this results in the generation of advantageous compressive residual stress near the bore area, enhancing the structural integrity of the cylinder.

Conversely, the outer autofrettage method involves overloading the outer surface of the thick-walled cylinder. The primary objective of this approach is to mitigate the tensile stresses present at the outer surface of the cylinder. By subjecting the outer surface to excessive pressure, the

overall level of tensile stress within the cylinder is effectively reduced after the unloading process. This process is particularly beneficial in increasing the fatigue life of structures that are prone to outer surface fatigue, making it a valuable technique in various engineering applications [56].

Undoubtedly, the autofrettage process plays a crucial role in enhancing the durability and load-carrying capacities of thick-walled cylinders [57]. However, it is essential to consider one notable disadvantage associated with the reduction of the yield strength during the unloading stage due to the Bauschinger effect, which can influence the effectiveness of the autofrettage technique. The Bauschinger effect is a phenomenon in which a material experiences a reduction in its yield strength when subjected to compressive loading and subsequent unloading. In the context of autofrettage, this effect becomes relevant during the unloading stage [58– 60].

Numerous investigations have focused on analyzing residual stresses and deformation in thick-walled cylinders subjected to autofrettage, leading to significant advancements in the field. Hodge et al. [61] presented a model employing the Prandtl-Reuss flow type stress-strain law and Hencky's deformation law to study stresses and displacements in a hollow, partially plastic, infinitely long cylinder. Both cases considered the von Mises yield condition and material compressibility, yielding comparable results.

Jahed et al. [62] developed a consistent method for calculating residual stresses resulting from the autofrettage process using elastic solutions under axisymmetric loading conditions. Their proposed solution incorporated actual material unloading curves, considering isotropic and/or kinematic hardening rules and a variable Bauschinger effect. The calculated residual hoop stress demonstrated excellent agreement with experimental measurements near the bore, highlighting the importance of accounting for the variable Bauschinger effect factor in predicting reverse yield initiation.

In further research, Parker [63] introduced a notable rule of thumb, revealing that the Bauschinger effect reduces the maximum beneficial residual hoop stress at the inner wall of a typical hydraulically autofretted cylinder by around 30% compared to ideal material behaviour that neglects this effect. Parker also recommended extending the ASME Boiler and Pressure Vessel Code to include standardized procedures for designing thick-walled cylindrical pressure

vessels with autofrettage. The code takes a conservative approach, allowing for a maximum autofrettage of 40% and restricting anything above that percentage. To enhance the existing codes, Parker proposed employing three key parameters: tangential strain on the outer surface, residual tangential strain on the inner surface, and autofrettage pressure, to estimate the radius of the elastic-plastic interface. This research emphasizes the significance of updating design standards to account for the Bauschinger effect and considers overstrains exceeding 40%.

d) Combination of reinforcement processes

Each reinforcement process, namely wire-winding, shrink-fit, and autofrettage, is associated with specific limitations. The wire-winding and shrink-fit processes have been found to have limited compressive stresses near the bore area when compared to the autofrettage process. Moreover, the shrink-fit process exhibits a stress transition from compressive to tensile at the interface surface between the layers, leading to high tensile stress at the outer surface of the outer layer. Additionally, the autofrettage process is affected by the Bauschinger effect, which hampers the development of compressive stress. To address these limitations and improve the distribution of compressive residual stress across the wall thickness, researchers have introduced a new design philosophy for thick-walled cylinders that involves employing various combinations of reinforcement processes [64, 65]. By combining these processes, it becomes possible to mitigate the drawbacks associated with individual techniques and achieve a more uniform and effective distribution of compressive stress.

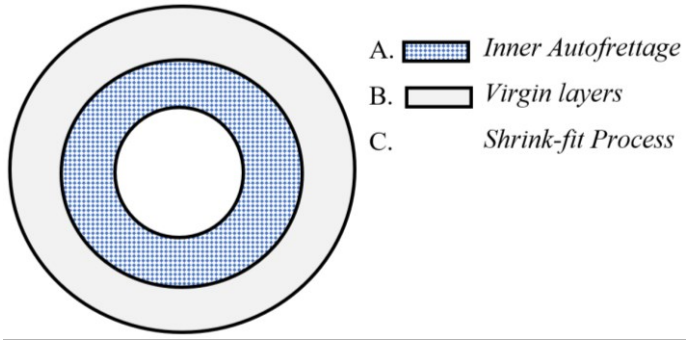

Figure 1-8. Schematic representation of the thick-walled cylinder production sequences proposed by Kapp et al. [66].

In light of the previous observed limitations of each individual reinforcement process, Kapp et al. [66] have proposed a multi-layer design for thick-walled cylinders subjected to cyclic

mechanical loading conditions, aiming to enhance their fatigue lifetimes. This design involves the compounding of an outer virgin tube with an auto-fretted inner tube through a shrink-fit process, as shown in the schematic Figure 1-8. Once the autofrettage process is performed on the inner tube, the subsequent operation of the shrink-fit process leads to a notable increase in the compressive residual stress, especially near the bore area of the inner tube. However, it is crucial to consider the presence of the Bauschinger effect, whereby the inner region is prone to re-yielding. This re-yielding phenomenon significantly diminishes the benefits gained from the reinforcement processes, thereby reducing their effectiveness.

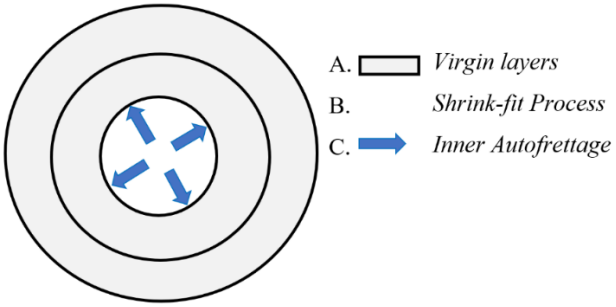

Figure 1-9. Schematic representation of the thick-walled cylinder production sequences proposed by Parker [67].

To address the challenge posed by the re-yielding effect and achieve a more desirable distribution of residual stress across the wall thickness, previous studies [68– 70] have put forth the idea of removing the thickness of re-yielded material from the inner region. An alternative and innovative solution to handle the re-yielding issue was proposed by Parker et al. [67]. They suggested the adoption of a shrink-fit approach involving two virgin tubes before subjecting the entire assembly to autofrettage. This procedure is visually depicted in Figure 1-9.

In the course of their investigation, various levels of shrink-fit clearance schemes were examined. The residual stress distribution through the wall thickness of their thick-walled configuration was then compared with those from the transitional shrink-fit of two virgin layers, ideal autofrettage, and monobloc autofrettage, as shown in Figure 1-10. In the figure, the main difference between ideal autofrettage and monobloc autofrettage lies in the treatment of the Bauschinger effect. In ideal autofrettage, the Bauschinger effect is ignored, while in mono-block autofrettage, it is considered. Based on the results from Figure 1-10.B, the suggested configuration of compounding two virgin tubes before subjecting the entire assembly to autofrettage shows

significant benefits in reducing near-bore plastic strain by around 50% when compared to monobloc autofrettage. This reduction is vital as it helps counter the negative impact of the Bauschinger effect and preserves the near-bore compressive residual hoop stress. As a result, the proposed thick-walled cylinder configuration leads to improved overall performance.

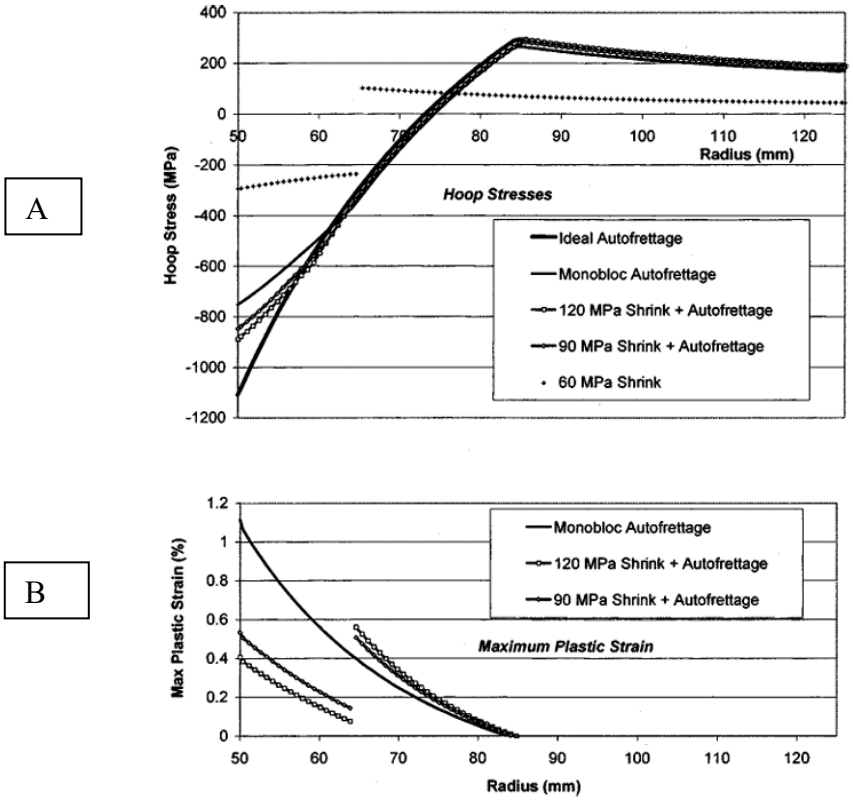

Figure 1-10. Residual hoop stress (A) and plastic strain (B) distribution through the wall [67].

In a similar study, Lee et al. [71] also employed the technique of shrink-fitting two virgin tubes before subjecting them to an inner autofrettage process. During their investigation, they investigated different levels of overstrain and considered two material behaviour approaches: strain hardening and elastic-perfect plasticity. The results based on experimental data revealed that the strain hardening approach provided more accurate results, particularly near the bore area of the thick-walled cylinder. They observed that increasing the overstrain level up to 80% led to a significant improvement in the residual compressive stress. They also found that when a large shrink-fit clearance was used, it caused higher compressive and tensile residual stresses in the inner and outer cylinders, respectively. As a result, the shrink-fit process proved to be highly efficient in increasing the compressive residual stress within their thick-walled cylinder configuration, but

there was a limit to its effectiveness. Beyond this limit, it had a negative impact on the distribution of residual stress, especially in the outer layer.

Yuan et al. [72] proposed a novel alternative configuration for thick-walled cylinders. In their approach, both inner and outer tubes are subjected to the autofrettage process before compounding the two tubes with each other using shrink-for process, as shown in the schematic Figure 1-11.

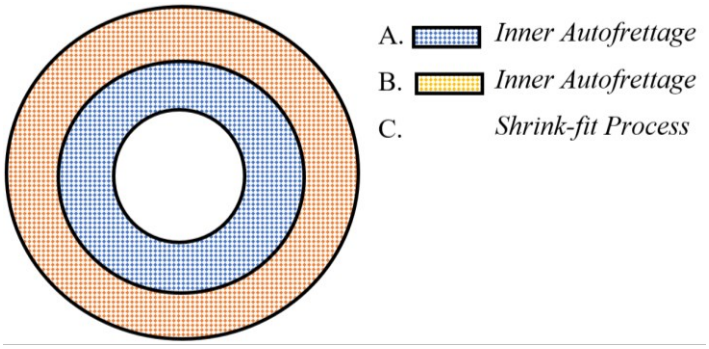

Figure 1-11. Schematic representation of the thick-walled cylinder production sequences proposed by Yuan [72].

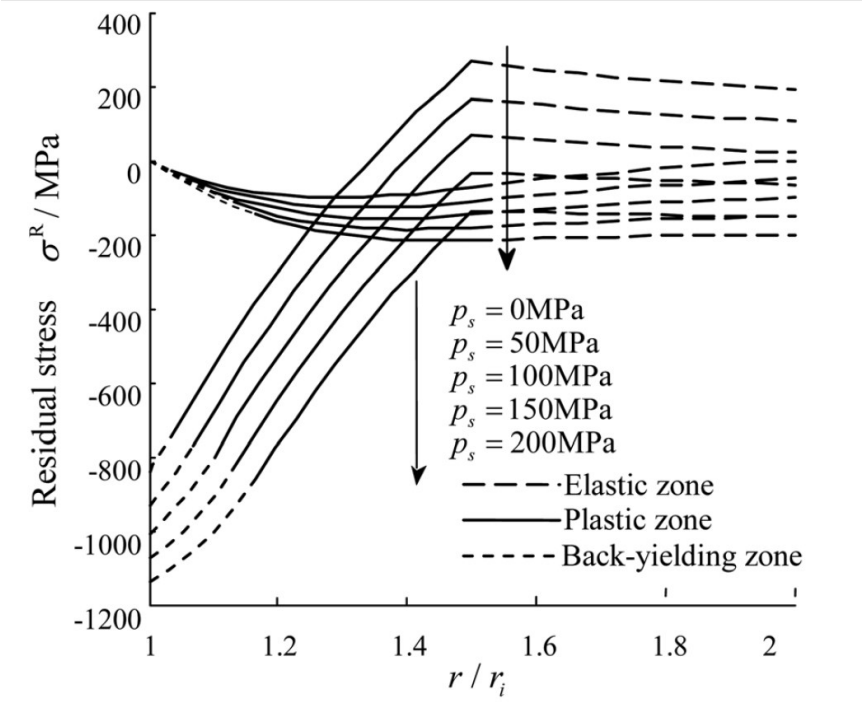

Figure 1-12. Residual stresses distribution through the wall [72].

Their findings indicated that an increase in the compounding pressure elevated the compressive residual stress within the inner cylinder wall, but it concurrently increased the

unfavourable tensile stress in the outer cylinder, as shown in Figure 1-12. Notably, such tensile stress increasing on the outer surface may potentially shorten the service life of the cylinders, particularly if they are prone to outer surface fatigue.

To address this concern, Parker [56] developed a reversed autofrettage process, commonly referred to as the outer autofrettage process [73]. In this approach, the outer surface of the thick-walled cylinder is overloaded to alleviate the tensile residual stress on its outer surface. Parker's novel configuration involves shrinking a traditional autofrettage inner layer alongside a reverse autofrettage outer layer, as shown in the schematic Figure 1-13.

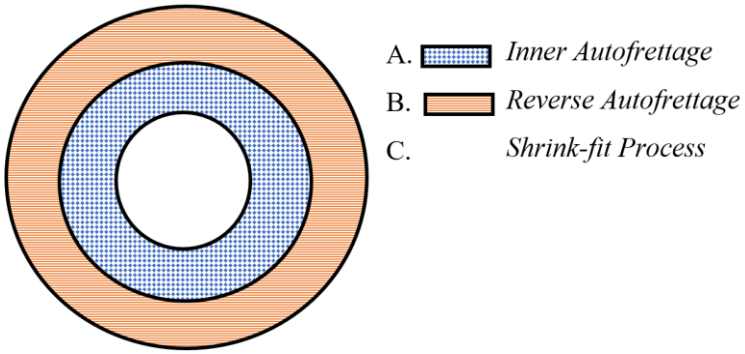

Figure 1-13. Schematic representation of the thick-walled cylinder production sequences proposed by Parker [56].

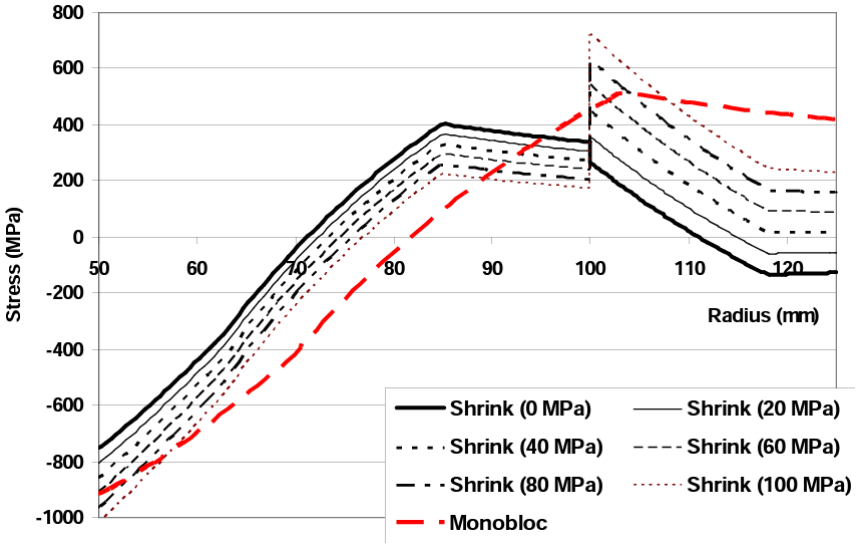

Figure 1-14. Residual stress distribution through the wall for different configurations [56]

Figure 1-14 illustrates the residual hoop stress distribution across the wall of a monobloc cylinder subjected to inner autofrettage pressure, resulting in a 70% overstrain (indicated by the red line). Additionally, it presents the corresponding residual hoop stress profile for the proposed configuration, where both the inner and outer tubes undergo individual inner and outer autofrettage processes, respectively, each causing a 70% overstrain. The investigation covers a range of interface pressure levels, spanning from zero to 100 MPa. According to Figure 1-14, the proposed thick-walled cylinder configuration by Parker [56] offers the same advantages as Yuan's configuration [72] for the inner tube while simultaneously reducing the detrimental residual hoop stress at the outer surface, which enhances the overall performance of the thick-walled cylinder. By achieving a favourable reduction in the tensile stress on the outer surface, this configuration extends the fatigue life of the cylinders, particularly in outer surface fatigue scenarios.

1.3.2 Design optimization of thick-walled compound cylinders

The optimization of thick-walled compound cylinders is crucial due to the diverse configurations involved in their production sequence, necessitating careful consideration. Achieving an ideal design for such cylinders entails taking into account various critical parameters, including the manufacturing sequence, inner and outer autofrettage pressures, shrinking interference, and layer thickness. The primary objective is to attain an optimal residual stress profile throughout the cylinder wall, thus significantly enhancing the overall structural performance.

Very limited studies have been conducted on design optimization of compound cylinders. There are a number of studies particularly concerning the optimization of thick-walled compound cylinders subjected to both autofrettage and shrink-fit processes [74– 77]. In these studies, various configurations of multi-layer thick-walled cylinders treated with different combinations of shrink-fit and autofrettage processes during their production have been investigated. The primary aim of these investigations has been to identify the optimum configurations and manufacturing parameters that lead to an optimal distribution of residual stresses, ultimately contributing to the enhancement of the fatigue life of cylinders. Notably, the key distinction among these studies lies in the optimization techniques employed. Jahed [75], in his work, utilized the simplex optimization search technique, a robust and efficient method to explore the design space and determine the optimal values of design parameters for each proposed thick-walled cylinder configuration. By

focusing on maximizing the compressive residual stress within each combination, Jahed aimed to enhance the thick-walled cylinder's durability under various loading conditions. Similarly, Kumar et al. [76] investigated the optimization process using the genetic algorithm technique, a powerful optimization approach inspired by the process of natural selection. Their study aimed to achieve the same objective as Jahed's research, namely, maximizing the compressive residual stress for each proposed thick-walled cylinder configuration. The genetic algorithm offered a more robust and flexible approach to searching for global optimal solutions in the design space, considering the trade-offs between multiple design objectives.

Expanding upon the work of Kumar et al., Ossama et al. [77] explored a more comprehensive optimization strategy by integrating both the genetic algorithm and sequential quadratic programming (SQP) techniques. By combining these optimization methods, they aimed to accurately determine the global optimal values of design variables for each thick-walled cylinder configuration. The primary objective of their study was twofold: maximizing the compressive residual stress to improve structural performance and simultaneously minimizing the tensile stress at the outer surface to mitigate potential failure modes.

The collective efforts of these research studies underscore the active endeavours within the scientific community to address the design optimization challenges associated with thick-walled cylinders subjected to complex manufacturing processes. As research in this field continues to progress, it is expected that new insights and advancements will emerge, leading to further improvements in the design and performance of thick-walled cylinders for diverse engineering applications.

1.3.3 Fatigue life evaluation

In thick-walled cylinder structures operating under cyclic loading conditions, there is a significant concern regarding their response to fatigue cycling. To ensure the integrity and safety of these structures, it is essential to conduct a fundamental assessment of their fatigue life in response to such loading conditions. To address this concern, several studies have conducted extensive investigations into the fatigue evaluation of thick-walled cylinders under cyclic loading [78– 86]. These studies have played a vital role in revealing the underlying mechanisms that govern

crack propagation, offering valuable insights into how these structures behave under different operational conditions.

The majority of studies mainly rely on the ASME fatigue life code, which offers guidelines and standards for assessing the fatigue performance of engineering components and structures subjected to cyclic loading. The evaluation of stresses in regions where cracks are likely to initiate and propagate due to cyclic loading significantly influences the fatigue life of such structures. Consequently, for thick-walled cylinders, identifying regions with the highest risk of crack initiation is crucial, as they experience alternating stresses during cyclic loading. Fatigue cracks can initiate from stress concentrations in these locations and propagate under repeated loading cycles, potentially leading to cylinder failure.

To determine fatigue lifetimes using the ASME code, the flow of work in published studies follows the following sequence: Firstly, the stress intensity factors are calculated, adhering to the guidelines in D-401.1 of Appendix D [11]. This involves fitting the stress profile through the wall thickness resulting from the applied loads as a function of the ratio of the radial distance from the inner surface to the wall thickness. Using the curve fitting coefficients, the stress intensity factor K_I is then computed. Subsequently, the Paris relation is applied to estimate the number of cycles required for crack growth leading to failure. This estimation is achieved through numerical integration of the crack growth rate in relation to the stress intensity factor. This comprehensive procedure ensures a precise evaluation of the fatigue lifetimes of thick-walled cylinder structures under cyclic loading conditions. The references [75, 87], and [88] provide a detailed analysis of fatigue assessments using the ASME code, further validating the credibility of this research approach.

As fatigue assessment in thick-walled cylinders depends on stress distribution across the wall thickness, beneficial compressive residual stress profiles within the wall are crucial for enhancing their fatigue life. In light of this, Parker et al. [87] conducted a study comparing two residual stress profiles in two configurations using the ASME code. One configuration combined two virgin layers before autofrettage, while the other simply shrink-fitted two virgin layers. The research revealed that the thick-walled cylinder with the compounding layers prior to autofrettage had a remarkable 41% increase in mechanical lifetime compared to the conventional shrink-fit method.

Moreover, other studies [75, 89] also utilized the ASME code to determine the most optimal cylinder configuration among different proposed configurations, further emphasizing the importance of fatigue assessment in design optimization for improved structural integrity and durability in specific applications.

In summary, the ASME fatigue life code is a widely used standardized tool for assessing the lifetime of thick-walled cylinder structures and predicting crack propagation. Stress evaluation in regions prone to crack initiation and propagation, particularly the cylinder bore, plays a pivotal role in understanding and predicting the fatigue life of such structures. Accurate assessments of these stress-critical areas are vital for ensuring the structural longevity and operational reliability of these components in engineering applications.

1.3.4 Thermo-mechanical response of thick-walled cylinders

Numerous methodologies have been explored to predict the response of thick-walled cylinders under combined thermal and mechanical loads. Thermo-elasticity has been effectively utilized to model the thermo-mechanical response of thick-walled cylinders. Previous studies have categorized the thermo-elasticity models into two distinct types of mathematical models: uncoupled and coupled thermo-elasticity models. The primary difference between the two groups is the presence or absence of coupling between the displacement and temperature fields in the governing equations of thermo-elasticity. In the coupled thermo-elasticity model, the displacement field is incorporated in the energy equation. In contrast, the uncoupled model neglects the influence of the displacement field on the energy equation.

a) Uncoupled approach

In uncoupled thermo-elasticity, the displacement response is ignored in the energy equation. This decoupling enables the energy equation to be solved independently of the elasticity equations. As a result, the temperature distribution across the structure wall can be determined by considering only the thermal boundary conditions. The temperature field obtained in this manner can be subsequently set as an input beside the mechanical boundary conditions in the elasticity model to estimate the thermo-mechanical response of the structure.

According to published studies, uncoupled thermo-elastic models can be classified into static and dynamic models, depending on whether inertia effects are considered in the elasticity equations. Static models exclude inertia effects, while dynamic models explicitly incorporate inertia effects. In structures under rapid time-dependent loadings, considering inertia effects is necessary to accurately capture the accurate dynamic behaviour of the structure.

Sentürk et al. [90] conducted an analytical investigation into the thermo-mechanical response of a machine gun barrel using a static uncoupled model. Their study aimed to understand the behaviour of the barrel under thermal loading. To achieve this, they solved the steady-state heat conduction equation, which allowed them to obtain the temperature distribution across the barrel's thickness. Based on these temperature results and elasticity theory, they calculated the stresses, disregarding the inertia effect in governing the equation of motion.

In a separate study, Farhan et al. [91] focused on the influence of inertia effects in the thermo-mechanical analysis by adopting a dynamic uncoupled model approach. They considered the dynamic response of the structure to time-dependent loads. To investigate the stresses and temperature distribution across the thickness of a cylinder, they utilized the Finite-Difference (FD) method as a numerical approach. This choice was motivated by the incorporation of temperature-dependent material properties (TDMP), which added complexity to the analytical solution.

In brief, uncoupled thermo-elasticity models provide a valuable framework for studying the thermal and mechanical responses of structures. By solving the energy equation separately from the elasticity equations, the temperature field can be determined and subsequently utilized in the elasticity model to estimate the thermo-mechanical response. Researchers have explored both static and dynamic models, employing analytical and numerical techniques to investigate different aspects of thermo-elasticity. The choice of solving technique depends on specific requirements, including the consideration of inertia effects and temperature-dependent material properties.

b) Coupled approach

Although decoupled models provide accurate predictions for the response of thermo-mechanically loaded structures, they fall short in accurately predicting the actual physical behaviours of structures subjected to sudden thermo-mechanical loading conditions. These

conditions occur when the loading period is much smaller compared with the lowest natural period of the structure [92]. To address this issue, it is essential to employ coupled models that link elasticity and energy equations through both displacement and temperature fields. Coupled models enable the estimation of the thermo-mechanical response by simultaneously solving the elasticity and energy equations. The main governing equations for the coupled thermo-elasticity was presented by Duhamel [93].

Several prior investigations have utilized coupled thermo-elasticity models to assess the thermo-elastic responses of thick-walled cylinders under sudden boundary conditions. These studies can be classified into two categories: those employing analytical solutions and those utilizing numerical approaches. Analytical solutions, as exemplified by publications [94– 97], are based on fundamental mathematical principles. For instance, Eslami et al. [94] presented a closed-form solution for the classical coupled thermo-elasticity problem in cylindrical coordinates. Their solution relies on the Eigen function of the Fourier expansion. Similarly, Kouchakzadeh et al. [96] investigated a closed-form solution for a rotating disc, incorporating body forces into the elasticity model based on coupled thermo-elasticity.

Numerical solutions using finite difference (FD), or finite element (FE) methods have also been employed to handle coupled thermo-elasticity problems [98– 100]. These numerical approaches offer enhanced capabilities as they can accommodate complex loading conditions and nonlinear material properties, which pose challenges for analytical solutions. Abd-Alla et al. [100] proposed an FD solution for a coupled thermo-elasticity problem in a thick-walled cylinder subjected to nonlinear boundary conditions. Their FD model is based on the unconditionally stable Crank-Nicolson approach. It should be noted that all the aforementioned studies assume temperature-independent material properties (TIMP) [94, 100]. However, a limited number of studies have explored temperature-dependent material properties (TDMP) to investigate the solution of coupled thermo-elasticity under simple loading conditions [101, 102].

1.4 Identification of Gaps in The Literature and Objective

The existing literature highlights several research gaps that require further investigation. Firstly, there is a lack of studies specifically focusing on the transient response of temperature-dependent thick-walled cylinders under cyclic nonlinear thermomechanical shocks. To address

this, considering coupled thermo-elasticity and temperature-dependent material models becomes crucial to accurately estimating the thermo-mechanical response of thick-walled cylinders under such harsh conditions. Secondly, although there are numerous numerical solutions available to estimate the residual stress profile through the thickness of thick-walled cylinders resulting from different reinforcement processes, such as shrink-fit and autofrettage, there is a notable absence of analytical solutions to predict the residual stress profile induced by the various combinations of the available reinforcement processes. Lastly, limited research has been conducted on identifying the optimal design of thick-walled compound cylinders under combined reinforcement processes, with the objective of enhancing their overall performance.

In light of the above-mentioned research gabs, the primary objective of this study is to comprehensively examine the response of thick-walled cylinders subjected to thermo-mechanical loading conditions while considering the impact of temperature-dependent material properties. Additionally, the research aims to develop effective design optimization methodologies utilizing artificial intelligence techniques. To accomplish the objectives, the present research study proceeds through the following stage:

- The first stage of this study focuses on the transient response of temperature-dependent thick-walled cylinders under cyclic nonlinear thermo-mechanical loads using coupled thermo-elasticity. The coupled thermo-elasticity model is numerically solved using the finite-difference method, and the findings are further validated through experimental measurements. Also, the accuracy of the results based on temperature-dependent material properties (TDMP) and temperature-independent material properties (TIMP) assumptions is compared.
- In the second stage of this study, analytical formulations have been developed for predicting the distribution of residual stress through the thickness of thick-walled cylinders subjected to different combinations of reinforcement processes. This stage involves performing procedures on different configurations of thick-walled cylinders, considering the same manufacturing sequences.
- In the third stage of this study, a design optimization approach is employed to determine the optimal configuration of a thick-walled cylinder, incorporating different combinations of reinforcement processes. The objective is to identify optimal design parameters, including

layer thickness, shrink-fit interference, inner autofrettage pressure, and outer autofrettage pressure (if applicable), in order to maximize compressive residual stress near the bore area, thereby extending the cylinder's lifetime. To achieve this, the objective function is derived using a machine learning approach.

- In the fourth stage of this study, the thermo-mechanical fatigue life of the optimal thick-walled cylinder configuration is evaluated under cyclic nonlinear thermo-mechanical loading conditions, taking into consideration the temperature-dependent material properties.

1.5 Thesis Organization

This dissertation follows a manuscript format, where each chapter is a self-contained document. While there might be some similarities in the information presented across chapters, efforts have been made to present it in a simple way. Chapters 2 to 4 contain revised versions of papers that were published or submitted and are currently under review. These chapters have been reformatted to ensure consistency in font size, style, reference numbering, and figure and equation numbering, resulting in a cohesive and comprehensive presentation. The dissertation consists of five chapters and three appendices. After this introductory chapter, the subsequent chapters are organized as follows:

Chapters 2 to 4 include the reformatted papers, providing their respective contexts as follows: Chapter 2 focuses on modelling the transient response of temperature-dependent thick-walled cylinders under cyclic nonlinear thermo-mechanical loads using the classical coupled thermo-elasticity approach. Chapter 3 presents analytical formulations to predict the residual stress distribution due to various reinforcement processes through the compound thick-walled cylinder wall. Chapter 4 addresses a design optimization formulation, determining the optimal configuration of a thick-walled cylinder due to various reinforcement processes to enhance thermomechanical fatigue under cyclic nonlinear dynamic loading conditions.

Chapter 5 concludes the dissertation by summarizing the main findings and offering recommendations for future research.

CHAPTER 2

TRANSIENT COUPLED THERMO-ELASTICITY ANALYSIS OF A TEMPERATURE-DEPENDENT THICK-WALLED CYLINDER UNDER CYCLIC THERMO-MECHANICAL LOADS

Authors: Mohamed Elfar, Ramin Sedaghati, and Ossama R. Abdelsalam [103].
Status before thesis submission: Published in: Journal of SN Applied Sciences, Volume: 5. Initially submitted on: 21st July 2022. / Accepted: 15th November 2022. Published on: 8th December 2022.

Abstract

Several studies have reported the solution of the classical coupled thermo-elasticity for thick-walled cylinders under different boundary conditions; however, no study has been conducted on the analysis of temperature-dependent thick-walled cylinders under cyclic nonlinear boundary conditions. Therefore, this study investigates the transient response of temperature-dependent thick-walled cylinders under cyclic nonlinear thermo-mechanical loads based on classical coupled thermo-elasticity. Also, it studies the impact of considering temperature-dependent material properties (TDMP) and temperature-independent material properties (TIMP) hypotheses on the accuracy of the results. The governing equations of the classical nonlinear coupled thermo-elasticity are numerically solved based on the finite-difference method, namely the Crank-Nicolson method. Then, an experimental setup is designed to further investigate the impact of considering TDMP and TIMP through a temperature measurement of the outer surface of a machine gun barrel under burst shooting. It has been found that considering TIMP overestimates the residual temperature and residual stress values through the cylinder thickness compared with TDMP. Moreover, based on the temperature measurement, TDMP estimates results with higher accuracy of 7% than TIMP.

2.1 Introduction

Thick-walled cylinders are widespread components utilized in several industrial fields such as mechanical, aerospace, naval and offshore, petrochemical plants, military, and electronics. They can work as pressure vessels in different structures under different mechanical or thermo-mechanical loading conditions.

Some of these structures work under timely-repeated thermo-mechanical loading conditions, as in machine gun barrels that are subjected to continuous shooting. Modelling of the effect of these cyclic thermo-mechanical loading conditions is difficult and maybe a challenging affair. This is because the time between two successive input loads is generally too short to allow the cooling down of the cylinder. Therefore, this leads to thermal accumulation in the cylinder material, which causes variations in stress and temperature distributions through the cylinder thickness [98, 99]. In addition, heat accumulation in cylinders may cause remarkable variations in their mechanical and thermal properties. Therefore, the design process of these timely-repeated thermo-mechanical loaded structures is a thriving field of study because it involves coupled multi-physics design problem that incorporates a nonlinear material response due to mechanical and thermal loading.

Several published works investigate thick-walled cylinder response due to thermo-mechanical boundary conditions based on thermo-elasticity [104– 107]. Thermo-elasticity is a mathematical model that predicts the structure response due to thermo-mechanical loading conditions. The main governing equations of thermo-elasticity are nearly the same as those for elasticity equations besides the energy equation [92]. According to the studies reported, the solution of thermo-elasticity can be arranged under two groups of mathematical models, namely: uncoupled and coupled thermo-elasticity models [108, 109]. The main difference between the two groups is the coupling between the displacement and temperature fields in the governing equations of thermo-elasticity. Unlike the coupled thermo-elasticity, the displacement field on the energy equation is ignored in uncoupled model.

Uncoupled thermo-elastic models can be classified as static and dynamic models. The difference between the two groups is the consideration of inertia effects, in the elasticity equations, that are accounted for only in dynamic models. However, including the inertia effect is thought to be necessary, especially in rapidly time-dependent-loaded structures. It is worth noting that, as the

displacement response is ignored in the energy equation, the energy equation can be solved firstly and separately from the elasticity equations. Then, the temperature field can be fed to the model of elasticity in order to estimate the thermo-mechanical response of the structure, as shown in Figure 2-1(a). Several reported studies discuss the solution of thermo-elasticity based on uncoupled models [90, 91] and [110– 114]. Sentürk et al. [90] used the static uncoupled model to analytically investigate the thermo-mechanical response of a machine gun barrel. They solved the steady state heat conduction equation to get the temperature distribution through the barrel thickness. Then they calculated the stresses based on the temperature results and elasticity theory ignoring the inertia effect on the equation of motion. On the other hand, Farhan et al. [115] considered the inertia effect on the elasticity model, and then they numerically investigated the stresses and temperature distribution through a cylinder thickness based on the dynamic uncoupled model approach. They considered the numerical approach based on the Finite-Difference (FD) rather than the analytical model. As they considered in their study temperature-dependent material properties (TDMP); then, the analytical solution in that case become more complicated.

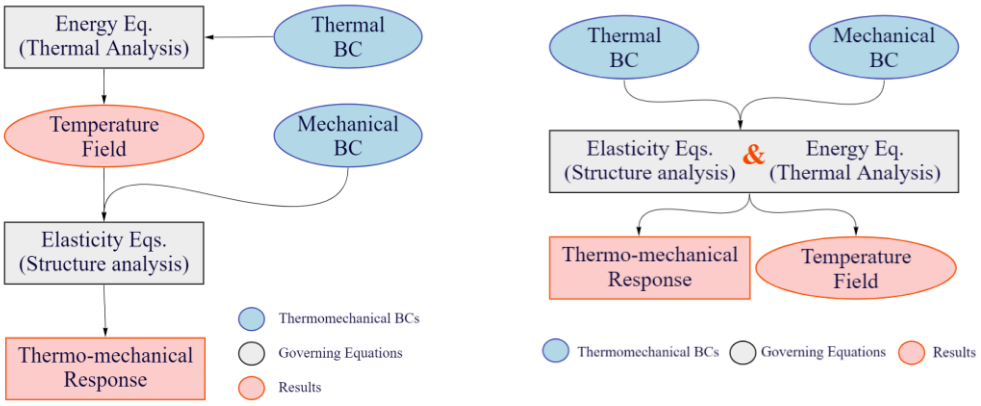

(a) Uncoupled hypothesis (b) Coupled hypothesis

Figure 2-1. Flow work solution of thermo-elasticity problem

Although uncoupled models give an accurate response prediction for several thermo-mechanical loaded structures, they failed to predict actual physical behaviors of structures worked under sudden thermo-mechanical loading conditions (in which the loading period has the same order as the structure's lowest natural frequency magnitude [92]). In this case, the use of coupled models in which elasticity and energy equations are coupled through both displacement and temperature fields is thought to be a must. The thermo-mechanical response in coupled models is

estimated through the simultaneous solution of the elasticity and energy equations, as shown in Figure 2-1(b).

Coupled thermo-elasticity models were used in some previous studies to evaluate the thermo-elastic responses of thick-walled cylinders under different boundary conditions. These studies can be categorized based on the solutions to analytical and numerical solutions. On the one hand, the analytical solutions are based on fundamental mathematics, as in [94– 97]. Eslami et al. [94] presented a closed-form solution for the classical coupled thermo-elasticity problem in cylindrical coordinates; the solution is based on the Eigen function of Fourier expansion. Using the same concept, Kouchakzadeh et al. [95] investigated a closed form solution of a rotating disk (the body force is included in the elasticity model) based on the coupled thermo-elasticity.

On the other hand, numerical solutions based on FD or Finite-Element FE are also used for coupled thermo-elasticity problems [98– 100]. They provide more powerful tools as they can account for more complicated loading conditions and nonlinear material properties, which is challenging in analytical solutions. Abd-Alla et al. [100] presented an FD solution for a coupled thermo-elasticity problem in cylindrical coordinates considering nonlinear boundary conditions. The FD model is based on the unconditionally stable Crank-Nicolson approach. All aforementioned studies [94, 100] are built under the assumption of temperature-independent material properties (TIMP). However, few studies consider temperature-dependent material properties (TDMP) to investigate the solution of coupled thermo-elasticity for simple loading conditions [101, 102].

The difficulties of coupled models in comparison with uncoupled models can be summarized as (i) the need to include cyclic nonlinear thermo-mechanical working conditions as it occurs in real systems. These need deep investigation to clearly depict the effect of thermal accumulation on stress and temperature responses due to highly cyclic loading conditions, and (ii) considering TDMP in elasticity and energy equations needs more investigation to depict its effect on calculations accuracy. Also, it is interesting to mention that considering TDMP hypothesis converts the problem to a nonlinear thermo-elasticity problem. These types of problems are mentioned as challenges in previous studies [115]. Overcoming these challenges on coupled

thermo-elasticity approach leads to accurately simulating thick-walled cylinder response under different working boundary conditions.

This paper presents a coupled approach to investigate the transient thermo-mechanical response of temperature-dependent thick-walled cylinders under highly cyclic nonlinear thermo-mechanical shocks. A detailed numerical solution procedure is implemented to solve the nonlinear coupled thermo-elasticity governing equations. The developed numerical model is based on the Crank-Nicolson approach. Then, the model results are validated with the results from the literature. Moreover, a comparative study is performed to investigate the impact of considering TDMP and TIMP hypotheses on the accuracy of the results. Furthermore, an experimental setup is designed to further investigate the impact of considering TDMP.

The paper is structured as follows, the main governing dynamic equations that address the classical nonlinear coupled thermo-elasticity in cylindrical coordinates are formulated in Section 2.2. Then, Sect. 2.3 presents the detailed finite-difference numerical solution of the nonlinear coupled thermo-elasticity for general thermal and mechanical boundary conditions. Sect. 2.4 presents the model validation with previous work in the literature, followed by the experimental setup and the comparative study of considering TIMP and TDMP on the accuracy of the results. Finally, conclusions are drawn in Section 2.5.

2.2 Governing Equations

Consider a thick-walled cylinder made of isotropic material with an inner radius R_i and outer radius R_o (as shown in Figure 2-2) subjected to axisymmetric thermo-mechanical loading conditions. The cylindrical coordinates (r, θ, z) and axisymmetric plane strain conditions have been assumed; thus, $u_\theta = u_z = 0$ and $u_r = u(r,t)$. Therefore, the strain–displacement relations in cylindrical coordinates can be described as the following:

$$\varepsilon_r = \frac{\partial u_r}{\partial r}\,, \qquad \varepsilon_\theta = \frac{u_r}{r}\,, \qquad \varepsilon_z = \gamma_{r\theta} = \gamma_{rz} = \gamma_{\theta z} = 0 \tag{2-1}$$

The classical coupled approach of the thermo-elasticity theory is used to investigate the thermo-mechanical response of the thick-walled cylinder due to its loading conditions. The main governing equations of this approach are the elasticity equations and the thermal energy transfer. On the one hand, the main governing equations for the elasticity theory are [116]:

- The constitutive relations for isotropic material:

$$\sigma_r = \frac{E}{(1+\nu)(1-2\upsilon)}[(1-\nu)\varepsilon_r + \nu\varepsilon_\theta] - \frac{E\alpha}{(1-2\nu)}T$$
$$\sigma_\theta = \frac{E}{(1+\nu)(1-2\nu)}[\nu\varepsilon_r + (1-\nu)\varepsilon_\theta] - \frac{E\alpha}{(1-2\nu)}T \quad (2\text{-}2)$$

- The equation of motion "due to the absence of shear stresses and ignoring the body forces":

$$\frac{\partial\sigma_r}{\partial r} + \frac{\sigma_r - \sigma_\theta}{r} = \rho\ddot{u}_r \quad (2\text{-}3)$$

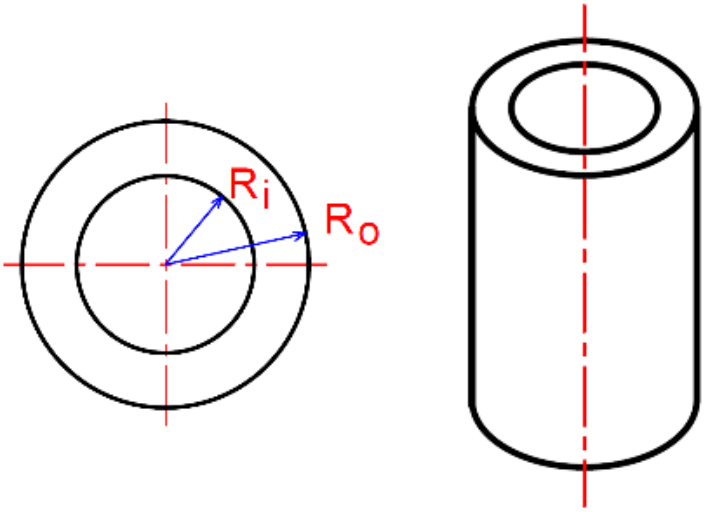

Figure 2-2. Schematic drawing of a thick-walled cylinder.

Substituting Eqs. (2-1) and (2-2) into Eq. (2-3) to put the equation of motion in terms of radial displacement components as:

$$\frac{\partial^2 u_r}{\partial r^2} + \frac{1}{r}\frac{\partial u_r}{\partial r} - \frac{u_r}{r^2} - \frac{\alpha(1+\nu)}{(1-\nu)}\frac{\partial T}{\partial r} - \frac{\rho\,(1+\nu)(1-2\nu)}{E\,(1-\nu)}\ddot{u}_r = 0 \quad (2\text{-}4)$$

where $\varepsilon_r, \varepsilon_\theta, \varepsilon_z, \gamma_{ij}(i,j=\{r,\theta,z\}; i\neq j)$, σ_r, σ_θ, E, υ, $\alpha, T, \ddot{u}_r, r,$ and ρ are the radial strain, hoop strain, axial strain, shear strain, radial stress, hoop stress, Young modulus of elasticity, Poisson's ratio, thermal expansion, temperature, radial acceleration, radial position, and density, respectively.

The root of the inverse coefficient of radial acceleration in Eq. (2-4) is known as the stress wave velocity,

$$v = \sqrt{\frac{\mathrm{E}\,(1-\nu)}{\rho\,(1+\nu)(1-2\nu)}} \tag{2-5}$$

On the other hand, the main governing equations of the thermal energy transfer are:

a) Fourier heat conduction equation

Assuming 1-D heat flow (only in the radial direction), the heat conduction through the thickness of the thick-walled cylinder is governed by the 1-D heat conduction equation as [117, 118]:

$$q_r = -kA\frac{\partial T}{\partial r} \tag{2-6}$$

b) Second law of thermodynamics

Considering the energy balance in the absence of the heat source, then it can also be described in one-dimensional as the following [119, 120]:

$$\frac{1}{A}\frac{\partial q_r}{\partial r} = -T_o\frac{dS}{dt} \tag{2-7}$$

c) Entropy

The entropy formula for isotropic material as a function of strains and material properties can be described as [92]:

$$S = \left(\frac{\rho C}{T_o}\right)T + \frac{E\alpha}{(1-2\nu)}\frac{\partial}{\partial t}(\varepsilon_r + \varepsilon_\theta) \tag{2-8}$$

where $q_r, T_o, k, S, C, t, and\ \alpha^*$ are, respectively, the heat flux vector in the radial direction, reference temperature, thermal conductivity, entropy, specific heat, time, and thermal diffusivity.

Eliminating S, q_r, ε_θ, and ε_r using Eqs. (2-1) and (2-6)-(2-8), the heat conduction equation considering TDMP can be expressed as:

$$\frac{\partial^2 T}{\partial r^2} + \frac{1}{r}\frac{\partial T}{\partial r} + \frac{1}{k}\frac{dk}{dr}\frac{\partial T}{\partial r} - \frac{1}{\alpha^*}\frac{\partial T}{\partial t} - \frac{T_o E\alpha}{k(1-2\nu)}\left(\frac{\partial^2 u_r}{\partial t\partial r} + \frac{1}{r}\frac{\partial u_r}{\partial t}\right) = 0 \tag{2-9}$$

It is worth noting that Eq. (2-9) is a nonlinear second-order partial differential equation. Also, this term (the third term) disappears for the case of TIMP; in this case, the equation is classified as a linear second-order partial differential equation.

Equations (2-4) and (2-9) together represent the governing equations of the classical coupled thermo-elasticity problem in cylindrical coordinates considering TDMP. Neglecting the strain rate term (last term) in the heat conduction Eq. (2-9) expresses the governing equations of the dynamic uncoupled thermo-elasticity. In that case, the heat conduction equation is solved independently of displacement Eq. (2-4).

Boundary conditions (loading conditions) besides initial conditions must be specified to solve Eqs. (2-4) and (2-9) simultaneously. On the interior surface of the thick-walled cylinder, the applied thermo-mechanical boundary conditions may be described as [94]:

$$\begin{aligned} \mathrm{w}_{11} u_r(\mathrm{R_i}, t) + \mathrm{w}_{12} \frac{du_r(\mathrm{R_i}, t)}{dr} + \mathrm{w}_{13} T(\mathrm{R_i}, t) &= \mathrm{f}_1(t) \\ \mathrm{w}_{21} T(\mathrm{R_i}, t) + \mathrm{w}_{22} \frac{dT(\mathrm{R_i}, t)}{dr} &= \mathrm{f}_2(t) \end{aligned} \tag{2-10}$$

while, at the exterior surface, the boundary conditions may be represented as [94],

$$\begin{aligned} \mathrm{w}_{31} u_r(\mathrm{R}_o, t) + \mathrm{w}_{32} \frac{du_r(\mathrm{R}_o, t)}{dr} + \mathrm{w}_{33} T(\mathrm{R}_o, t) &= \mathrm{f}_3(t) \\ \mathrm{w}_{41} T(\mathrm{R}_o, t) + \mathrm{w}_{42} \frac{dT(\mathrm{R}_o, t)}{dr} &= \mathrm{f}_4(t) \end{aligned} \tag{2-11}$$

The initial conditions of the thick-walled cylinder before applying the thermo-mechanical loads may also be defined as :

$$\begin{aligned} T(r, 0) &= \mathrm{f}_5(r) \\ u_r(r, 0) &= \mathrm{f}_6(r) \end{aligned} \tag{2-12}$$

where w_{ij} are the thermal and mechanical loading coefficients describing different boundary conditions such as temperature, flow convection coefficient, heat flux, flow pressure, and displacement.

2.3 Solution Methodology

This study investigates the solution of the classical coupled thermo-elasticity problem considering nonlinear loading conditions and material nonlinearities. As the analytical solution of the nonlinear thermo-elasticity problem is a challenging affair, the numerical solution is used to

solve Eqs. (2-4) and (2-9) that are described in section 2.2. The numerical solution is based on the FD approach, which converts the continuous equations to a system of linear algebraic equations by discretizing the time and spatial domains. The FD approach is used for its computational power efficiently, and the model is constructed on the two levels of three points Crank-Nicolson scheme. This scheme is unconditionally stable and has a second-order accuracy for both time and spatial domains [100].

2.3.1 Differential time and space scheme

The solution domain $\overline{D}$ of the Eqs. (2-4) and (2-9) is discretized with uniform mesh in spatial and time, described as $\overline{D}_{i,j} = \{(r_j, t_n)\,;\, j = 1,2,\ldots,J\,;\, n = 1,2,\ldots,N : r \in [R_i, R_o]\,, t \in [o, t_{end}]\}$. Assume $\Delta r = (R_o - R_i)/(J-1)$ as the mesh size in the spatial domain; thus, $r_j = R_i + j\Delta r$, while $\Delta t = t_{end}/(N-1)$ is the mesh size in the time domain, and thus $t_n = n\Delta t$.

2.3.2 The Crank-Nicolson finite difference method

Applying Crank-Nicolson finite difference discretization to nonlinear coupled thermo-elasticity Eqs. (2-4) and (2-9) with the boundary conditions described in Eqs. (2-10) and (2-11) yields:

- Equation of motion, Eq. (2-4):

$$\begin{aligned} &A_j T_{j-1}^{n+1} + B_j T_{j+1}^{n+1} + C_j u_{j-1}^{n+1} + D_j u_j^{n+1} + E_j u_{j+1}^{n+1} \\ &\qquad = -A_j T_{j-1}^{n} - B_j T_{j+1}^{n} - C_j u_{j-1}^{n} + Q_j u_j^{n} - E_j u_{j+1}^{n} + F_j u_j^{n-1} \end{aligned} \tag{2-13}$$

- Heat heat conduction equation, Eq. (2-9)

$$\begin{aligned} &G_j T_{j-1}^{n+1} + H_j T_j^{n+1} + I_j T_{j+1}^{n+1} + K_j u_{j-1}^{n+1} + L_j u_j^{n+1} + M_j u_{j+1}^{n+1} \\ &\qquad = -G_j T_{j-1}^{n+1} + P_j T_j^{n+1} - I_j T_{j+1}^{n+1} + K_j u_{j-1}^{n+1} + L_j u_j^{n+1} + M_j u_{j+1}^{n+1} \end{aligned} \tag{2-14}$$

- Internal BC, Eq. (2-10):

$$\begin{aligned} u_0 &= X_1 u_2 + Y_1(t) \\ T_0 &= X_3(t) T_2 + X_4(t) \mathrm{T}_f(t) \end{aligned} \tag{2-15}$$

- External BC, Eq. (2-11):

$$\begin{aligned} u_{M+1} &= X_2 u_{M-1} - Y_2(t) \\ T_{m+1} &= X_5(t) T_{m-1} + X_6(t) \mathrm{T}_\infty \end{aligned} \tag{2-16}$$

The detailed step-by-step derivation has been provided in Appendix A. Eqs. (2-13) and (2-14) may be cast into the matrix form as illustrated in Eq. (2-17), where matrices $\boldsymbol{A}$ to $\boldsymbol{H}$ are coefficient matrices, vectors $\{v_1\}$, and $\{v_2\}$ are temperature and displacement vectors, and $\{c_1\}$ and $\{c_2\}$ are constant vectors, respectively. The detailed description and components are presented in appendix A.

$$\begin{bmatrix} [\boldsymbol{A}]_{J\times J} & [\boldsymbol{B}]_{J\times J} \\ [\boldsymbol{E}]_{J\times J} & [\boldsymbol{F}]_{J\times J} \end{bmatrix}_{2Jx2J} \begin{Bmatrix} \{v_1\}_{J\times 1} \\ \{v_2\}_{J\times 1} \end{Bmatrix}_{2J\times 1}^{n+1} = \begin{bmatrix} [\boldsymbol{C}]_{J\times J} & [\boldsymbol{D}]_{J\times J} \\ [\boldsymbol{G}]_{J\times J} & [\boldsymbol{H}]_{J\times J} \end{bmatrix}_{2J\times 2J} \begin{Bmatrix} \{v_1\}_{J\times 1} \\ \{v_2\}_{J\times 1} \end{Bmatrix}_{2J\times 1}^{n} + \begin{Bmatrix} \{c_1\}_{J\times 1} \\ \{c_2\}_{J\times 1} \end{Bmatrix} \quad (2\text{-}17)$$

It is worthy mentioning that, the first and last lines in coefficient matrices (corresponding to the thick-walled cylinder inner and outer boundaries) are determined using the boundary conditions (provided in appendix A).

2.4 Results and Discussions

In this section, the developed numerical model is used to predict thick-walled cylinders' temperature and stress variations due to different loading conditions. In order to better present the outputs of the first two examples, the results are presented in non-dimensional forms of time t^* and radius r^*, where $t^* = \frac{v\,t}{R_o - R_i}$ and $r^* = \frac{r - R_i}{R_o - R_i}$. Consequently, the boundaries of radial position r are changed from $[R_i\text{-}R_o]$ to [0-1] in the non-dimensional form. On the other hand, the stress wave needs a non-dimensional time of 1 to travel from the inner surface to the outer surface of the cylinder and needs the same time for reflection. In other words, the required time for the upfront stress wave ranges [0-1] while it ranges [1-2] for the reflected wave.

Table 2-1 Geometry, material properties, initial and loading conditions.

Geometry		Initial conditions	
$R_i = 50$	mm	$T(R_i, t) = 21$	^oC
$R_o = 100$	mm	$\sigma_r(R_i, t) \approx 0$	Mpa
Material Properties		Boundary conditions	
ρ =7060	Kg/m^3	$T(r\,, t) = 200$	^oC
$k = 204$	$W/m\,K$	$\sigma_r(R_i, t) = 0$	Mpa
$\alpha = 10 \times 10^{-6}$	$^oC^{-1}$	$\sigma_r(R_o, t) \approx 0$	Mpa

2.4.1 Thermal load

For the purpose of validating the model results with published studies, consider a thick-walled cylinder under uniform temperature through its thickness. Table 2-1 lists the thick-walled cylinder geometry, material properties, initial conditions, and loading conditions, as same as published studies [120, 121].

Figure 2-3 shows the dynamic radial and hoop stresses at the mid-section of the thick-walled cylinder due to thermal load. It is noticed that there is a good agreement between both the proposed model and published studies; therefore, the developed FD model has an acceptable degree of accuracy.

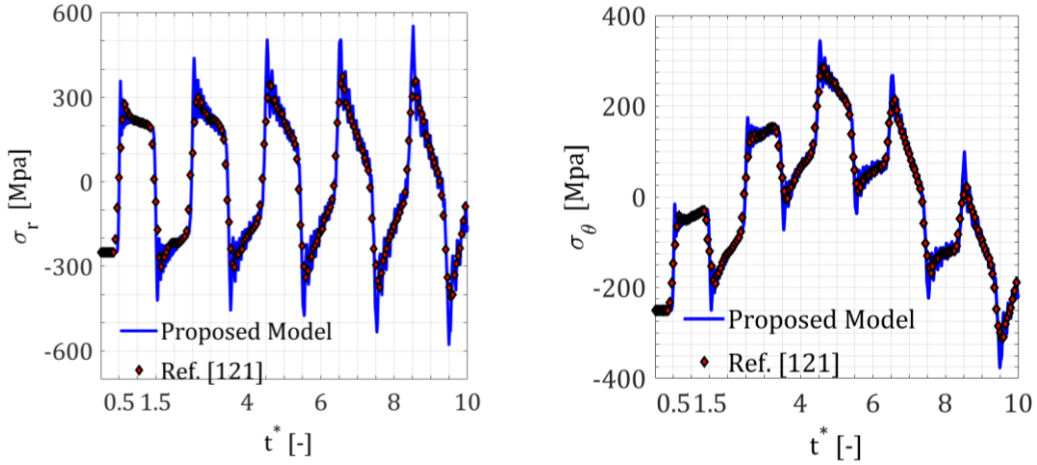

(a) Radial stress (b) Hoop stress

Figure 2-3. Stresses-time history at the mid-radial position.

In Figure 2-3, the first two sudden jumps of stresses at non-dimensional times of 0.5 and 1.5 represents the first upfront stress wave and its reflection, respectively. As from Eq. (2-5), the stress wave velocity, for this example, is 3.18 km/s. Thus, the upfront stress wave takes a non-dimensional time t^* of 0.5 to reach the mid-radial position. On the other hand, the reflected wave takes a t^*=1.5 to reach the same position.

2.4.2 Sudden mechanical shock

This example investigates the thermal and elastic behaviors of a thick-walled cylinder made of steel 4130 under internal mechanical shock (sudden internal pressure of 300 MPa). This simple loading condition is selected to clearly investigate the thermal response due to the absence of

thermal load. The thick-walled cylinder geometrey, material properties, the initial and boundary conditions are listed in Table 2-2.

According to the loading conditions stated in Eqs. (2-10) and (2-11), the values of w_{ij} are equal to zero except $w_{11}, w_{12}, w_{31}, and\ w_{32}$, and their values are: $\frac{1}{R_i}\frac{E\nu}{(1+\nu)(1-2\upsilon)}$, $\frac{E(1-\nu)}{(1+\nu)(1-2\upsilon)}$, $\frac{1}{R_o}\frac{E\nu}{(1+\nu)(1-2\upsilon)}$, and $\frac{E(1-\nu)}{(1+\nu)(1-2\upsilon)}$, respectively.

Table 2-2. Material and geometrical properties

Geometry		Initial conditions	
$R_i = 3.81$	mm	$T(R_i, t) = 21$	^oC
$R_o = 10$	mm	$\sigma_r(R_o, t) \approx 0$	Mpa
Material Properties		Boundary conditions	
ρ =7845	Kg/m^3	$T(R_i, t) = 21$	^oC
$k = 42.63$	$W/m\ K$	$T(r\ , t) = 21$	^oC
$\alpha = 10.4 \times 10^{-6}$	$^oC^{-1}$	$\sigma_r(R_i, t) = -300$	Mpa
$C = 470$	$J/Kg\ K$	$\sigma_r(R_o, t) \approx 0$	Mpa

Using Eq. (2-5), the stress wave velocity, for this example, is 6 km/s. Thus, the upfront stress wave takes around 1.03 μs to propagate through the thickness of the cylinder from the inner to the outer surfaces and takes the same period for reflection. Thus, it is better to present the results in the non-dimensional forms of time and radial position.

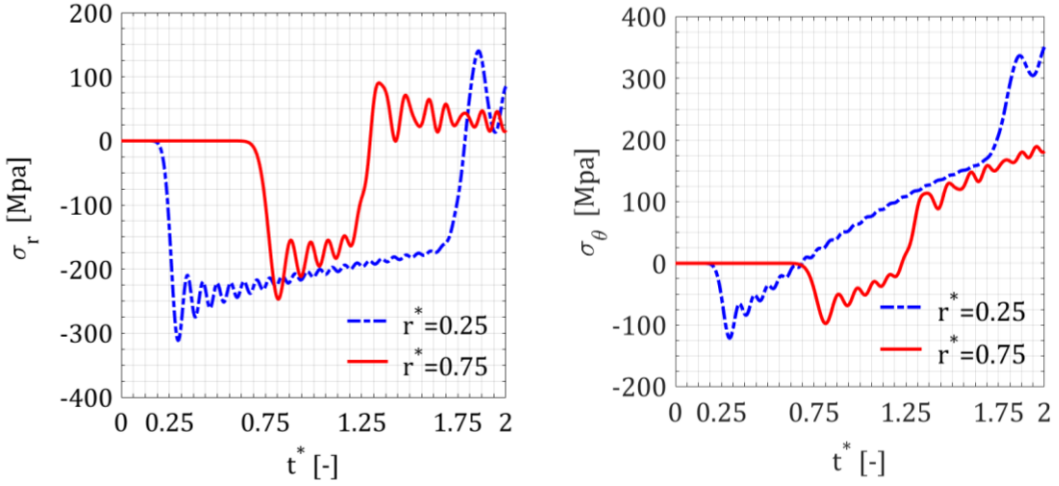

(a) Radial stress (b) Hoop stress

Figure 2-4. Stresses-time history at specific non-dimensional radial positions.

Figure 2-4 shows the time-history results for the radial and hoop stresses at non-dimensional radii of 0.25 and 0.75. The radial and hoop stresses at r* of 0.25 and 0.75 are zero till t* of 0.25 and 0.75, respectively. According to the stress wave speed, the stress wave takes t* of 0.25 and 0.75 to reach r* of 0.25 and 0.75 from the inner surface, respectively.

Figure 2-5 depicts the radial stress wave variations through the thickness of the thick-walled cylinder at specified times. The selected non-dimensional times are 0.25, 0.75 for the upfront wave in the solid line and 1.25, 1.75 for the reflected wave in the center line. The upfront stress wave takes nearly t* of 0.25 and 0.75 to reach non-dimensional radii of 0.25 and 0.75, respectively. On the other hand, the reflected wave takes t* of 1.75 and 1.25 to reach r* of 0.25 and 0.75, respectively. From Figure 2-5, the t* between the upfront and the reflected waves to reach r* of 0.25 and 0.75 equals nearly 1.5 and 0.5. This clearly illustrates the time of action of stresses in Figure 2-4 at r* of 0.25 and 0.75.

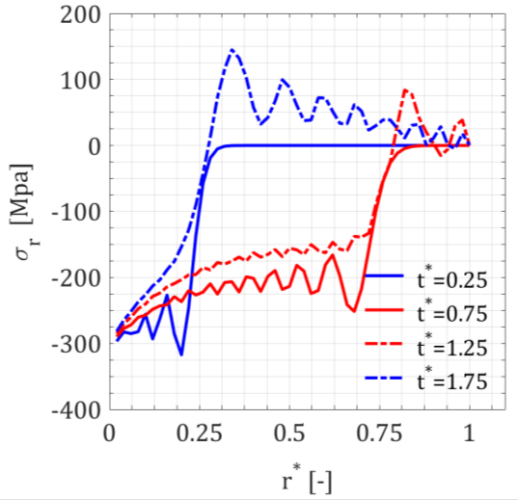

Figure 2-5. Radial stress variation through-thickness at specific t*.

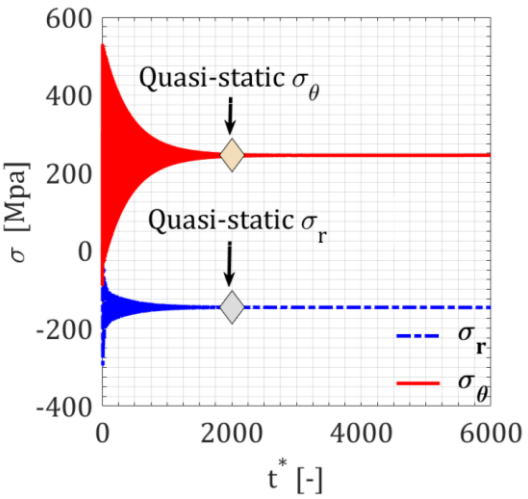

Figure 2-6. Radial Stress attenuation-time history at specific r*

It is interesting to note that the quasi-static internal pressure generates compressive radial and tensile hoop stresses throughout the entire thickness of the thick-walled cylinder. However, under the shock pressure load, as shown in Figure 2-4(b), the compressive hoop stress starts initially at t* = 0.25, then it approaches the tensile nature after around t* = 0.75.

Figure 2-6 shows the radial and hoop stress attenuation with more extended time at a non-dimensional radial position of 0.25. Results show that after nearly 2000 stress wave cycles (nearly

2 ms), the radial and hoop stresses reach steady-state conditions with values similar to those under quasi-static pressure (using the hypothesis of static-uncoupled thermo-elasticity). However, before reaching the steady-state conditions, the coupled thermo-elasticity model predicts higher stresses than the static-uncoupled model. Therefore, it is better to consider coupled thermo-elasticity models, especially in thick-walled cylinder applications prone to sudden boundary conditions.

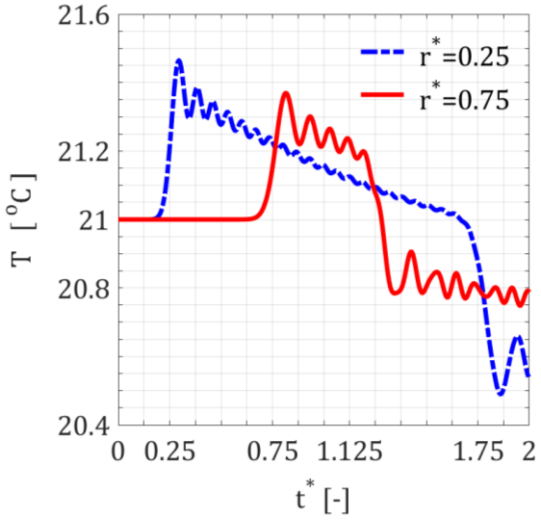

Figure 2-7. Temperature-time history at specific non-dimensional radial positions.

Figure 2-7 depicts the time variation of the temperature waves at non-dimensional radial positions of 0.25 and 0.75. Interestingly, while the thick-walled cylinder is only subjected to a mechanical load, a temperature variation is observed due to internal molecular friction.

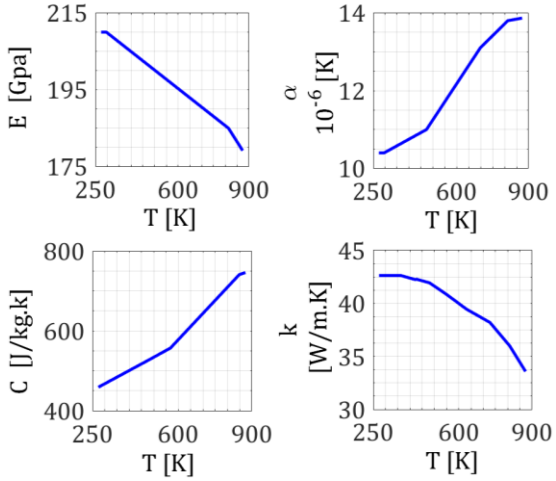

Figure 2-8. Material properties of steel 4130 variations with temperature

2.4.3 Cyclic time-dependent thermo-mechanical shocks

This example investigates a temperature-dependent thick-walled cylinder due to cyclic time-dependent thermo-mechanical shock (machine gun barrel under continuous shooting). The thick-walled cylinder material is 4130 steel, and its material properties variation with temperature is shown in Figure 2-8 [122], while the geometry is listed in the first section of Table 2-2.

Firstly, let's introduce the internal and external boundary conditions in some detail, as follows:

Internal boundary conditions

The inner surface of the thick-walled cylinder is subjected to cyclic nonlinear thermo-mechanical shocks. Each shock consists of a 5 ms loading period, as in Figure 2-9, and a 95 ms unloading period to produce a complete shock of 100 ms, as shown in Figure 2-10. The time axis in Figure 2-10 is put in log scale to clearly depict the first few milliseconds which represent the loading period. These loads are generated due to the burning of 1.63 gm of double-base propellant [123]. As in Figure 2-9, the loads' effect reaches after 0.6 ms the position of calculations; this position is far about 178 mm from the load source section (chamber section). Also, this position is the same as the experimental measurement, which will be explained in the next section.

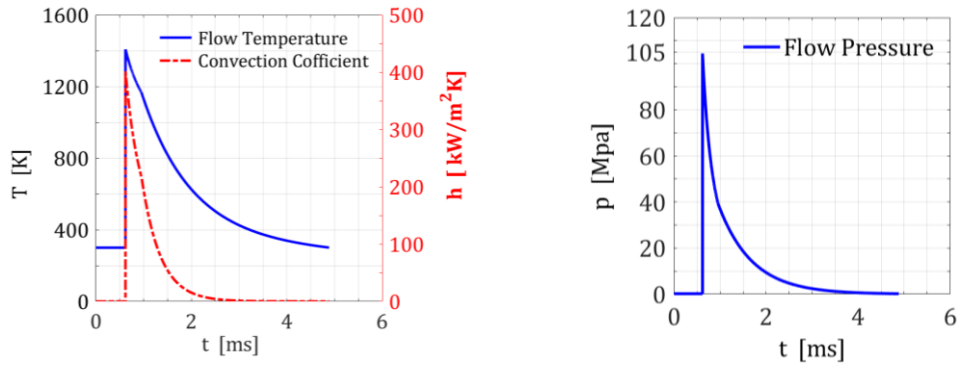

Figure 2-9. Applied thermo-mechanical loads during the loading period at the inner surface of the thick-walled cylinder, 178 mm from the load source section.

The inner thermal boundary condition is represented, based on Newton's law of cooling and continuity [124], as follows

$$\mathrm{k}\frac{\partial T}{\partial r}\Big]_{r=R_i} = \mathrm{h}_f\left(T - T_f\right)$$

while the mechanical boundary condition is represented as:

$$\mathrm{p}(R_i, t) = p_f(t)$$

where $h_f, T_f, and\ p_f$ are the convection coefficient, temperature, and pressure of the inner gas flow.

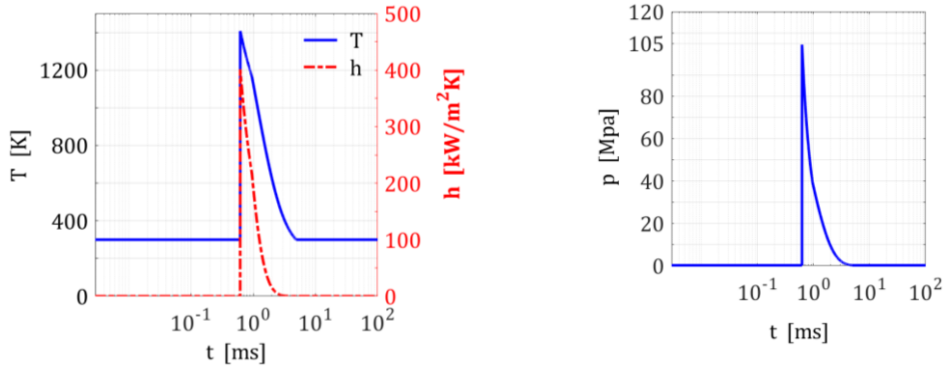

Figure 2-10. Applied thermo-mechanical loads for a complete cycle at the inner surface of the thick-walled cylinder, 178 mm from the load source section.

External boundary conditions

The outer surface of the thick-walled cylinder is only affected by ambient conditions (no external forces). Consequently, the thermo-mechanical outer boundary condition becomes

$$k\frac{\partial T}{\partial r}\Big]_{r=R_o} = h_\infty(T_\infty - T)$$

$$p(R_o, t) = p_\infty$$

where $h_\infty, T_\infty, and\ p_\infty$ are the free convection coefficient, ambient temperature, and ambient pressure. The values are considered constant with values of 15 W/m^2K, 300 K, and 0.1013 Mpa, respectively.

Before delving into the experimental setup, let us discuss the phenomenon of thermal accumulation in some detail.

a) Thermal accumulation

In fact, the time between two successive input loads is insufficient to allow the cylinder to reach its initial conditions. Consequently, a part of thermal energy is stored inside the cylinder thickness, then it accumulates during the successive loading to introduce the so-called "thermal accumulation." This thermal accumulation causes variations in both stress and temperature distributions through the cylinder thickness. To better realize this, ten successive nonlinear thermo-mechanical shocks are applied at the inner surface of a thick-walled cylinder, each shock as in

Figure 2-10. The calculations are performed based on the developed model considering the two hypotheses of TIMP and TDMP. The material properties for the case of TIMP are listed in the first section of Table 2-2, while Figure 2-8 represents the material properties for the case of TDMP.

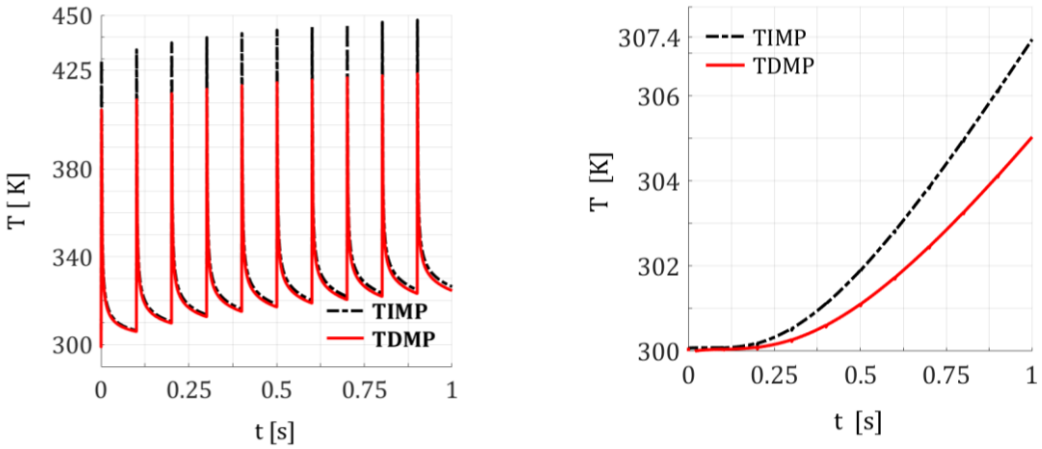

(a) Inner surface (b) Outer surface

Figure 2-11. Temperature-time history of the tube boundaries for 10 cycles.

Figure 2-11 depicts the temperature variation at the thick-walled cylinder's inner and outer surfaces due to the ten successive time-dependent thermo-mechanical shocks considering both TIMP and TDMP hypotheses. For the two hypotheses, Figure 2-12 also shows the temperature variation through the thickness of the thick-walled cylinder after applying the ten successive thermo-mechanical shocks.

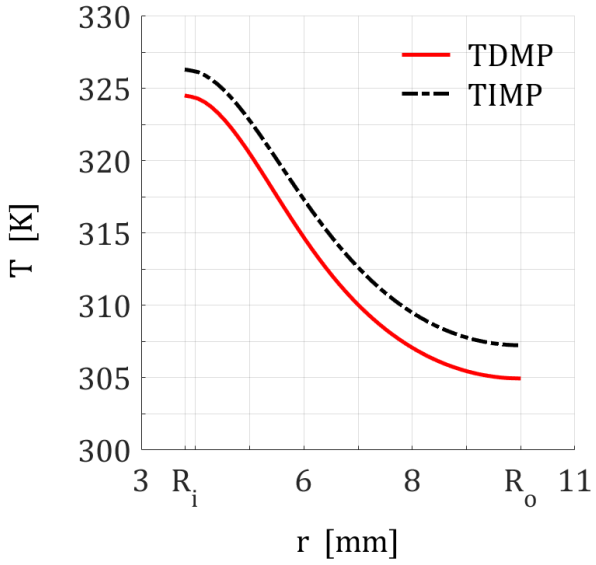

Figure 2-12. The temperature variation through the cylinder thickness after the 10 cycles.

As in Figure 2-11, the temperature after each cycle does not reach the initial temperature (300 K in this example), which clearly defines the thermal accumulation due to successive thermal cycles. Also, examining the results in Figure 2-11 and Figure 2-12, the maximum inner surface temperature is 425 K and 449 K under the hypothesis of TDMP and TIMP, respectively. Also, the inner surface temperature after applying ten successive cycles is 324.9 K and 327 K, while the anticipated temperature at the outer surface is 305 K and 307.4 K for TDMP and TIMP, respectively. These values conclude that the temperature values in the case of TDMP are noticeably lower than those in the case of TIMP. Figure 2-8 illustrates the reason, as the material's ability to store thermal energy increases with temperature increase while its values of thermal conductivity decrease. In other words, according to the first law of thermodynamics, part of the applied thermal energy will be stored in the cylinder material, and the other part will transfer through the thickness and then to the surrounding. Due to temperature increases, the cylinder's ability to store heat increases, so the stored energy part increases while the conducted thermal part decreases. Therefore, the temperature values in the case of TDMP are lower than those in the case of TIMP.

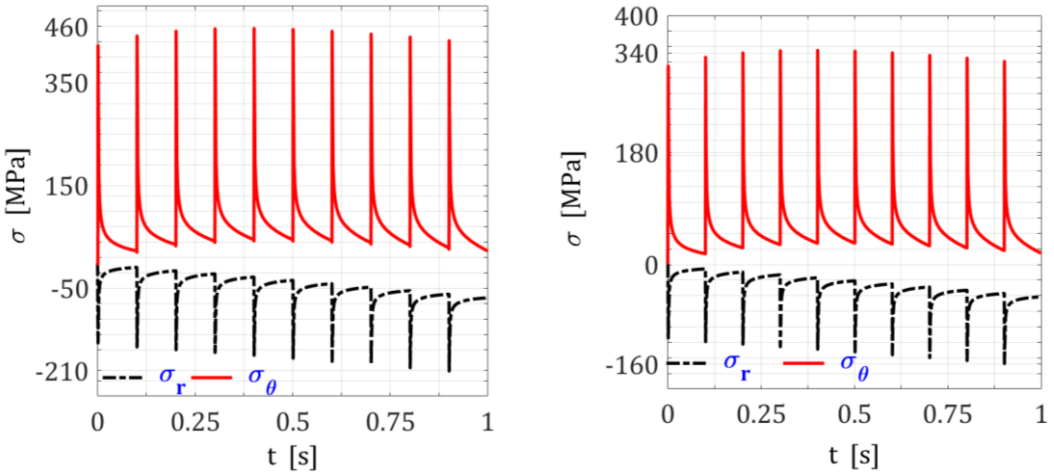

(a) TIMP (b) TDMP

Figure 2-13. Stresses-time history at the mid- radial section of the thick-walled cylinder due to 10 cycles.

Figure 2-13 depicts the hoop stress variation at the middle-radial surface of the thick-walled cylinder due to ten successive shocks considering both TIMP and TDMP hypotheses. The TIMP hypothesis predicts a maximum compressive radial and tensile hoop stress at the tenth cycle of around 210 and 450 MPa at the mid-wall, while it equals, respectively, 160 and 370 MPa in the

case of TDMP. Therefore the TIMP also overestimates the stress values compared to TDMP. Eq. (2-2) shows the reason, as TIMP overestimates the predicted temperature; therefore, it also overestimates the predicted stresses compared with TDMP.

Adding relaxation periods after successive shocks may be used to control thermal accumulation. To better recognize that, 5 s relaxation time is added after the ten successive loads for the previous loads. Figure 2-14 displays the temperature variation at a temperature-dependent thick-walled cylinder's inner and outer radii due to ten successive shocks in 6 s. The first second in the time axis represents the time of the ten successive shocks, while the rest of the time represents the 5 s relaxation period. It easily realizes the mitigation of thermal accumulation during the relaxation period.

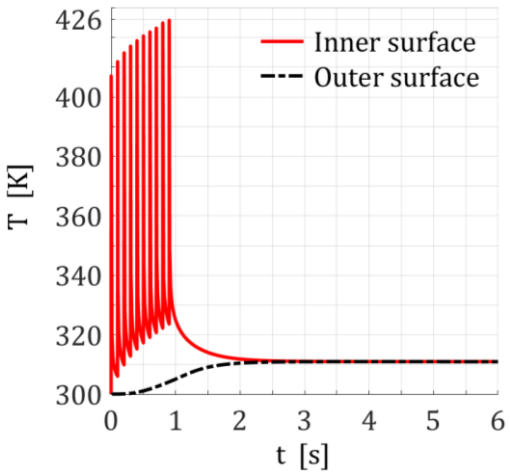

Figure 2-14. The temperature variation during the 10 cycles in 6 s under the hypothesis of TDMP.

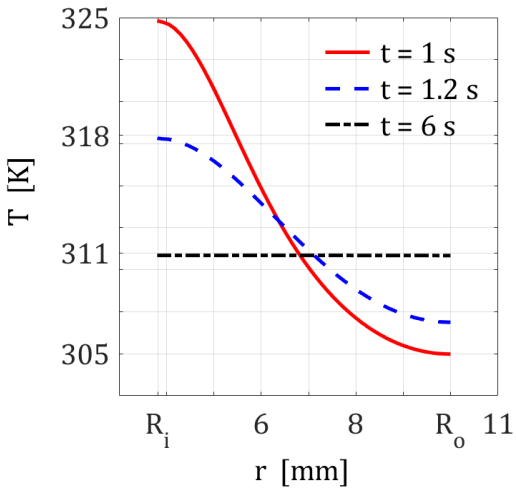

Figure 2-15. The temperature profile through the cylinder thickness under the hypothesis of TDMP.

To better illustrate it in more detail, Figure 2-15 represents the temperature variation through the cylinder thickness after different relaxation periods. These three plots in Figure 2-15 depict the profile at 6 s, 1.2 s, and just after applying ten cycles, corresponding to 5 s, 0.2 s, and 0 s relaxation periods, respectively. The temperature difference between the cylinder surfaces dropped by 7 K by applying a 0.2 s relaxation time, while the temperature is uniformly distributed after a relaxation time of 5 s.

Figure 2-16 shows the time history of dynamic radial and hoop stresses at the intermediate radius of the thick-walled cylinder due to the prementioned loads. Although, after the relaxation

period, the temperature is uniformly distributed, as in Figure 2-15, the stresses did not vanish. This is because the temperature of the thick-walled cylinder is not reached the initial temperature. Also, it is interesting to mention that the residual temperature generates compressive residual hoop stress, which enhances the thick-walled cylinder's performance [125].

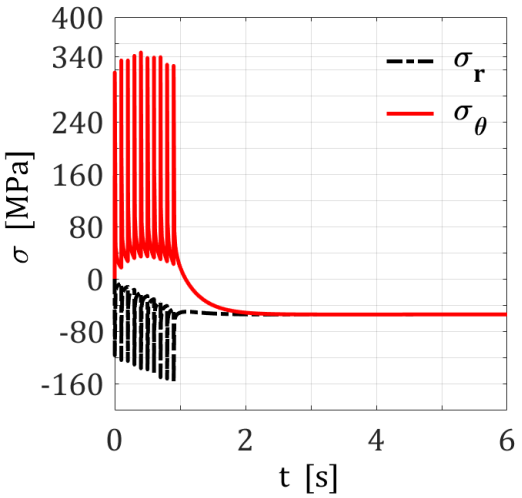

Figure 2-16. Stresses-time history at the mid- radial section of the temperature-dependent thick-walled cylinder due to 10 cycles in 6 s.

Therefore, from the thick-walled cylinder design point of view, the TDMP hypothesis is better than the TIMP hypothesis as it underestimates compressive residual hoop stress variation through the cylinder thickness. Also, the TDMP hypothesis is better than the TIMP hypothesis if it can predict accurate results compared with the TIMP hypothesis.

b) Experimental Study

An experimental study has been designed to further investigate the impact of considering the TDMP hypothesis on the accuracy of results. The measurements are performed on a real machine gun barrel under burst shooting. The barrel has the same dimensions and material properties as those in Table 2-2 and Figure 2-8. The sketch of the experimental setup is shown in Figure 2-17.

The inner surface of the cylinder is subjected to 85 cyclic nonlinear thermo-mechanical shocks with a particular regime of fire. The regime of loading consists of 3 bursts of pulses, two bursts of 30 pulses, followed by a burst of 25 pulses. Each burst is followed by a relaxation period, as shown in Figure 2-18.

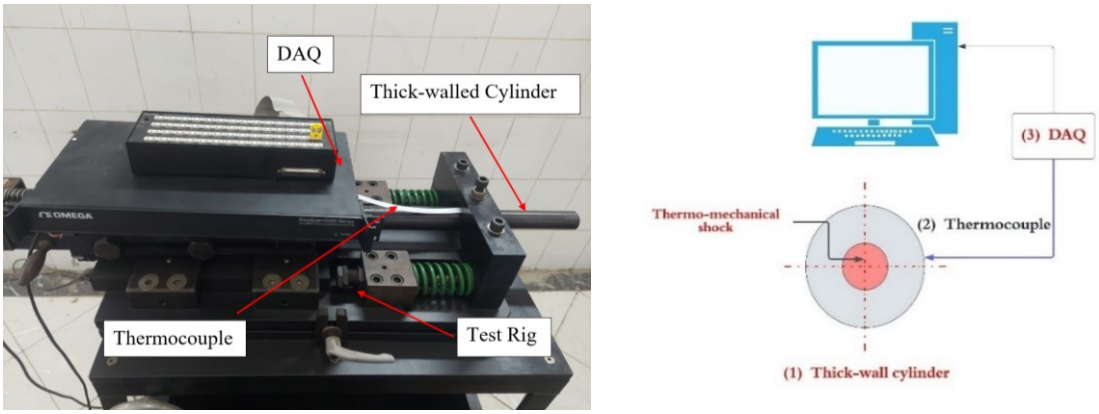

Figure 2-17. Schematic drawing of the experimental setup.

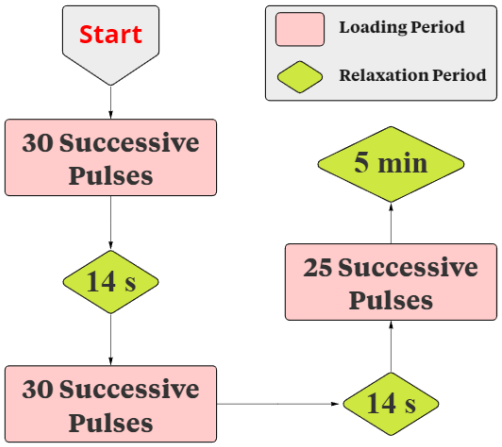

Figure 2-18. Schematic representation of applied thermo-mechanical shocks.

Each thermo-mechanical shock represents the loads due to the propellant burning, as shown in Figure 2-10 [123]. The outer surface temperature of the cylinder is measured using a highly sensitive thermocouple type K (Chrome-Aluminium) with a diameter of 0.5 mm. It is too difficult to directly fix the thermocouple at the axial section of the load source (chamber section); consequently, the measurement is performed at a distance of 178 mm from the load source section.

The thermocouple signal is processed using a data acquisition system with a maximum sampling rate of 200 kHz. The relaxation time after each burst of shocks is the time consumed during the reloading of new bolts. Also, this relaxation time is necessary to enhance the measurement results as the duration of the applied loads is too short.

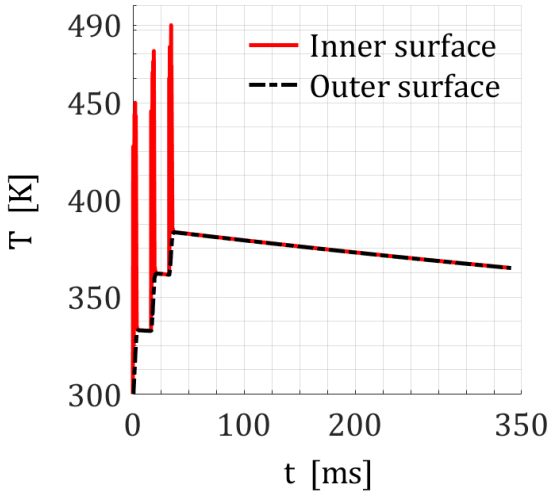

Figure 2-19. Inner and outer surface temperatures for applying 85 shocks under the hypothesis of TDMP.

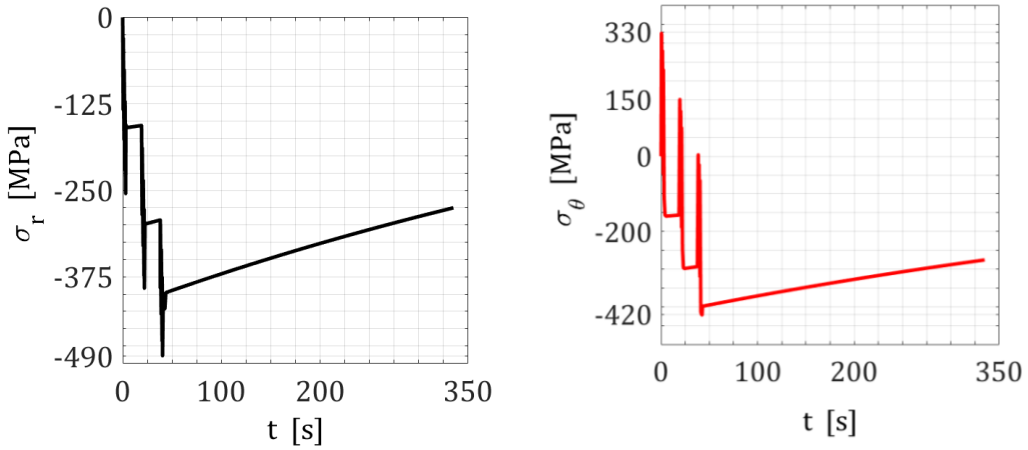

(a) Radial stress (b) Hoop stress

Figure 2-20. Stresses-time history at the mid-radial section of the temperature-dependent barrel cylinder due to 85 thermo-mechanical shock pulses.

Figure 2-19 shows the predicted temperature-time history at the inner and outer surfaces of the temperature-dependent barrel cylinder due to 85 nonlinear thermo-mechanical shocks. The transient temperature spikes for each successive burst of thermo-mechanical shocks appear as one thick line for each burst due to the used time scale. The temperature peak always increases between each subsequent shock due to heat accumulation. During the relaxation period, the temperature difference between the inner and outer surfaces of the thick-walled cylinder becomes negligible.

Figure 2-20 depicts the time history of the dynamic radial and hoop stresses at the intermediate surface of the thick-walled cylinder. It is noteworthy to point out that, as in Figure 2-20(b), the

hoop stress with time pass becomes compressive due to the effect of thermal loads. On the other hand, the stress spikes almost have the same length of around 340 MPa, and it is always upward. In fact, this is the effect of mechanical loads. In brief, the mechanical load effect is not changed with subsequent cycles, and it has a maximum tensile hoop and compressive radial stresses of 315 and 105 MPa, respectively. In comparison, the thermal load causes the shifting down of these values and changes the hoop stress from tensile to compressive.

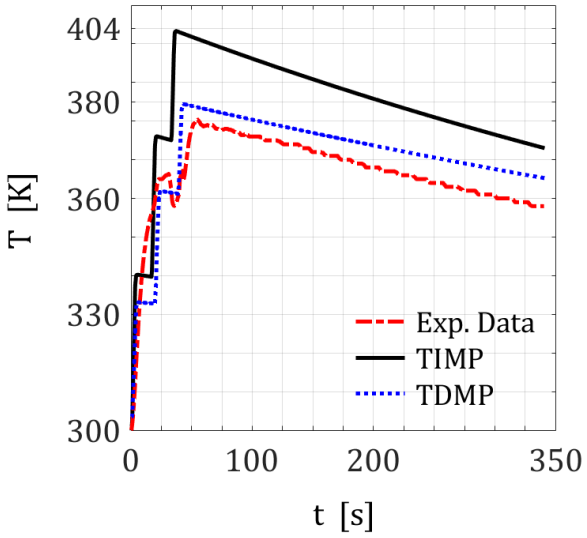

Figure 2-21. Temperature-time history of the outer surface of the temperature-dependent thick-walled cylinder due to 85 shocks.

Figure 2-21 shows a thick-walled cylinder's measured and predicted outer surface temperature-time history due to the predefined regime. The predicted temperature is performed considering the two hypotheses of TDMP and TIMP. The results show a good agreement between calculated results based on TDMP and experimental results. Simultaneously, model-based TIMP could not accurately capture the thermal response, particularly at the end of the third burst of shocks and after that. The maximum measured temperature is 380 K, compared with 385 K and 404 K for TDMP and TIMP, respectively. In comparison, the measured temperature after the completion of the load cycles and subsequent relaxation is 358 K, compared with 364 K and 374 K for TDMP and TIMP, respectively. The maximum error between model-based TDMP and experiment was less than 3%, while that between the model-based on TIMP and experiment was around 10%.

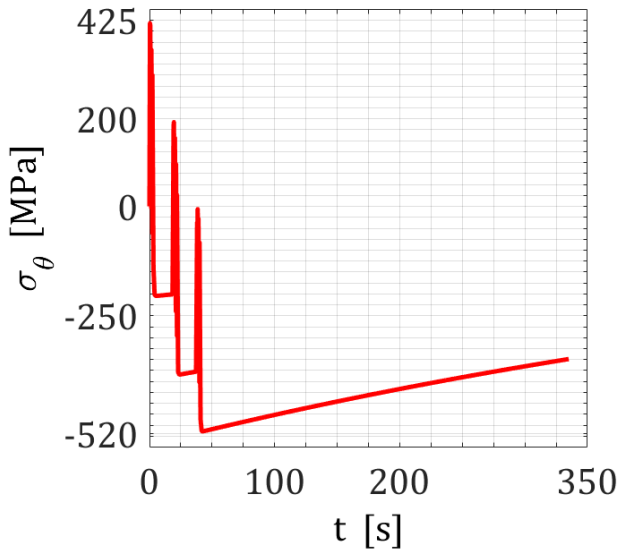

Figure 2-22. Hoop stress-time history at the mid- radial section of the thick-walled cylinder due to 85 pulses under the hypothesis of TIMP.

Figure 2-22 displays the dynamic hoop stress's time history at the thick-walled cylinder's intermediate surface, considering TIMP. As in Figure 2-22 and Figure 2-20(b), the maximum compressive hoop stress is 520 MPa and 420 MPa for TIMP and TDMP, respectively. In fact, Figure 2-20(b) to Figure 2-22 highlight the positive impact of considering TDMP on the accuracy of results which also guarantees an accurate thick-walled cylinder design.

2.5 Conclusion

The main subject of this study is to investigate the coupled thermo-elastic behaviors in temperature-dependent thick-walled cylinders under cyclic nonlinear thermo-mechanical loads. To achieve this, firstly, the governing equations addressing the classical coupled thermo-elasticity in cylindrical coordinates considering material nonlinearities are formulated. Then a detailed numerical solution is presented to predict the displacement and temperature fields. The proposed numerical solution is based on the implicit finite difference using the Crank-Nicolson scheme. This proposed solution of the classical coupled thermo-elasticity represents the temperature and stress fields to a reasonable level of accuracy for different boundary conditions. The model reveals that, before reaching the steady state condition, the coupled thermo-elasticity model predicts higher thermo-elastic behaviors than the uncoupled models. Thus, it is better to consider the coupled model in structures under sudden boundary conditions.

Secondly, an experimental setup is designed to deeply compare the TDMP model results and the TIMP model results with experimental data. Therfore, the outer surface temperature of a machine gun barrel is measured using a highly sensitive thermocouple. The machine gun is under burst shooting. Based on the temperature measurement, the model results had good agreement with the experimental data in the case of TDMP, with a maximum error of 3% compared with a maximum error of 10% for the case of TIMP. Also, TIMP overestimates temperature and stresses, which badly affects thick-walled cylinder design.

Finally, to the best of the authors' knowledge, this is the first time that the classical nonlinear coupled thermo-elasticity has been investigated under cyclic nonlinear thermo-mechanical loads. Moreover, the comparative study has been conducted between two hypotheses, TIMP and TDMP. More generally, the proposed model can be used for trade studies to design lightweight thick-walled cylinders according to their severe operating conditions.

CHAPTER 3

ANALYTICAL FORMULATION TO PREDICT RESIDUAL STRESSES IN THICK-WALLED CYLINDERS SUBJECTED TO HOOP WINDING, SHRINK-FIT, AND CONVENTIONAL AND REVERSE AUTOFRETTAGES

Authors: Mohamed Elfar, Ramin Sedaghati, and Ossama R. Abdelsalam [126].
Status before thesis submission: Submitted to ASME-Journal of Pressure Vessel Technology. Initially submitted on: 19th April 2023. / (Under Review).

Abstract

Shrink-fit, wire-winding, and autofrettage processes and their combinations can be effectively used to increase the strength and fatigue life of thick-walled cylinders for a given volume. While several numerical solutions have been developed for determining the residual stress profile through the thickness of thick-walled cylinders for different combinations of the shrink-fit and autofrettage processes, there are no analytical solutions available to predict the residual stress profile induced by the combination of the shrink-fit and inner and outer autofrettage processes with the hoop winding. In this study, the analytical formulations to predict the residual stress distribution for various combinations of the three processes (hoop-winding, shrink-fit, and autofrettage) have been formulated considering the same manufacturing sequences. The results demonstrate that combinations that include the wire-winding process significantly improve the residual stress profile through the wall thickness of single or two-layer thick-walled cylinders.

3.1 Introduction

Thick-walled cylinders play an essential role in many industrial structures due to their ability to safely store and transmit fluids under different loading conditions. These structures may be subjected to different loading conditions, including mechanical, thermal, or severe cyclic thermo-mechanical loading conditions. In harsh loading conditions, virgin (mono-block) thick-walled cylinders may not be able to sustain the applied loads unless they are designed to be very thick and heavy, which is not practical. Shrink-fit, wire-winding, and autofrettage processes, as shown in Figure 3-1, have been developed to substantially increase the load-carrying capacity per volume of thick-walled cylinders [2]. These processes mainly generate a beneficial compressive stress near the bore region, which counteracts the tensile stresses that would normally develop during operational cyclic loading, thus enhancing the fatigue lifetime of thick-walled cylinders. The wire-winding process generates a compressive stress near the bore region through hoop winding of the outer surface of the cylinder, while the inner layer is put under compression by the outer layer in the case of the shrink-fit process. Unlike the wire-winding and shrink-fit processes, the autofrettage process is induced by overloading a thick-walled cylinder bore, which produces permanent deformation near the bore region. After removing the load, a compressive residual stress is introduced near the bore due to the elastic recovery of the outer part.

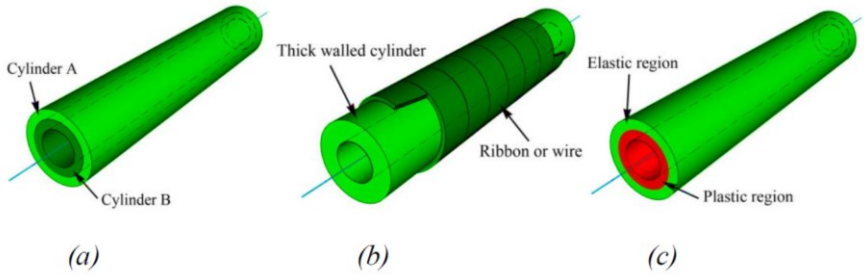

Figure 3-1. Methods of strengthening thick-walled cylinders (a) shrink-fit two-layer cylinder; (b) wire-wounded thick-walled cylinder; and (c) autofrettage thick-walled cylinder [2]

The prediction of the residual stresses induced by the reinforcement processes is of paramount importance for the optimal design of thick-walled cylinders. Wire-winding [12, 13] and [127], shrink-fit [26– 29], and autofrettage [36, 58, 63] and [128– 131] processes have been widely used individually to reinforce thick-walled cylinders to enhance their load-carrying capacity. Several limitations associated with each process have been reported [75, 89]. These can be summarized as: (a) limited compressive stresses near the bore area for both the wire-winding and shrink-fit

processes compared with the autofrettage process; (b) in the shrink-fit process, the internal stress changes from compressive to tensile at the interface surface between the two layers, and high tensile stress is also produced at the outer surface of the outer layer. (c) The Bauschinger effect has a negative effect on the compressive stress developed by the autofrettage process [59, 60]. As a result, different combinations of shrink-fit and autofrettage processes are proposed to alleviate the above limitations and enhance the compressive residual stress distribution through the wall thickness [4, 75], and [77].

Kapp et al. [66] suggested a multi-layer design for thick-walled cylinders under cyclic mechanical loading conditions to enhance their fatigue lifetimes by compounding an outer virgin tube with an auto-fretted inner one. After autofrettage of the inner tube, the shrink-fit process increases the compressive residual stress close to the bore area of the inner tube. However, as a consequence of the Bauschinger effect, the inner region is more likely to re-yield, thus substantially reducing the beneficial effect of the autofrettage process. Several studies have suggested removing material from the inner region in an effort to reduce the Bauschinger effect and improve the profile of residual stress throughout the wall thickness [68– 70]. Parker [67] proposed an innovative approach to overcoming re-yielding by shrink fitting two virgin tubes prior to autofrettage of the entire assembly. This leads to a reduction in plastic strain near the bore region after autofrettage of roughly 50% compared with single layer autofrettage. Reduction of the plastic strain lessens the Bauschinger effect and prevents the loss of beneficial residual stress close to the bore area.

Yuan et al. [72] proposed another configuration of a thick-walled cylinder by shrinking two inner and outer cylinders after the inner autofrettage procedure was conducted on both the inner and outer layers. Results suggested that an increase in the compounding pressure enhanced the compressive residual stress through the inner cylinder wall but increased the unfavourable tensile stress of the outer cylinder. Notably, the increasing tensile stress at the outer surface of thick-walled cylinders may shorten their service life if they are likely to be exposed to outer surface fatigue. To address this issue, Parker [56] developed a reversed autofrettage process, also known as the outer autofrettage process [73], in which the outer surface of a thick-walled cylinder is overloaded to reduce tensile residual stress on the tube's outer surface. He introduced a new configuration for shrinking a traditional autofrettage inner layer with a reverse autofrettage outer layer. This configuration achieves the same advantages as Yuan's configuration [72] for the inner

tube. Moreover, unlike Yuan's configuration, the proposed configuration reduces the detrimental residual hoop stress at the outer surface.

While many studies have been conducted to propose various combinations of autofrettage and shrink-fit compound cylinders in an attempt to increase the fatigue life, there are limited studies on the analytical analysis of these combinations. In addition, to the best of our knowledge, no study has been conducted on the analytical determination of the residual stress profile through the wall thickness for thick-walled cylinders subjected to combined wire-winding, shrink-fit, and autofrettage processes. The present study aims at the development of analytical formulations to predict the residual stress distribution for different combinations of the wire-winding, shrink-fit, and autofrettage processes.

This article is structured as follows: the main governing equations addressing the residual stress profile through the wall thickness are formulated in Section 3.2. This is followed by the detailed analytical solution of the residual stress profile using different processes and their different combinations in Section 3.3. Summary and conclusions are finally provided in Section 3.4.

3.2 Main Governing Equations

Let us consider a closed-end thick-walled mono-block cylinder made of isotropic material with an inner radius R_i and an outer radius R_o subjected to axisymmetric loading conditions. Under the axisymmetric plane strain conditions ($\varepsilon_z = 0$), the constitutive relations relating the elastic strains to stresses may be expressed as [116]:

$$\begin{aligned} {\varepsilon_r}^e &= \frac{(1+\nu)}{E}[(1-\nu)\sigma_r - \nu\sigma_\theta] \\ {\varepsilon_\theta}^e &= \frac{(1+\nu)}{E}[(1-\nu)\sigma_\theta - \nu\sigma_r] \end{aligned} \tag{3-1}$$

The strain–displacement relations in cylindrical coordinates can be described as [116]:

$$\begin{aligned} \varepsilon_r &= \frac{\partial u_r}{\partial r} \\ \varepsilon_\theta &= \frac{u_r}{r} \end{aligned} \tag{3-2}$$

The equilibrium equation, in the absence of shear stresses and ignoring the body forces, may be formulated as follows [92]:

$$\frac{d\sigma_r}{dr} + \frac{\sigma_r - \sigma_\theta}{r} = 0 \tag{3-3}$$

The Prandtl-Reuss equation considering plastic axial strain, $\varepsilon_z^p = 0$, is expressed as [132]:

$$d\varepsilon_{eq}^p = \frac{2}{\sqrt{3}} d\varepsilon_\theta^p \tag{3-4}$$

The von Mises yielding criteria, in the case of applied internal pressure, may also be stated as:

$$\sigma_\theta - \sigma_r = \frac{2}{\sqrt{3}} \sigma_{eq} \tag{3-5}$$

in which the equivalent stress as a function of plastic strain, for linear work hardening material, may be written as [58]:

$$\sigma_{eq} = \sigma_Y + E_P \varepsilon_{eq}^p \tag{3-6}$$

where $\varepsilon_r{}^e, \varepsilon_\theta{}^e, u_r, \sigma_r, \sigma_\theta, E, \upsilon, \varepsilon_{eq}^p, \varepsilon_\theta^p, \sigma_{eq}, \sigma_Y, and\ E_P$ are the elastic radial strain, elastic hoop strain, radial displacement, radial stress, hoop stress, Young modulus of elasticity, Poisson's ratio, plastic equivalent strain, plastic hoop strain, equivalent stress, yield strength, and plastic modulus, respectively.

In the case of a purely elastic response, the stresses distribution through the thickness of the thick-walled cylinder of radii R_i and R_o under internal pressure p_i and external pressure p_o may be stated according to the Lame´ solution as [3]:

$$\sigma_r = p_i \left(\frac{R_i^2}{r^2}\right)\left(\frac{r^2 - R_o^2}{R_o^2 - R_i^2}\right) - p_o \left(\frac{R_o^2}{r^2}\right)\left(\frac{r^2 - R_i^2}{R_o^2 - R_i^2}\right) \tag{3-7}$$

$$\sigma_\theta = p_i \left(\frac{R_i^2}{r^2}\right)\left(\frac{r^2 + R_o^2}{R_o^2 - R_i^2}\right) - p_o \left(\frac{R_o^2}{r^2}\right)\left(\frac{r^2 + R_i^2}{R_o^2 - R_i^2}\right) \tag{3-8}$$

On the other hand, for stresses greater than those provided by Eq. (3-5), a plastic zone appears until a radial position of R_c is reached in the thick-walled cylinder, such that for $R_i < r < R_c$, the layer material behaviour is plastic, while for $R_c < r < R_o$, the layer material behaviour remains

elastic. The radius of the elastic-plastic border R_c is mainly dependent on the applied loads. It is worth noting that the Lame' elastic equations are no longer valid in the plastic zone.

The equivalent stress distribution through the plastic zone thickness is determined by considering the incompressibility material criterion ($\varepsilon_r^p + \varepsilon_\theta^p + \varepsilon_z^p = 0$). Besides, as mentioned before, considering $\varepsilon_z^p = 0$ yields:

$$\varepsilon_r + \varepsilon_\theta = \varepsilon_r^e + \varepsilon_\theta^e \tag{3-9}$$

Eliminating ε_r, $\varepsilon_\theta, \varepsilon_r^e$ and ε_θ^e using Eqs. (3-1), (3-2), and. (3-4)- (3-6), the equivalent stress profile through the plastic zone thickness can be obtained as:

$$\sigma_{eq} = \frac{\sigma_Y}{(1 + AE_P)}\left(1 + AE_P \frac{R_c^2}{r^2}\right) \tag{3-10}$$

where $A = 4(1 - \nu^2)/3E$ is a constant value. The detailed step-by-step procedure for calculating σ_{eq} has been provided in Appendix B. It is worth noting that in the case of the plane stress condition ($\sigma_z = 0$), the constant A becomes equal to $4/3E$.

3.3 Determination Of Residual Stresses

In this section, first the analytical models to evaluate the induced internal or residual hoop stress through the thickness of the thick-walled cylinder due to wire-winding, shrink-fit, inner autofrettage, and outer (reverse) autofrettage processes are individually addressed. Then, the analytical solutions for the residual stress distribution for combinations of the aforementioned processes using the same manufacturing sequences have been presented.

3.3.1 Modelling of the Shrink-Fit Process

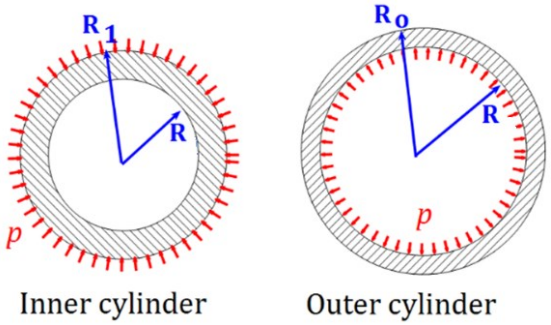

Figure 3-2. Interference pressure due to the shrink-fit process at the inner and outer layers.

The shrink-fit process is an effective technology used in the production of thick-walled cylinders. It involves interferingly compounding two virgin cylinders of relatively small thickness. This process of compounding two cylinders produces a compressive pressure at the outer surface and the inner surface of the inner and outer cylinders, respectively, as shown in Figure 3-2. It is noted that based on the value of shrinking interference between the inner and outer cylinders, the material exhibits purely elastic or elastic-plastic behaviour as described below.

a) Stress components in the case of purely elastic behavior

The interface pressure p generated due to the shrink-fit process can be expressed as [29]:

$$p = \frac{0.5\,\delta}{\frac{R}{E_o}\left(\frac{R_o^2 + R^2}{R_o^2 - R^2} + \upsilon_o\right) + \frac{R}{E_i}\left(\frac{R_i^2 + R^2}{R_i^2 - R^2} - \upsilon_i\right)} \tag{3-11}$$

If the inner and outer layers are made of the same material, the shrink-fit pressure can be simplified as follows:

$$p = \frac{E\delta}{2R^3}\left(\frac{(R_o^2 - R^2)(R^2 - R_i^2)}{R_o^2 - R_i^2}\right) \tag{3-12}$$

where $R_i, R, R_o, \delta, E_i, E_o, \upsilon_i,$ and υ_o are the inner radius of the inner layer, the interface radius between the two layers, the outer radius of the outer layer, shrink-fit clearance, the Young modulus of elasticity of the inner layer and the outer layer, and the Poisson's ratio of elasticity of the inner layer and the outer layer.

The internal stresses distribution through each layer thickness can be simply obtained using Lame´ Eqs. (3-7) and (3-8), considering that the interface pressure acts as an internal pressure for the external cylinder and as an external pressure for the internal cylinder as shown in Figure 3-2.

b) Stress components in the case of elastoplastic behavior

For a sufficiently large shrinking interference, the stress in the compound cylinder approaches the yield limit. Assuming that von Mises' yield criterion governs the yielding behavior, the initial yielding of the compound thick-walled cylinder occurs for the stress values satisfying Eq.(3-5). After yielding begins, the Lame' elastic equations are no longer valid for the yield region. It is worth noting that, according to the compounding interference, the yield zone can be either at the

bore area of the inner layer or at the bore area of the outer layer, or their combination. Thus, as shown in Figure 3-3, plastic zones may occur in different places depending on the thickness of each layer, the compounding interference value, and the properties of the material.

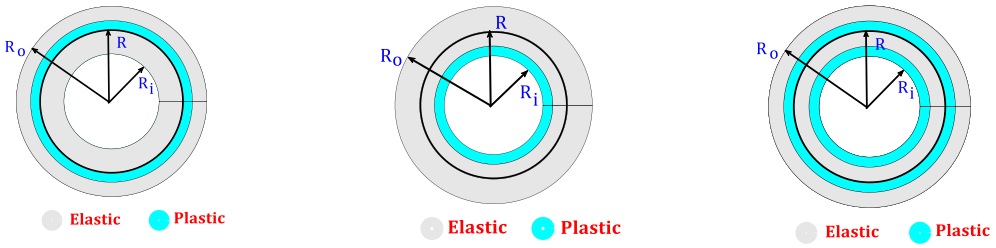

a) b) c)

Figure 3-3. Elastic and plastic zone configurations: a) elastic-plastic-elastic configuration; b) plastic-elastic configuration; and c) plastic-elastic-plastic-elastic configuration.

In Figure 3-3, the configuration (a) occurs if and only if the generated shrink-fit pressure (p_s) is greater than the critical pressure required to start yielding at the inner surface of the outer layer $(\overline{p_\iota})$ and less than the critical pressure required to start yielding at the inner surface of the inner layer $(\overline{p_o})$, $(\overline{p_\iota} < p_s < \overline{p_o})$. Similarly, configuration (b) occurs if the pressure generated by the shrinking process is greater than $\overline{p_o}$ and less than $\overline{p_\iota}$, $(\overline{p_o} < p_s < \overline{p_\iota})$. Finally, configuration (c) takes place if the interface pressure is greater than $\overline{p_\iota}$ and $\overline{p_o}$.

For the outer layer, the yielding begins when the equivalent stress due to the applied interface pressure (caused by the shrink-fit process) at its inner surface $(r = R)$ is equal to the yield strength of the material $(\sigma_{eq} = \sigma_Y)$. It is worth noting that the Lame´ Eqs. (3-7) and (3-8) are valid until the initial yielding occurs. Therefore, the pressure required to initiate yielding can be obtained using Eqs. (3-5), (3-7) and (3-8) as:

$$\overline{p_\iota} = \frac{1}{\sqrt{3}}\sigma_Y\left(1 - \frac{R^2}{R_o^2}\right) \tag{3-13}$$

When the pressure due to the shrink-fit process is greater than $\overline{p_\iota}$, the plastic zone develops at the at bore area of the outer layer, in which the radial stress can be obtained as a function of σ_{eq} using Eqs. (3-3) and (3-5) as:

$$\sigma_r = \int \frac{2}{\sqrt{3}}\frac{\sigma_{eq}}{r}dr + D_1 \tag{3-14}$$

Substituting σ_{eq} from Eq. (3-10) into Eq. (3-14) and then conducting integration yields the radial stress in the plastic zone, which can then be explicitly described as:

$$\sigma_r = \frac{2}{\sqrt{3}} \frac{\sigma_Y}{(1 + AE_P)} \int \left(\frac{1}{r} + AE_P \frac{R_c^2}{r^3} \right) dr + D_1$$

$$\sigma_r = \frac{2}{\sqrt{3}} \frac{\sigma_Y}{(1 + AE_P)} \left(\ln(r) - 0.5AE_P \frac{R_c^2}{r^2} \right) + D_1 \qquad \text{(3-14-a)}$$

It is worth mentioning that the integration constant D_1 in Eq. (14-a) is determined by considering that at the radius R_c (the radius between the elastic and plastic zones), the equivalent stress is equal to the yield strength of the material $(\sigma_{eq} = \sigma_Y)$, and the elastic Lame′ Eqs. (3-7) and (3-8) are valid. Consequently, substituting Eqs. (3-7) and (3-8) into the von-Mises Eq. (3-5) obtains the pressure p_c corresponding to the radius R_c:

$$p_c = \frac{1}{\sqrt{3}} \sigma_Y \left(1 - \frac{R_c^2}{R_i^2} \right)$$

Now, the constant D_1 is directly obtained from Eq. (a) at $r = R_c$ and $\sigma_r = -p_c$. Therefore, the radial stress in the plastic zone can be described as:

$$\sigma_r = \frac{2}{\sqrt{3}} \frac{\sigma_Y}{(1 + AE_P)} \left(\ln\left(\frac{r}{R_c} \right) + 0.5AE_P \left(1 - \frac{R_c^2}{r^2} \right) \right) \qquad \text{(3-15)}$$

It is noted that the hoop stress in the generated plastic zone can be subsequently obtained using Eqs. (3-5), (3-10), and (3-15).

Similarly, for the inner layer, yielding begins when the equivalent stress due to the applied outer pressure induced by the shrink-fit process at its outer surface ($r = R$) is equal to the yield strength of the material $(\sigma_{eq} = \sigma_Y)$. The pressure required to initiate yielding can be obtained using Eqs. (3-5), (3-7) and (3-8) as:

$$\overline{p_o} = \frac{1}{\sqrt{3}} \sigma_Y \left(1 - \frac{R_i^2}{R^2} \right) \qquad \text{(3-16)}$$

As the applied outer pressure generates compressive hoop stress, therefore, the equivalent stress as a function of plastic strain, considering linear work hardening material, may be written as:

$$\sigma_{eq} = -\sigma_Y - E_P \varepsilon_{eq}^p \tag{3-17}$$

The equivalent stress distribution and subsequently the radial stress in the plastic zone can be expressed as:

$$\sigma_{eq} = -\frac{\sigma_Y}{(1 + AE_P)}\left(1 + AE_P \frac{R_c^2}{r^2}\right) \tag{3-18}$$

$$\sigma_r = -\frac{2}{\sqrt{3}}\frac{\sigma_Y}{(1 + AE_P)}\left(\ln\left(\frac{r}{R_i}\right) - 0.5AE_P\left(\frac{R_c^2}{r^2} - \frac{R_c^2}{R_i^2}\right)\right) \tag{3-19}$$

The hoop stress in the generated plastic zone can be subsequently obtained using Eqs. (3-5), (3-18), and (3-19).

In order to better realize the effect of the interference clearance on the distribution of the radial and hoop stress components, let us consider a two-layer thick-walled cylinder with an inner of 50 mm, an interference radius between the two layers of 80 mm, and an outer radius of 150 mm. Both layers are made of steel, with material properties as follows: $\sigma_Y = 700$ MPa, $E = 207$ GPa, $E_t = 50$ GPa, and $\nu = 0.3$. The values of shrink fit interference are, respectively, considered to be 0.39 mm, 0.46 mm, and 0.6 mm.

According to Eqs. (3-13) and (3-16), the outer layer and the inner layer require 289 MPa and 246 MPa, respectively, to initiate yielding. Therefore, until a compounding pressure of 246 MPa, the two layers exhibit purely elastic behavior, which corresponds to a shrink-fit interference of 0.39 mm, according to Eq. (3-12). Thus, Eq. (3-12) is not valid for a shrink-fit clearance beyond 0.39 mm. In this case, a simple iteration is required to calculate the generated shrinking pressure, which is only correlated with a unique shrink-fit clearance value. It involves accumulating the interface pressure. At each step, the new interface pressure value compresses the inner layer by a displacement of u_i and expands the outer tube by a displacement of u_o. It is important to note that the inner and outer displacements are calculated using Eq. (B.3) for plastic behaviour or Eqs. (3-1) and (3-2) for elastic behavior. Finally, the shrink-fit interference corresponding to the iterated interface pressure is equal to $(u_o - u_i)$. It is noted that for the data in this example, the inner layer

begins to yield at a shrink-fit interference of 0.39 mm, while the outer layer begins to yield at a shrink-fit interference of 0.46 mm.

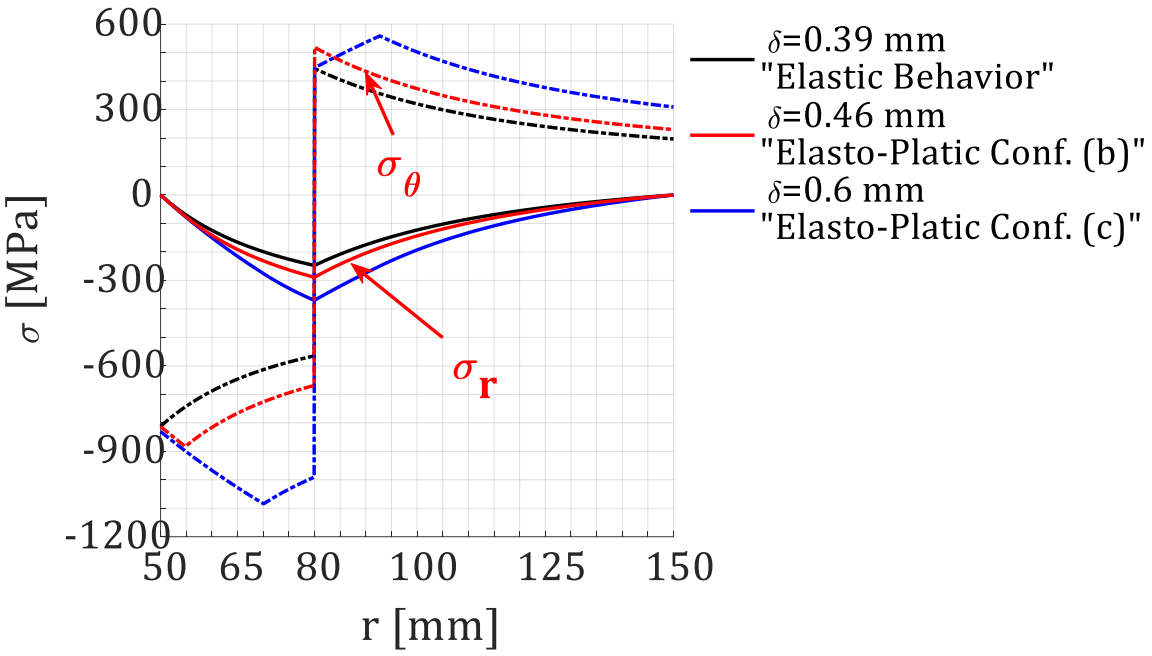

Figure 3-4. Radial and hoop stress variation through the two-layer shrink-fit thick-walled cylinder for different radial interference values.

Figure 3-4 shows the profile of the radial and hoop stresses through the thickness of the compound thick-walled cylinder for different shrink-fit interferences. As it can be reazlied, for an interference of 0.39 mm, corresponding to an interference pressure of 246 MPa, the behaviour of the inner and outer layers is purely elastic. While, for an interference of 0.46 mm corresponding to a pressure of 289 MPa, the yielding occurs at the inner layer while the outer layer behaviour is still purely elastic. Finally, for 0.6 mm of interference, yielding occurs in the outer layer as well. In that case, the generated interface pressure exceeds the critical pressure required to initiate yielding for the inner and outer layers, which is equal to 246 MPa and 289 MPa, respectively.

It is important to note that as the compounding interference between the two layers increases, the compressive stress near the inner region increases. Also, the determinal tensile stress at the outer surface increases with the increasing compounding interference, which negatively affects the lifetime of the thick-walled cylinders, especially for structures exposed to outer surface fatigue.

Thus, in summary, the material behaviour can be purely elastic for both tubes, elasto-plastic for one tube, or elasto-plastic for both of them, and the developed model is able to detect these three distinct behaviors of the material caused by the shrink-fit process.

3.3.2 Modelling of the Wire-winding Process

Wire-winding is a process used for reinforcing thick-walled cylinders and involves hoop wrapping the outer surface of the cylinder with a flat wire made of high-strength steel, as shown in Figure 3-5. The wrapping process generates a compressive pressure acting on the outer surface of the cylinder, which subsequently generates a beneficial compressive stress near the cylinder bore and therefore increases the load bearing capacity of the pressure vessels.

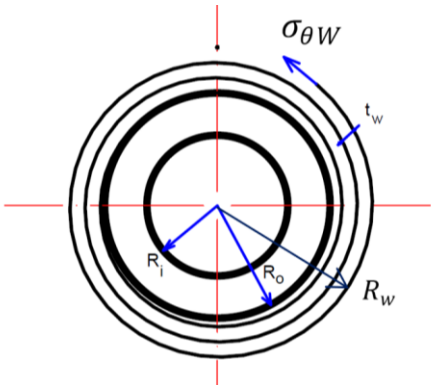

Figure 3-5. Schematic drawing of the wire-winding process

The wrapping is carried layer by layer, and each layer is considered a thin-walled cylinder with a constant hoop stress of $\sigma_{\theta W}$ and thickness of (t_w). Consequently, the developed pressure at the outer surface of the thick-walled cylinder due to each winding layer p_W can be simply represented as [4]:

$$p_W = \frac{t_w \ \sigma_{\theta W}}{R_w - t_w} \tag{3-20}$$

where R_w is the outer radius of the wounded layer as shown in Figure 3-5. The overall internal stresses are thus obtained by summing the internal stresses for all layers.

To better realize the wrapping effect, let us consider a thick-walled cylinder with a wall ratio of 2 that is wound by 2 layers of wire. Each layer has a $0.2R_o$ thickness, and the tension in the wire produces a hoop stress of $0.5\sigma_Y$. Figure 3-6 shows the internal stress distribution through the thickness of the thick-walled cylinder due to the winding process. The results are presented in non-

dimensional forms of radius r^* and stress σ^*, where $r^* = \mathrm{r}/R_i$ and $\sigma^* = \sigma/\sigma_Y$. It is clear that adding two layers substantially increases the induced compressive residual stress near the bore area. While adding layers will increase the beneficial compressive stress in the near bore area, it also noticeably increases the weight and cost of the cylinder.

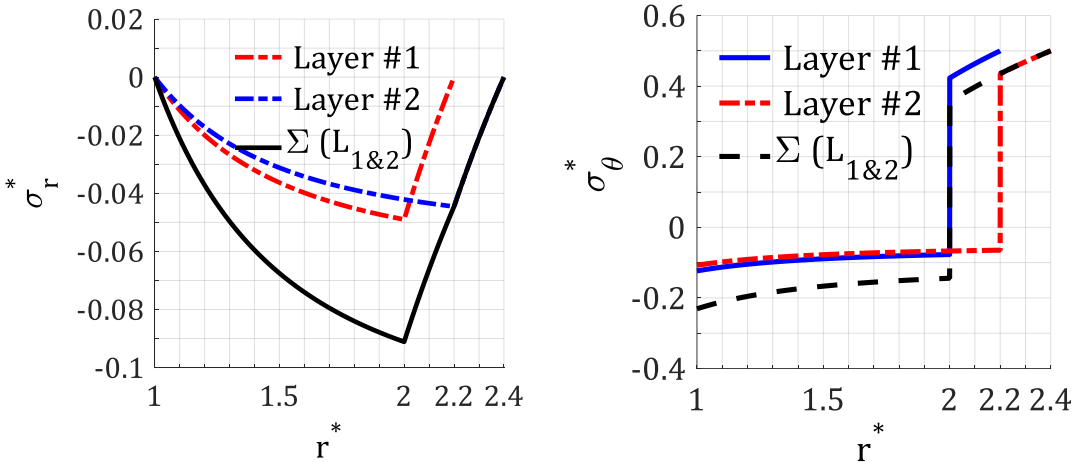

(a) radial stress *(b) hoop stress*

Figure 3-6. Internal stress distributions through the thickness of a thick-walled cylinder due to two wounded layers

3.3.3 Modelling of the Autofrettage Process

The autofrettage process can be categorized as inner autofrettage and outer autofrettage processes. For the inner autofrettage process, the thick-walled cylinder bore is overloaded, which causes permanent deformation in the inner bore area of the thick-walled cylinder. After removing the loads, the inner part of the cylinder is subjected to compression due to the elastic recovery of the outer part of the thick-walled cylinder, thus generating beneficial compressive residual stress near the bore area. On the other hand, in the outer autofrettage, the outer surface of the thick-walled cylinder is overloaded to reduce the tensile stresses at the outer surface of the cylinder.

a) Modelling of the Inner Autofrettage Process

The inner autofrettage process, also called conventional autofrettage, is performed in two stages, namely the loading stage and the unloading stage, as shown in Figure 3-7 (a).

In the loading stage, the inner surface of the cylinder is overloaded beyond its elastic limit, which causes plastic deformation near the cylinder bore area. Knowing the applied inner pressure p_i, the radius R_c (interface between elastic and plastic regions) is directly calculated using Eq. (3-

15) by equating r with R_i and σ_r with $-p_i$. Then the stress profile at the loading stage is calculated using Eqs. (3-5), (3-10), and (3-15).

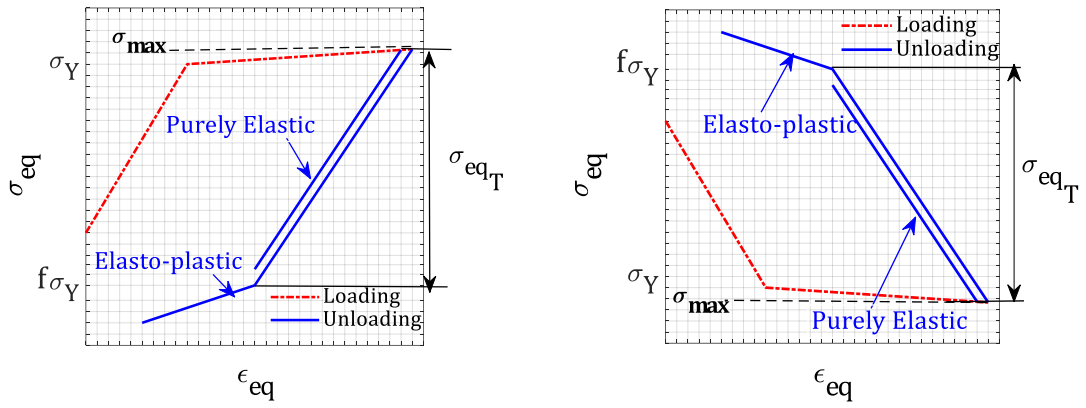

(a) Inner-Autofrettage *(b) Outer-Autofrettage*

Figure 3-7. Material stress–strain behaviour during loading and unloading for the inner and outer autofrettage processes.

In the unloading stage, the applied pressure is released, under which the material may have purely elastic or elastoplastic behavior. If the released pressure exceeds the critical pressure, calculated from Eq. (3-13), the re-yielding of the material near the bore area occurs; therefore, the elastoplastic material behaviour is considered. It is worth mentioning that the new yield strength $(\sigma_{max} + f\sigma_Y)$, in this case, is equal to the total elastic recovery σ_{eq_T}, as shown in Figure 3-7 (a). where, f and σ_{max} are the Bauschinger constant and the maximum equivalent stress, respectively. Considering the new elastic recovery stress σ_{eq_T}, if the released pressure is less than the critical pressure, then the unloading stage is purely elastic, and the Lame´ Eqs. (3-7) and (3-8) are used to estimate the stress profile at the unloading stage. On the other hand, Eqs. (3-5), (3-10), and (3-15) are used if the unloading is elastoplastic. Finally, the hoop residual stress profile is estimated by adding the tensile hoop stress profile due to the loading stage to the compressive hoop stress profile due to the unloading stage.

b) Modelling of the Outer Autofrettage Process

The outer autofrettage, similar to the inner autofrettage, is performed in two stages, as shown in Figure 3-7 (b), but unlike the inner autofrettage, the outer surface of the thick-walled cylinder is overloaded.

In the loading stage, the applied compressive load put the cylinder under compression, as shown in Figure 3-7 (b). The applied loads cause plastic deformation near the cylinder bore area. Similar to the inner autofrettage, the radius R_c is calculated first, but this time using Eq. (3-19) by equating r with R_o and σ_r with $-p_o$. Then the stress profile at the loading stage is calculated using Eqs. (3-5), (3-18), and (3-19).

Similar to the inner autofrettage process, the unloading stage may be purely elastic or elastoplastic depending on whether the released pressure exceeds the critical pressure or not, which is calculated from Eq. (3-16). Also, the new yield strength $(\sigma_{max} + f\sigma_Y)$, in this case, is equal to the total elastic recovery σ_{eq_T}, as shown in Figure 3-7 (b). The yield strength (σ_Y), in this case, is equal to the total elastic recovery σ_{eq_T}, as shown in Figure 3-7 (b). The Lame´ Eqs. (3-7) and (3-8) are used to estimate the stress profile at the unloading stage for purely elastic behavior. On the other hand, Eqs. (3-5), (3-10), and (3-15) are used in the case of elastoplastic behavior. Finally, the hoop residual stress profile is estimated by adding the compressive hoop stress profile due to the loading stage to the tensile hoop stress profile due to the unloading stage.

3.3.4 Modelling Combination of Wire-winding, Autofrettage, and Shrink-Fit

In this study, using analytical equations formulated in previous sections, every possible combination of wire-winding, inner and outer autofrettage, and shrink-fit processes applied to thick-walled cylinders has been analytically investigated to evaluate the induced residual stress profiles.

The analytical solution is initially validated with available results in the literature for a compound cylinder made of two shrink-fitted layers in which, before compounding of the two layers by a shrink-fit pressure of 20 MPa, the inner layer is subjected to the inner autofrettage process while the outer layer is subjected to the outer autofrettage process [56]. The inner and outer layer cylinders are made of A723 steel with material properties of $E = 286 \quad GPa, \nu = 0.29$, and $\sigma_Y = 1170\ MPa$, as reported in [56]. The inner layer has inner and outer radii of 50 mm and 100 mm, respectively, while the outer layer has inner and outer radii of 100 mm and 120 mm, respectively. It is worth mentioning that the material exhibits elastic-perfect-plastic behaviour during loading, while the linear strain hardening and Bauschinger effect are considered during the

unloading stage, as shown in Figure 3-8. The Bauschinger effect constant (f) and strain hardening constant (m) are set at 0.342 and 0.3, respectively.

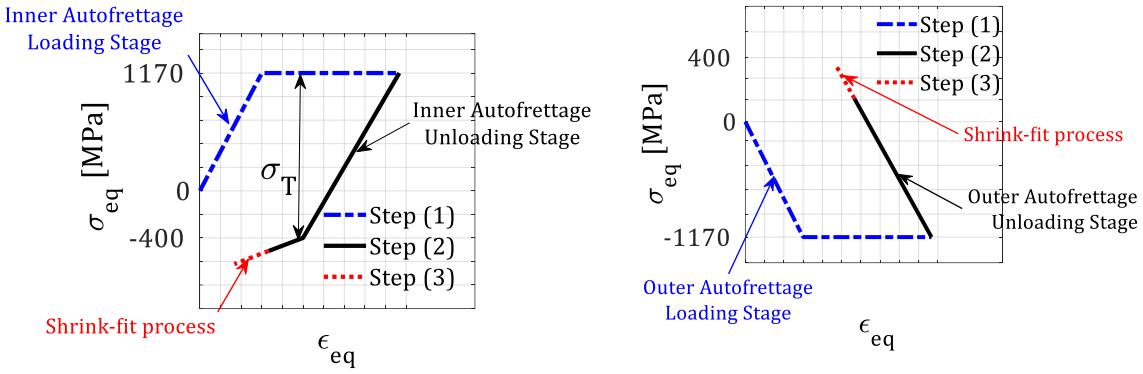

(a) Inner tube *(b) Outer tube*

Figure 3-8. Material stress–strain curve of the inner and outer tubes

The solution follows the same manufacturing procedure sequences. Consequently, the solution is performed as follows:

1) First, the inner tube is subjected to the inner autofrettage process; independently, the outer tube is subjected to the outer autofrettage process. The two processes are modeled as follows:
   - For the inner tube, the stress profile through the wall thickness due to the inner autofrettage at the loading stage is modeled using Eqs. (3-5), (3-10), and (3-15). Then, considering the new elastic yield strength, the same equations are considered at the unloading stage. The inner autofrettage is represented by steps (1-2) in Figure 3-8 (a).
   - For the outer tube, the stress profile through the wall thickness due to the outer autofrettage at the loading stage is modeled using Eqs. (3-5), (3-18), and (3-19). Then, at the unloading stage, the stress profile is obtained using the Lame´ elastic Eqs. (3-7) and (3-8). The outer autofrettage is represented by steps (1-2) in Figure 3-8 (b).
2) Then, the shrink-fit process is performed. The shrink-fit process, at the same time, generates a compressive pressure at the inner and outer surfaces of the outer and inner layers, respectively. For the inner layer, the generated pressure at the outer surface increases the compressive stress through the tube thickness. Eqs. (3-5), (3-18), and (3-19) are used to obtain the stress profile through the wall thickness considering the new initial compression point. The shrink-fit process effect on the autofrettage inner layer is shown in step (3) in Figure 3-8(a). On the other hand, for the outer layer, the generated pressure at the inner surface increases the tensile stress

through the tube thickness. Eqs. (3-5), (3-10), and (3-15) are used to obtain the stress profile through the wall thickness. Considering the new initial tensile point, the shrink-fit process effect on the outer layer is shown in step (3) in Figure 3-8(b).

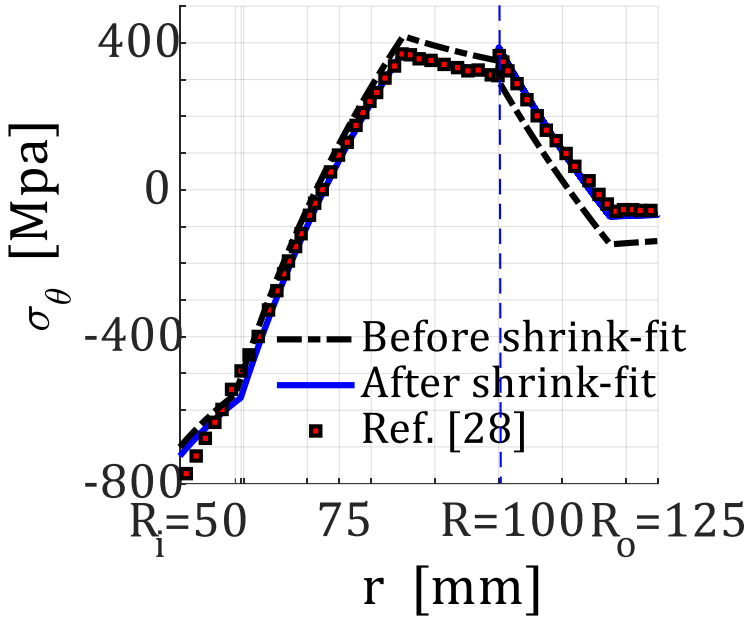

Figure 3-9. Residual hoop stress distributions through the compound thick-walled cylinder wall.

Figure 3-9 shows the hoop stress distribution through the compound thick-walled cylinder wall, before and after shrinking the two tubes with each other. It is noticed that there is good agreement between the proposed solution sequence and the results in Ref. [56]. Comparing the stress profiles before and after shrinking the two tubes, one can conclude that: a) For the inner tube, which has an inner radius of 50 mm and an outer radius of 100 mm, the outer pressure generated from the shrink-fit process is responsible for increasing the compressive stress, as shown in step (3) in Figure 3-8(a), and therefore the re-yielding radius is increased from 58.7 mm to 59.5 mm. b) For the outer tube, with an inner radius of 100 mm and an outer radius of 125 mm, the inner pressure generated from the shrink-fit process increases the tensile stress, as shown in step (3) in Figure 3-8 (b).

In the following, the induced residual stress distribution through the thickness of single- or double-layer thick-walled cylinders is investigated using various combinations of shrink-fit, wire-winding, and autofrettage.

The suggested configurations for one layer are:

- **Configuration #1:** Single inner autofrettage of the thick-walled cylinder
- **Configuration #2:** Inner autofrettage of the thick-walled cylinder after the cylinder is wire wounded.

while the configurations for two layers, as shown in Figure 3-10, are selected as follows:

- **Configuration #3:** Inner autofrettage after shrink fitting the two virgin tubes.
- **Configuration #4:** Inner autofrettage of the inner layer and outer autofrettage of the outer layer. The layers are then compounded through the shrink-fit process.
- **Configuration #5:** Inner autofrettage of the inner layer and outer autofrettage of the outer layer. Then, the two layers are compounded using a shrink-fit process, and finally, the assembly is wire-wounded.

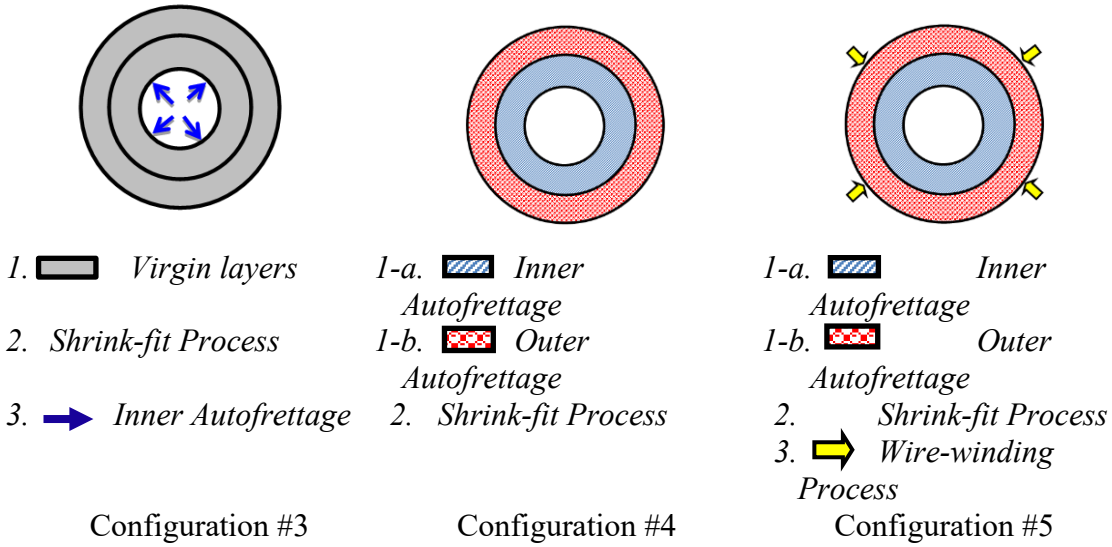

Figure 3-10. Scheme of two-layer configurations and production sequences

It is worth noting that the parameters for single-layer thick-walled cylinder configurations are the inner autofrettage pressure (P_i), the hoop winding stress ($\sigma_{\theta W}$), inner, and outer radii (R_i, R_o). Alternatively, the added parameters for two-layer thick-walled cylinder configurations compared with the single layer one is the intermediate radius (R), the outer autofrettage pressure (P_o), and the compounding shrink-fit pressure (p_s). Table 3-1 lists the parameter values for each configuration.

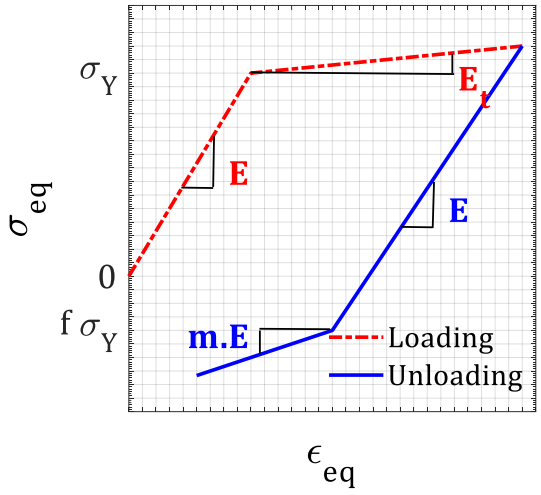

Figure 3-11. Linear-hardening material stress–strain curve

Table 3-1. Design parameters for the five configurations

Parameters / Configuration		R_i [mm]	R_o [mm]	R [mm]	P_i [MPa]	$\sigma_{\theta W}$ [MPa]	P_o [MPa]	P_s [MPa]
Single layer	Conf. 1	60	150	-	827	-	-	-
	Conf. 2				918	420		
Two layers	Conf. 3			120	625	-	-	40
	Conf. 4					-	209	
	Conf. 5					420		

Figure 3-12 depicts the developed residual hoop stress distribution through the wall thickness for the five different configurations. Results show that while the single layer configurations produce more compressive stress near the bore of the cylinder compared with the two-layer configurations, the two-layer configurations produce less tensile stress at the outer surface of the cylinder compared with the single layer configurations.

For the single-layer tube, configuration #2 significantly enhances the compressive residual stress, particularly at the inner bore area, compared with configuration #1. Similarly, for the two-layer tube, configuration #5 provides the maximum compressive and minimum tensile residual stresses at the inner and outer surfaces, respectively, compared with configurations #4 and #3. Also, it is interesting to note that the compressive residual stress profile is the same for configurations #3 and #4 through the thickness of the inner layer. On the other hand, the residual

tensile stress profile through the outer layer wall is different, and in the overall evaluation, configuration #4 outperforms configuration #3.

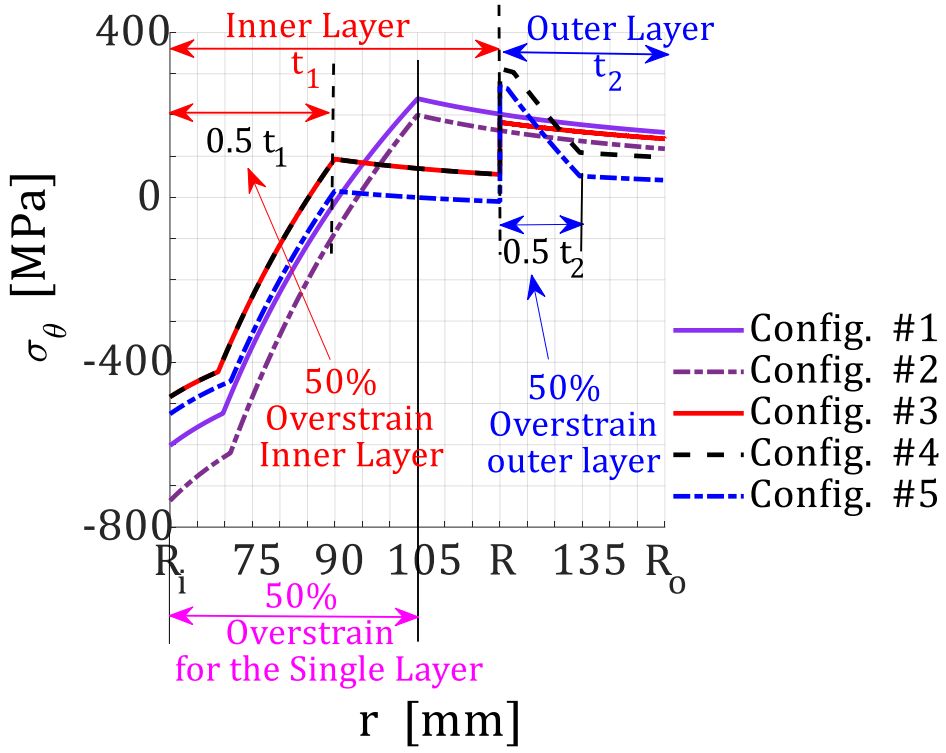

Figure 3-12. Residual hoop stress profiles for different configurations through the wall thickness

Configurations #2 and #5 clearly reveal the positive effect of the wire-winding process on the residual stress distribution through the wall thickness of a single or two-layer thick-walled cylinder. For single layer, in configuration #2, compared with configuration #1, the winding process puts the cylinder under compression before the inner autofrettage. Therefore, during the loading stage of inner autofrettage, the elastic zone is larger than in a virgin cylinder. This increases, in this example, the applied autofrettage pressure from 827 MPa (in configuration #1) to 918 MPa to get the desired 50% overstrain in both cases, as stated in Table 3-1.

Also, the benefit of the wire-winding process is clearly shown in two-layer configuration #5 compared with configurations #3 and #4. Unlike configuration #2, the winding process is performed as a final process in configuration #5. Therefore, for the inner tube with radii of 60 mm and 120 mm, the winding process continues compressing the tube after the inner autofrettage and shrink-fit processes; its effect is similar to the effect of the shrink-fit process in step (3) in Figure

3-8(a). This makes the re-yielding radius increase from 68.8 mm to 71.1 mm. On the other hand, the outer layer is under tension after the outer autofrettage and shrink-fit processes. Therefore, the winding process lowers the tensile stress, as shown in Figure 3-12. Finally, by comparing the residual stress profiles through the wall thickness from the inner radius to a radial position of 90 mm, it becomes clear that the residual stress profile highly depends on the order in which the manufacturing processes are conducted.

3.4 Summary And Conclusions

In this study, first an analytical solution for the residual stress profile through the wall thickness has been presented for each of the reinforcing processes used in thick-walled cylinder design, namely wire-winding, shrink-fit, inner autofrettage, and outer autofrettage. Using the same manufacturing sequences, the analytical formulations have been combined to predict the residual stress distribution for various combinations of the aforementioned processes, resulting in an accurate estimation of the induced residual stresses through the thickness of reinforced thick-walled cylinders using a combination of shrink-fit, autofrettage, and wire winding processes. The wire-winding process significantly improves the residual stress profile through the wall thickness of a single or two-layer thick-walled cylinder. The analytical models can clearly detect the different behaviour of the material due to the shrink-fit process, as it can be purely elastic for both tubes, elasto-plastic for one tube, or elasto-plastic for both of them. The residual stress distribution through the wall thickness for different combinations of reinforcing processes depends on the order in which they are conducted during the manufacturing process. In summary, the proposed analytical methodology can provide essential guidance for the design of single and multi-layer compound cylinders reinforced by wire-winding, shrink-fit, and inner and outer autofrettage processes.

CHAPTER 4

DESIGN OPTIMIZATION OF COMPOUND THICK-WALLED CYLINDERS TREATED WITH AUTOFRETTAGE, SHRINK-FIT AND WIRE-WINDING PROCESSES USING NEURAL NETWORK REGRESSION

Authors: Mohamed Elfar, Ramin Sedaghati, and Ossama R. Abdelsalam [133].
Status before thesis submission: Submitted to: ASME-Journal of Pressure Vessel Technology. Initially submitted on: 1st August 2023. / (Under Review).

Abstract

Shrink-fit, wire-winding, and autofrettage processes are commonly utilized to enhance strength and durability of thick-walled cylinders across various mechanical applications. In this study, a novel design optimization methodology has been developed to determine the optimal configuration of a thick-walled cylinder, incorporating different combinations of shrink-fit, wire-winding, and autofrettage techniques. The objective is to identify the optimal layer thickness, shrink-fit interference, inner autofrettage pressure, and outer autofrettage pressure, if applicable, to maximize the compressive residual stress and minimize the tensile residual stress, thereby extending fatigue lifetime of the cylinder. First, different configurations of thick-walled cylinders, subjected to various combinations of reinforcement processes, are identified. A dataset of residual hoop stress profiles through the cylinder thickness is subsequently generated for these configurations based on the same manufacturing process. Neural network regression is then utilized to construct a single fitting function for the residual hoop stress profiles. To achieve a strong agreement between the generated neural network fitting function and the dataset, a parametric study is performed to determine the optimal training functions, activation functions, and hyperparameters. A combination of GA and SQP algorithms is employed to determine the accurate optimal values. Fatigue life analysis is subsequently conducted to estimate the fatigue lifetime of the optimal configuration. Results demonstrate that the optimal configuration, involving inner autofrettage of the inner layer followed by shrink-fitting with a virgin layer, and wire-winding the entire assembly, can significantly improve fatigue life compared with virgin monobloc cylinder.

4.1 Introduction

Thick-walled cylinders are essential components utilized in a wide range of industrial structures, enabling the safe storage and transportation of fluids under mechanical, thermal, and severe thermo-mechanical loading conditions. To enhance their performance, several reinforcement processes, such as wire-winding, shrink-fit, and autofrettage, are utilized to induce the beneficial residual compressive tangential (hoop) stress near the bore area [2, 12, 13, 26, 29, 58, and 128]. The introduction of the compressive residual stress near the bore mitigates the overall level of tensile stress during loading conditions, directly impacting fatigue life, durability, and load bearing capacities.

Despite their advantages, each reinforcement process has its limitations [89]. The wire-winding and shrink-fit methods exhibit limited compressive stresses near the bore region compared to the autofrettage process. Additionally, in the shrink-fit method, the internal stress profile undergoes a large transition from compressive to tensile stress at the interface radius, resulting in high tensile stress at the outer surface of the outer layer. Also, the effectiveness of the compressive stress induced by the autofrettage process is negatively affected by the Bauschinger effect, reducing its effectiveness [59, 60]. To address these limitations and improve the distribution of compressive residual stresses across the cylinder's thickness, researchers have proposed different configurations of thick-walled cylinders that subjected to various combinations of the reinforcement processes [4, 56, 66, 72, and 73]. These processes aim to enhance the reliability and longevity of these cylinders in demanding industrial applications.

While the majority of the previous studies have focused on investigating the distribution of residual stress across the wall thickness of thick-walled cylinders under different reinforcement process combinations, limited research study has been dedicated to identifying the optimal configuration of thick-walled cylinders to enhance their mechanical performance [75– 77]. These studies introduced different configurations of multi-layer, thick-walled cylinders subjected to different combinations of shrink-fit and autofrettage processes with the aim of improving their fatigue life. Notably, the distinguishing factor among these studies lies in the optimization techniques employed. Jahed [75] utilized the simplex optimization search technique to determine the optimal values of design parameters for each proposed thick-walled cylinder configuration, with the objective of maximizing the compressive residual stress in each combination. In contrast,

Kumar et al. [76] employed a genetic algorithm technique to achieve the same objective, maximizing the compressive residual stress for each proposed thick-walled cylinder configuration as in the previous study. Furthermore, Ossama et al. [77] engaged in a similar line of research to Kumar [76] but incorporated both the genetic algorithm and sequential quadratic programming (SQP) to accurately determine the optimal values of design variables for each thick-walled configuration, aiming to maximize the compressive residual stress and minimize the tensile stress at the outer surface as well.

Undoubtedly, achieving the optimum compound thick-walled cylinder configuration is crucial for maximizing their performance and durability through enhancing the compressive residual hoop stress near the bore area or/and reducing the tensile hoop stress near the outer surface. One of the challenges in addressing these problems lies in the derivation of the objective function. In previous few studies, first, different compound thick-walled cylinder configurations have been proposed, and for each configuration, the objective function is then derived to obtain the optimal values of the design parameters. Subsequently, a comparison of the optimum solutions for each configuration is performed to determine the most favourable configuration. Notably, the objective function in these studies represents the compressive residual hoop stress value at the inner surface or the tensile residual hoop stress value at the outer surface.

In this study, a novel approach based on neural network regression has been developed to establish a unique objective function for various configurations of compound thick-walled cylinders. The objective function is considered to be the area under the residual hoop stress profile through the wall thickness. Consequently, the objective function is represented by the continuous residual hoop stress profile, in contrast to the previous studies where only one value of the residual stress at the inner surface or at the outer surface of the compound thick-walled cylinders is considered.

Different configurations of thick-walled cylinders subjected to various combinations of autofrettage, wire-winding, and shrink-fit processes are first identified, thereby defining the design variables for each configuration. Subsequently, the design variables and their domain space are established to cover the entire design space. To comprehensively explore the design space, the full-factorial approach is selected to construct the design of experiments table.

Following that, the residual hoop stress profiles throughout the wall thickness are calculated using the same manufacturing sequence, as outlined in prior research [126], thus generating labeled input and output data sets. These data sets consist of the values of the design variables and their corresponding calculated residual hoop stress profiles. Then, the data sets are utilized in neural network regression to derive a fitting function for all the residual hoop stress profiles. To achieve the closest possible match with the actual profiles, a fine-tuning of the neural network parameters, including the training function, error function, and hyperparameters (such as learning rate, momentum, number of layers, and number of neurons per layer), is performed to obtain the optimal neural network parameters.

Subsequently, the genetic algorithm (GA) and sequential quadratic programming (SQP) techniques are used to determine the global optimum values for the design variables. This process facilitates the identification of the optimal configuration for the compound thick-walled cylinder. Finally, the fatigue life of the obtained optimum configuration is evaluated by subjecting it to cyclic mechanical loading conditions. Subsequently, the fatigue life of the optimum configuration is compared with that of a virgin single-layer thick-walled cylinder with identical inner and outer radii, and under the same loading conditions.

4.2 Design Optimization Methodology

The objective of this study is to improve the mechanical performance of thick-walled cylinders, including their durability, lifetime, load-bearing capacity, and weight. This is possible by increasing the compressive residual hoop stress close to the bore area while decreasing the tensile residual hoop stress near the outer section of the compound cylinder. Thus, as shown in Figure 4-**1**, the design optimization goal is to maximize the negative area of the compressive residual stress area as well as minimizing the positive area of the tensile residual stress.

In other words, the design optimization goal is to minimize the net area under the residual hoop stress profile through the wall thickness, considering the sign of the residual hoop stress. The proposed objective function (Y) can be mathematically represented as:

$$\mathrm{Y} = \int_{R_i}^{R_o} \sigma_\theta dr \tag{4-1}$$

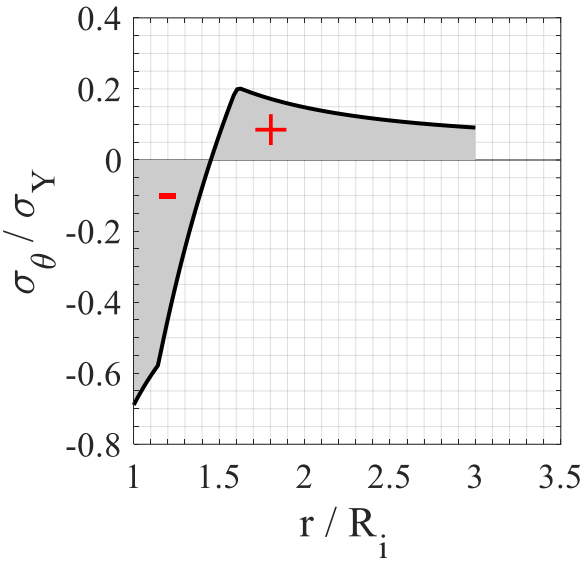

Figure 4-1. Residual hoop stress profile through the wall thickness of a thick-walled cylinder, made of streel with a wall ratio of 3, subjected to a conventional autofrettage process resulting in a 35% overstrain.

To formulate the design optimization problem, it is first important to address the design variables and precisely define the domain space for each design variable. This step is crucial as the design variables are changed for each proposed configuration. The suggested configurations for the single layer (monobloc) and compound double-layer thick-walled cylinders are summarized as follows:

Configurations for the single layer cylinder:

- **Configuration #1:** Inner autofrettage of the thick-walled cylinder.
- **Configuration #2:** Inner autofrettage of the thick-walled cylinder after the cylinder is wire-wound.

Configurations for the double layer cylinder:

- **Configuration #3:** Shrink fitting of two virgin tubes.
- **Configuration #4:** Wire-winding the assembly of Configuration #3.
- **Configuration #5:** Inner autofrettage of the inner layer; then shrink fitting it with a virgin layer.
- **Configuration #6:** Wire-winding the assembly of Configuration #5.

- **Configuration #7:** Inner autofrettage of the inner layer and outer autofrettage of the outer layer. The two layers are then compounded through the shrink-fit process.
- **Configuration #8:** Wire-winding the assembly of Configuration #7.

The inner layer thickness (t_1), if any, the shrink-fit pressure (p_s), the elastoplastic radii (R_{ci} and R_{co}) of the inner and outer layers, respectively, due to the inner and outer autofrettage processes, respectively, and the hoop winding stress ($\sigma_{\theta W}$) are considered to be the design variables. The consideration of elastoplastic radii (R_{ci} and R_{co}) for the inner and outer layers is used instead of relying on the inner and outer autofrettage pressures. The basis behind this consideration is rooted in the iterative nature of the design variables to span the entire space. As the thickness of the layers changes, it may potentially result in scenarios where the applied autofrettage pressure exceeds the complete plastification of the layer or may fail to reach the required threshold for plastic deformation. It is worth noting that after identifying the optimum solution, the inner and outer autofrettage pressures can be simply obtained as a function of inner and outer elastoplastic radii, respectively. Also, for the same reason the shrink-fit pressure (p_s) is considered instead of the shrink-fit clearance (δ).

Table 4-1. Design variables for compound thick-walled cylinder configurations

Parameters / Configuration		t_1	p_s	R_{ci}	R_{co}	$\sigma_{\theta W}$	# Design Variables
Single layer	Conf. 1	Total thickness	-	✓	-	-	1
	Conf. 2					✓	2
Two layers	Conf. 3	✓	✓	-	-	-	2
	Conf. 4			-	-	✓	3
	Conf. 5			✓	-	-	3
	Conf. 6			✓	-	✓	4
	Conf. 7			✓	✓	-	4
	Conf. 8			✓	✓	✓	5

Table 4-1 outlines the selected design variables related to the eight configurations described before. As can be realized, the number of design variables differs for each configuration. The domain space for each design variable, which represents the lower and upper limits of the design variable, is considered as follows: t_1 $[0.4t - 0.7t]$, p_s $[0.05\bar{p}_x - 0.5\bar{p}_x]$, R_{ci} $[0.4t_1 - 0.75t_1]$,

R_{co} $[0.4t_2 - 0.75t_2]$, and $\sigma_{\theta W}$ $[0.25\,\sigma_Y - 0.5\,\sigma_Y]$ in which t is the total thickness of the thick-walled cylinder, t_2 is the outer layer thickness "$t_2 = t - t_1$", σ_Y is the material yield strength, and $\bar{p}_x$ is the critical shrink-fit pressure which is required to initiate plasticisation for the inner or outer layer and it can be described as [126]:

$$\bar{p}_x = min\left\{\bar{p}_{outer} = \frac{1}{\sqrt{3}}\sigma_Y\left(1 - \frac{R^2}{R_o^2}\right)\ ,\qquad \bar{p}_{inner} = \frac{1}{\sqrt{3}}\sigma_Y\left(1 - \frac{R_i^2}{R^2}\right)\right\}$$

Finally, the design constraints for each design variable have been established by defining its upper and lower limits, with the exception of t_1, which is set within the range of $[0.4t - t]$ to accommodate single layer configurations. It is noted that the residual stress distribution through thickness, arising from different combinations of strengthening processes, is influenced by the manufacturing process sequence. Consequently, specific constraints are considered to restrict the selection among the proposed eight configurations. For example, referring to Table 4-1, if R_{ci} is equal to 0, then R_{co} is also set to 0. Similarly, if the ratio of t_1 exceeds $0.7t$, so the iteration proceeds with the single-layer configurations, leading to $t_1$being equal to t, p_s being assigned a value of 0, and R_{co} being set to 0.

4.2.1 Objective-Function Derivation

As shown in Figure 4-1, the objective function is represented by area under the hoop residual stress profile through the wall thickness. As a result, all hoop residual stress profiles covering the entire design space of each configuration are accurately evaluated based on the same manufacturing sequence. Subsequently, with the help of Design of Experiments (DoE) and the machine learning regression models, a single smooth fitting function is derived for all configurations.

a) *Design* of Experiments

The design of experiments (DoE) is a scientific method that is used to improve, develop, and design processes in many fields. It uses tools from applied statistics to change multiple input design variables at the same time to find and measure the cause-and-effect relationships between design variables and results in the process or problem being studied. This can save time and effort by making it easier to find the best settings and conditions for multi-design variable problems. Full factorial, partial factorial, and Taguchi designs are generally used as ways to identify all pertinent

combinations of experimental designs. Unlike the full-factorial designs, the partial factorial and Taguchi designs rely on a small set of design variable combinations to span the design space. In this study, the full factorial method is selected to obtain the maximum number of design variable combinations for each configuration that spans the entire design space to enhance the generated fitting function. This is achieved by carefully selecting an independent number of center points for each design variable in each configuration, which is optimized to ensure a comprehensive exploration of the design space. For example, in Configuration #1, which includes a single design variable (R_{ci}), as stated in Table 4-1, 800 equal space points are chosen within the lower and upper limits of R_{ci}, resulting in a total of 800 design variable combinations. Similarly, for Configurations #2 and #3, where each configuration has two design variables, 41 equal space points are selected for each variable, thereby generating 1680 design variable combinations for each configuration. Moreover, in configurations #4 and #5, where each configuration includes three design variables, 16 equal space points for each variable are selected, leading to 4095 design variable combinations for each configuration. Additionally, for configurations #6 and #7, which encompass four design variables, 10 equal space points are chosen for each variable, resulting in an extensive set of 10,000 design variable combinations for each configuration. Lastly, Configuration #8, with five design variables, requires a selection of 7 equal space points for each variable to generate a total of 16,806 design variable combinations.

Table 4-2. Number of center points for each design variable in each configuration

Configuration	#1	#2	#3	#4	#5	#6	#7	#8
# Center Points	800	41	41	16	16	10	10	7

The selected number of points for each design variable in eight configurations are provided in Table 4-2, alongside the corresponding number of design variable combinations for each configuration are presented in Table 4-3.

Table 4-3. Number of design variables combinations for each configuration

Configuration	#1	#2	#3	#4	#5	#6	#7	#8
# Combinations	800	1680	1680	4095	4095	10000	10000	16806

Finally, the hoop residual stress distribution through the thick-walled cylinder thickness is calculated for each design variable combination in each configuration. It is worth noting that the total number of evaluated residual stress profiles is 49156.

b) Machine *Learning*

Machine learning (ML), a branch of artificial intelligence, focuses on developing algorithms that learn from data, identify patterns, and make predictions without explicit programming. Regression, a crucial field within machine learning, focuses on modelling and analyzing relationships between dependent and independent variables. There are various types of regression models in machine learning, including linear regression, polynomial regression, logistic regression and neural network regression. The selection of an appropriate regression model depends on the nature of the data and the research objectives, as each model has its own advantages and disadvantages. Neural network regression, a widely used approach in ML regression, employs interconnected layers of neurons to model complex input-output relationships. It utilizes nonlinear activation functions and mathematical transformations to capture complex patterns within the data.

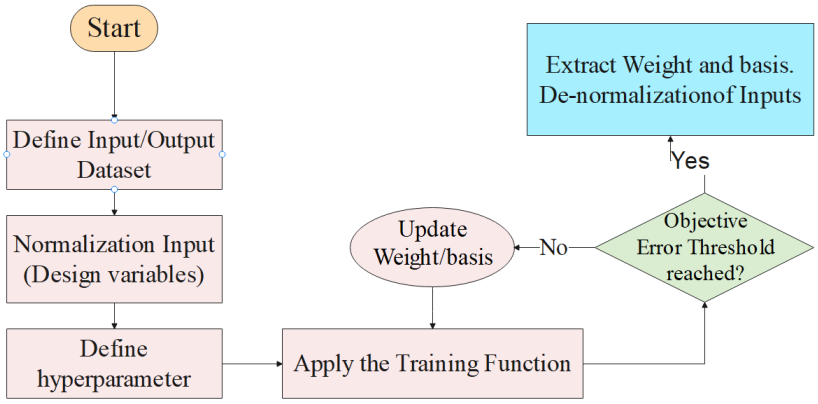

Figure 4-2. Flowchart of the NN prediction

Due to its capability to model complex relationships within input-output data, this study employs the neural network regression model. However, the accuracy of the model depends on adjusting components (or so-called fine-tuning) such as, training function, error function, and hyperparameters (e.g., learning rate, momentum, number of layers, and neurons per layer) to optimize the accuracy. It is worth noting that the training function determines how the network's weights and biases are updated during training in order to minimize the objective function (error function). The following is considered for the establishment of the model using artificial neural network regression approach:

1. Hidden layer sizes: The number of neurons in each hidden layer varies between 10-100 while the number of hidden layers varies between 1-3.

2. Learning rates: learning rates varies between 0.0001 and 0.01.
3. Activation functions: The activation functions 'logsig', 'tansig', and ‘poslin’.
4. Objective functions: The error functions mean squared error (MSE) and mean absolute error (MAE) are utilized.
5. Training functions: Two training functions, gradient descent 'traingd' and gradient descent-conjugate gradient methods 'trainscg', are selected.

The detailed flowchart of the neural network (NN) prediction is shown in Figure 4-2. It is noteworthy to mention that the dataset in ANN is divided into training, testing, and validation subsets which their weight, respectively, are considered to be 70%, 20%, and 10%. According to the grid search including the previous fine-tuning ranges, the optimal fine-tuning parameters are identified and listed in Table 4-4 while Figure 4-**3** depicts the architecture of the considered artificial neural network.

Table 4-4. The optimal fine-tuning parameters.

Fine-Tuning Parameter	**Optimal Value**		
Number of Hidden Layers	3		
Hidden Layer Sizes	25	50	25
Activation Functions	f_1(logsig)	f_2(logsig)	f_3(logsig)
Learning Rate	0.001		
Objective Function	MSE		
Training Function	gradient descent-conjugate gradient methods ('trainscg')		

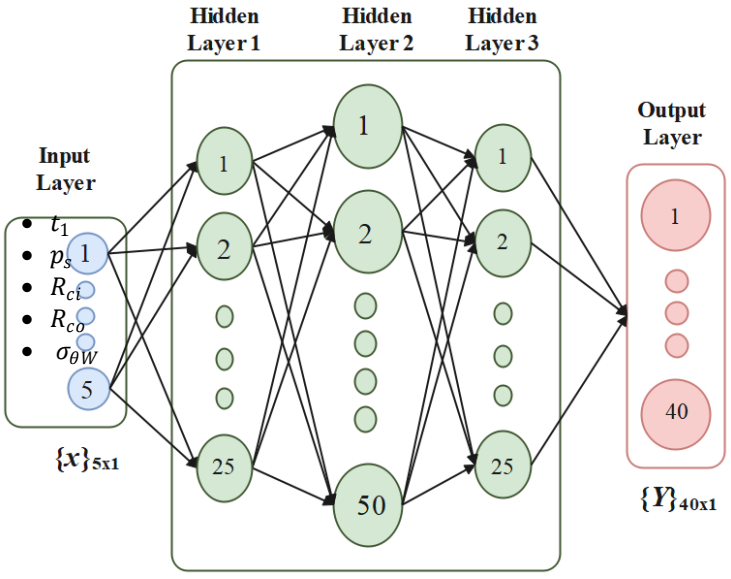

Figure 4-3. Neural network architecture.

It is worth noting that the output equation for a neural network with the optimal values of fine-tuning parameters can be mathematically represented as follows:

$$\{Y\}_{40\times1} = \{\sigma_\theta\}_{40\times1} = \\ = [W_4]_{40\times25} f_3\{[W_3]_{25\times50} f_2([W_2]_{50\times25} f_1\langle[W_1]_{25\times5}\{x\}_{5\times1} \\ + \{b_1\}_{25\times1}\rangle + \{b_2\}_{50\times1}) + \{b_3\}_{25\times1}\} + \{b_4\}_{40\times1} \quad (4\text{-}2)$$

in which Y, $x, W_{1-4}, b_{1-4}, and\ f_{1-3}$ are the output "the hoop residual stress profile", the design variables inputs parameters, the weight matrices associated with the connections between the layers, the bias vectors corresponding to each layer, and the activation functions applied to the outputs of each layer, respectively.

4.2.2 Optimization Strategies

Once the objective function (fitting function) is formulated using NN, the genetic algorithm (GA) is utilized to iteratively evolve a population of potential solutions, aiming to roughly get a point near to the global optimum point. The GA draws inspiration from natural genetics and selection principles, operating on candidate solutions represented as binary strings. Each solution's fitness is evaluated based on its performance, and the GA employs reproduction, crossover, and mutation operators to generate offspring solutions. These operations facilitate exploration and exploitation of the search space, gradually improving the quality of the solutions. The process continues until a specific termination criterion is met.

As GA generally captures solutions near to global optimum, to further enhance the solution and achieve the accurate global optimum, optimum solution obtained from GA is used as the initial point for the Sequential Quadratic Programming (SQP) to capture the global optimum solution accurately. SQP is a local gradient-based optimizer which solves quadratic programming subproblems iteratively by creating quadratic approximations of the objective function and constraint functions.

4.3 Fatigue Life

Thick-walled cylinders are generally subjected to reinforcement processes to improve their fatigue life by inducing compressive residual stresses. To assess their performance under cyclic loading conditions, it is necessary to determine their fatigue life. In this stage, the fatigue life of

the optimized compound cylinder subjected to cyclic inner mechanical or thermomechanical loading conditions is assessed, following ASME's Alternative Rules for Construction of High-Pressure Vessels Code, Division 3 [11], under the assumption of the existence of a semi-elliptical crack.

4.3.1 Fatigue Life Due to Cyclic Mechanical Loading Conditions

To determine the fatigue life, first the initial depth of the semi-elliptical crack, a_{Ec}, is assumed. Subsequently, the stress distribution normal to the crack plane is formulated using a curve fitting approach of third-order polynomial, as function of polynomial constants (A'_{0-3}) and radial distance (r) as:

$$\sigma_\theta = A'_0 + A'_1\left(\frac{r}{t}\right) + A'_2\left(\frac{r}{t}\right)^2 + A'_3\left(\frac{r}{t}\right)^3 \tag{4-3}$$

where t is the thick-walled cylinder thickness. Then the Stress Intensity Factor (K_I) is evaluated as [19]:

$$K_I = [(A_0 + A_p)G_o + A_1G_1 + A_2G_2 + A_3G_3]\sqrt{\frac{\pi a_c}{Q_c}} \tag{4-4}$$

where A_p and A_{0-3} are, respectively, applied internal pressure in MPa, coefficients given as a function of polynomial constants (A'_{0-3}) and the initial depth of the semi-elliptical crack (a_{Ec}) as stated in Eq.(4-5). G_{0-3} and Q_c are, respectively, the free surface correction factors provided in ASME code [11], and the flaw shape parameter as a function of the flaw's major axes (l), the plastic zone correction factor (q_y), and the flaw aspect ratio $\left(\frac{a_{Ec}}{l}\right)$, as described as in Eq. (4-6):

$$A_o = A'_o\,, A_1 = A'_1\left(\frac{a_{Ec}}{t}\right), \qquad A_2 = A'_2(\frac{a_{Ec}}{t})^2\,, \qquad A_3 = A'_3(\frac{a_{Ec}}{t})^3 \tag{4-5}$$

$$Q_c = 1 + 4.593\left(\frac{a_{Ec}}{l}\right)^{1.65} - q_y \tag{4-6}$$

It is noteworthy that the same approach is utilized in calculating stress intensity factors due to residual stresses as well [11]. Subsequently, the rate at which the crack is propagated can be precisely described as a function of the stress intensity ratio (R_K), the range of stress intensity factor (ΔK_I), and crack growth rate factors (C_f and m_f), in accordance with the Paris relation, as:

$$\frac{da_c}{dN} = C_f[f(R_K)](\Delta K_I)^{m_f} \tag{4-7}$$

It is worth noting that the ASME pressure vessel code Division 3 [11] provides the crack growth rate factors, C_f and m_f. The stress intensity ratio (R_K) and the range of stress intensity factor (ΔK_I) are denoted as a function of the stress intensity factors associated with the initial inside pressure (K_{Imin}), working pressure (K_{Imax}), and residual stress (K_{Ires}) and it can be stated as:

$$R_K = \frac{K_{Imin} + K_{Ires}}{K_{Imax} + K_{Ires}} \tag{4-8}$$

$$\Delta K_I = K_{Imax} - K_{Imin} \tag{4-9}$$

In the last stage of the analysis, Eq. (4-7) is numerically integrated to determine the lifetime cycles by considering incremental changes of the crack depth (Δa_c), under the assumption of constant (ΔK_I) during incremental changes in the crack depth (Δa_c). By continuously updating the crack depth increment until the final permissible crack depth is reached, the lifetime cycles are determined as:

$$\Delta N = \frac{\Delta a_c}{C_f[f(R_K).(\Delta K_I)^{m_f}]} \tag{4-10}$$

4.3.2 Fatigue Life Due to Cyclic Thermomechanical Loading Conditions

In the case of thick-walled cylinders under cyclic thermomechanical loading conditions, a significant challenge arises. Unlike cyclic mechanical loading, where the applied stress remains identical across cycles, cyclic thermomechanical loads introduce varying stress levels with each cycle. To address this, a table of the stress intensity factors due to the combination of stresses due to thermomechanical loads and the residual stresses are created among their corresponding mean temperature.

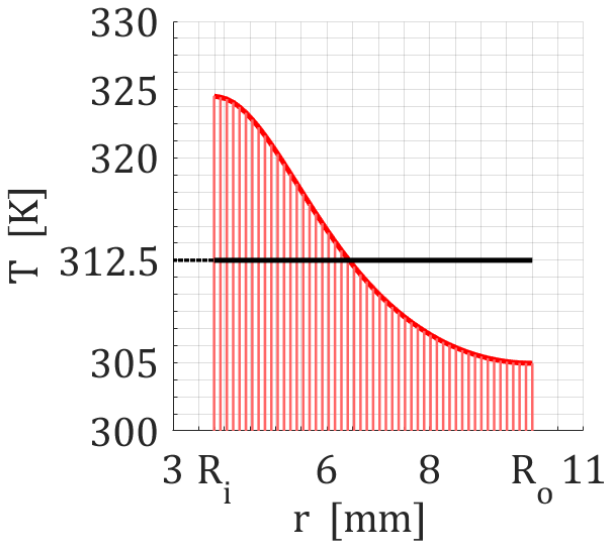

Figure 4-4. The Area under the temperature profile through the cylinder wall after 10 thermomechanical pulses under the loading conditions, geometrical, and material properties, as detailed in Section 2.4.3.

Subsequently, the cumulative fatigue life cycles are determined as the number of cycles until the stress intensity factor approaches the temperature-dependent critical stress intensity factor. It is essential to highlight that Eqs. (4-3) to (4-7) are used to calculate the stress intensity factors that come from the combination of residual stress and stress caused by cyclic thermomechanical loads. Furthermore, the area under the temperature profile through the wall thickness is utilized to obtain the corresponding mean temperature to each calculated stress intensity factor, as shown in Figure 4-4.

4.4 Results and Discussions

In this study, a linear work-hardening material model is employed to approximate the real material behavior. The possible residual stress profiles that span the design space for the eight different configurations discussed in Section 4.2 are generated using a consistent manufacturing process [126]. It is important to note that the thick-walled cylinders are made of NiCrMoV125 steel with material properties of $E = 286 \quad GPa, \nu = 0.29$, and $\sigma_Y = 700\ MPa$. The inner and outer radii of the compound cylinder are kept constant at 50 mm and 150 mm, respectively, for all configurations. The design variables, including the inner layer thickness (if applicable), shrink-fit clearance, elastoplastic radii of the inner and outer layers resulting from the inner and outer autofrettage processes, and hoop winding stress, are bounded as described in Section 4.2.1.

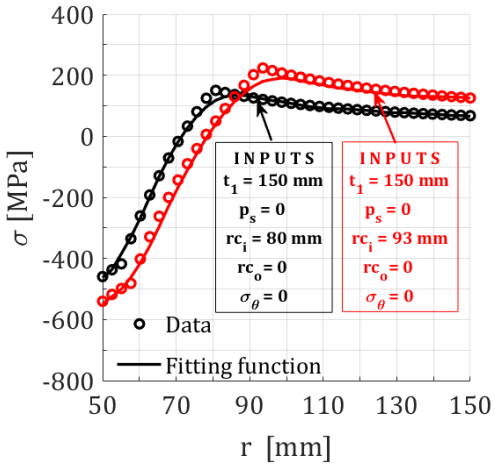

Figure 4-5. Residual hoop stress profile through the wall for the 1st configuration

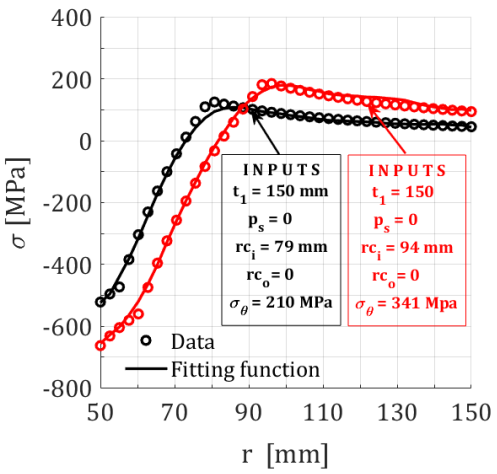

Figure 4-6. Residual hoop stress profile through the wall for the 2nd configuration

As mentioned before, to explore the design space, a full factorial approach is utilized to obtain various combinations of design variable for the eight configurations. The NN with the architecture shown in Figure 4-3 and the settings outlined in Table 4-4 is employed to derive a single fitting function equation for all residual stress profiles (49162 profiles), which has the same format of Eq.(4-2). The specific constant values of the weight matrices associated with the connections between the layers and the bias vectors corresponding to each layer for this example can be found in Appendix C.

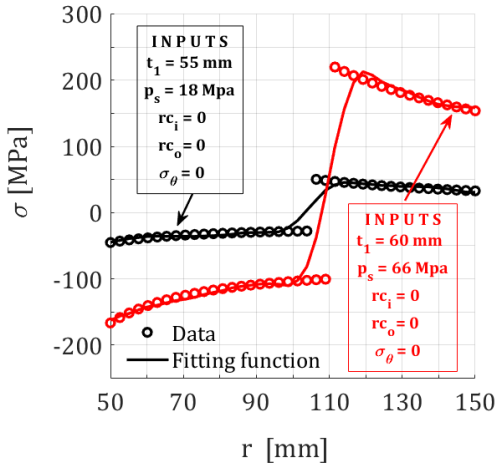

Figure 4-7. Residual hoop stress profile through the wall for the 3rd configuration

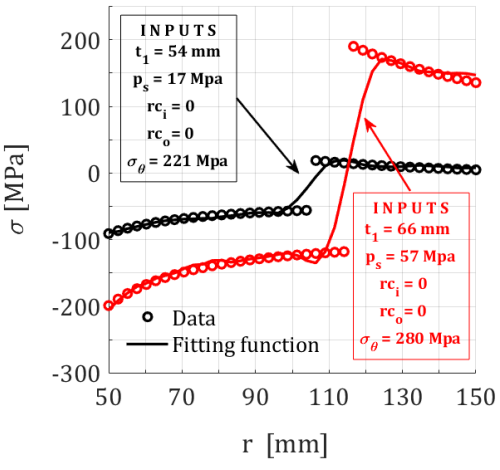

Figure 4-8. Residual hoop stress profile through the wall for the 4th configuration

As shown in Figure 4-5 to Figure 4-12, the resulting fitting functions demonstrate a strong agreement with the calculated residual stress data, as indicated by a coefficient of determination

error (R^2) of nearly 0.97. Each figure represents two different values of design variables (inputs) for each configuration.

Subsequently, the objective of minimizing the area under the residual stress profile across the wall thickness is pursued by using a genetic algorithm (GA) to obtain a near global optimum point. The optimal results from GA were then served as the initial points for the sequential quadratic programming (SQP) to identify accurate global optimal solutions. Table 4-5 lists optimum values of the design variables obtained using combined GA and SQP. Results show that $R_{co} = 0$ which means that outer layer should not be autofrettaged.

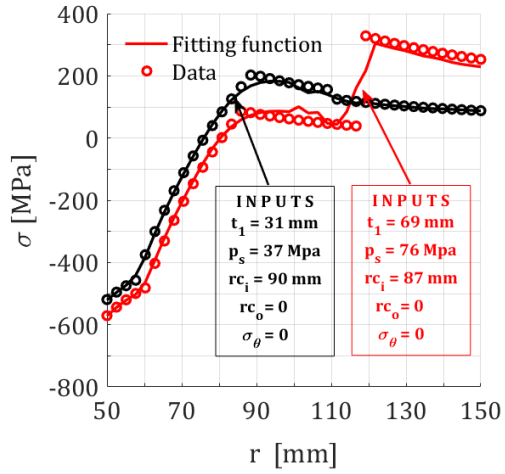

Figure 4-9. Residual hoop stress profile through the wall for the 5th configuration

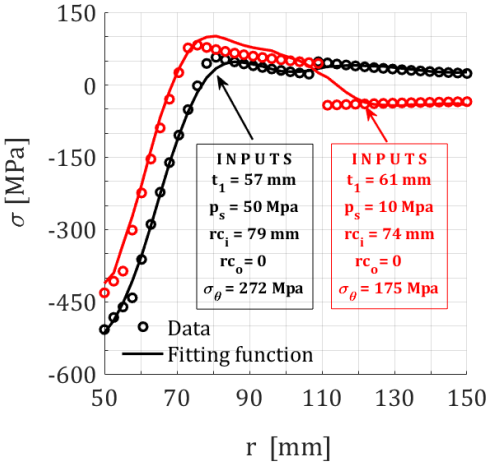

Figure 4-10. Residual hoop stress profile through the wall for the 6th configuration

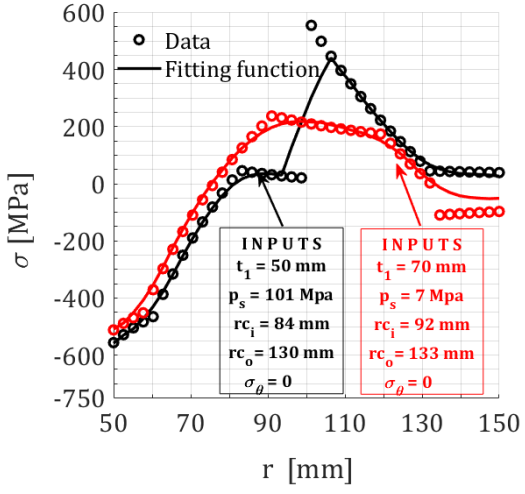

Figure 4-11. Residual hoop stress profile through the wall for the 7th configuration

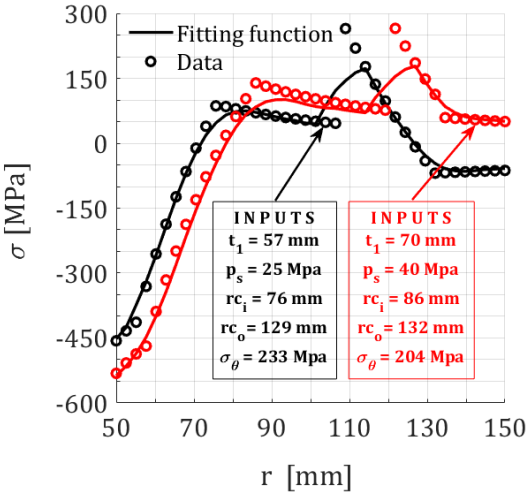

Figure 4-12. Residual hoop stress profile through the wall for the 8th configuration

Among 8 configurations listed in Table 4-1, only Configuration 6 (Inner autofrettage of the inner layer; then shrink fitting it with a virgin layer and final wire-winding of the entire assembly) has four design variables and the design variable R_{co} is zero. Thus Configuration 6 is the optimum configuration with optimal parameters stated in Table 4-5.

Table 4-5. The identified optimal design variables

Parameters	t_1 mm	p_s Mpa	R_{ci} mm	R_{co} mm	$\sigma_{\theta W}$ Mpa
Optimum Values	62.2	42.71	92.5	0	342.9

Figure 4-13 illustrates the hoop residual stress profile across the wall thickness for Configuration 6 using the optimum design variable values obtained from the ANN fitting function and the calculated data. Results demonstrate a strong agreement between the two profiles, highlighting the accuracy of the ANN fitting function beyond the dataset.

Finally, to evaluate the fatigue life, it is essential to consider the material factors specified by the ASME [11] for the material used in this study. According to the ASME codes, the crack growth rate factors, denoted as C_f and m_f, are specified as 3.64×10^{-9} mm/cycle and 3.26, *respectively*, according to the table KD-430M [11]. While, the free surface correction factors, denoted as G_{0-3}, are determined according to the table D-401.2 [11]. These factors are assigned the values of 0.7019, 0.1285, 0.0426, and 0.0194, respectively. Furthermore, the flaw shape parameter, denoted as Q_c, is set to 1.75, according to the code D-401 [11]. The thick-walled cylinder is subjected to cyclic inner pressure of 300 MPa. The Stress Intensity Factor (SIF) resulting from the working loads and residual stresses are then calculated according to the guidelines stated in Section 4.3 using Eqs. (4-3) to (4-6). Subsequently, the number of cycles until failure is determined based on Paris's law using Eqs. (4-7) to (4-10).

The total cycles until failure for the identified optimal configuration is found to be 88×10^6 cycles. In comparison, a virgin monobloc thick-walled cylinder with identical inner and outer radii under the same loading conditions exhibits a fatigue life of 78×10^3 cycles. Results clearly show a significant increase in fatigue life due to surface strength enhancement caused by the combination of inner autofrettage, shrink-fit and wire-winding processes.

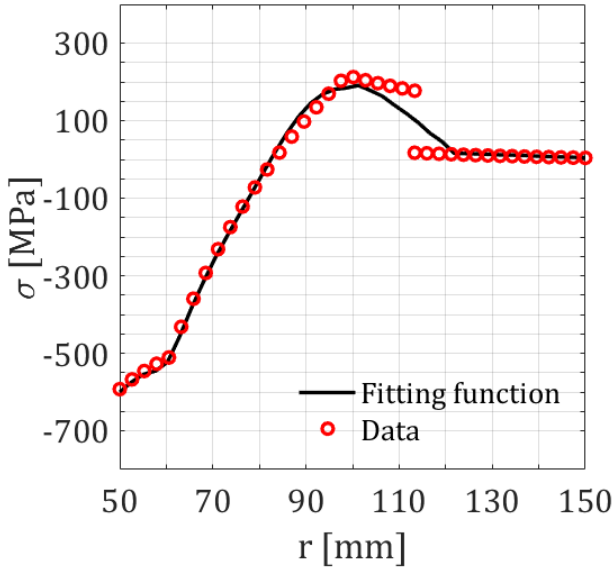

Figure 4-13. Optimum residual hoop stress profile through the wall thickness.

To further validate that Configuration #6 is the optimal configuration among the eight configurations, a comprehensive evaluation is conducted. This involves performing identical design optimization sequences for each configuration individually to obtain their respective optimum design variable values. Then, the fatigue life of each configuration is calculated under the same cyclic loading of 300 MPa, utilizing the corresponding optimal design variable values found during the design optimization process.

Table 4-6. The optimal design variables for each configuration

Parameters		t_1 mm	p_s Mpa	R_{ci} mm	R_{co} Mm	$\sigma_{\theta W}$ Mpa
Optimum Values	Configuration #1	-	-	120	-	-
	Configuration #2	-	-	100	-	175
	Configuration #3	70	9.2	-	-	
	Configuration #4	58.1	23.7	-	-	342.7
	Configuration #5	60	10	80.4	-	-
	Configuration #6	62.2	42.71	92.5	0	342.9
	Configuration #7	68	16.7	72.1	120.3	-
	Configuration #8	70.3	13.8	71.5	139	349

Table 4-6 presents the optimal design variables obtained from the design optimization solution for each configuration, while Table 7 presents the lifetimes associated with each optimal configuration under the cyclic load.

Table 4-7. The lifetime for each configuration

Configuration	#1	#2	#3	#4	#5	#6	#7	#8
Lifetime ($\times 10^6$)	16	25	7	19	51	88	41	63

Table 4-7 illustrates that Configuration 6 maintains the highest fatigue lifetime, with a value of 88×10^6 cycles as obtained before. This validated the proposed methodology to use machine learning to generate a single objective function that accurately fits different configurations, thus significantly reducing the time and effort required to perform multiple optimization solutions for each configuration. By avoiding the need for repetitive calculations and comparisons, the proposed approach accelerates the process of selecting the optimum design variable values and their corresponding configuration, making it more efficient and practical.

Moreover, as observed in Table 4-7, the wire-winding process significantly increases the fatigue lifetimes in thick-walled cylinder configurations 2, 4, 6, and 8, compared to their respective unwire-wound counterparts, namely, configurations 1, 3, 5, and 7. Additionally, shrink-fit combination 2 and its wire-wound counterpart 3 exhibit the shortest lifetimes when compared to any other combination and its wire-wound counterpart. This outcome can be attributed to the insufficient compressive residual stresses generated by the shrink-fit process and the abrupt transition of residual stress at the interface between the two layers, as depicted in Figure 4-7 and Figure 4-8, which impacts the overall area under the residual stress profile and consequently affecting the fatigue life.

Furthermore, upon closer examination of combinations 7 and 8, which involve an outer autofrettage process, the reason behind the shorter lifetimes compared with combinations 5 and 6 becomes apparent. The outer autofrettage increases the tensile stress at the interface between the two layers, as illustrated in Figure 4-11 and Figure 4-12. This additional tensile stress at the interface significantly affects the overall area under the residual stress profile and consequently influences the fatigue life of these configurations.

In the case of thermomechanical fatigue analysis, the identical geometric parameters discussed in this section remain consistent. However, in this scenario, the thick-walled cylinder is subjected to cyclic nonlinear thermomechanical loading conditions, as detailed in Section 2.4.3.

To provide a concise overview, each thermomechanical loading cycle follows pre-established profiles illustrated in Figure 2-10.

Table 4-8. SIF for different cycles and their corresponding mean temperature considering TIMP

Cycle No.	10^0	10^1	10^2	10^3	10^4	10^5	10^6
T_{mean} [K]	301.2	306.2	315.1	367	613	886.7	956.6
K_I $\left[MPa\sqrt{m}\right]$	-445	-325	-204	-155	-64	77	201

Table 4-9. SIF for different cycles and their corresponding mean temperature considering TDMP

Cycle No.	10^0	10^1	10^2	10^3	10^4	10^5	10^6
T_{mean} [K]	301.2	306.2	311.1	345.1	519	780	841.5
K_I $\left[MPa\sqrt{m}\right]$	-444	-322	-200	-144	-12	128	251

In a manner similar to the computation of the stress intensity factor due to cyclic mechanical loads, the stress intensity factor is determined using Eqs. (4-3)-(4-6). However, in this context, the calculation takes into consideration both residual stress and stress resulting from the applied thermomechanical loads. As the generated stress due to the cyclic thermomechanical loads varies for each cycle, the stress intensity factor and its corresponding mean temperature are evaluated after every set of cycles. Results for the stress intensity factors are provided in Table 4-8 and Table 4-9 addressing temperature-dependent material properties (TDMP) and temperature-independent material properties (TIMP), respectively.

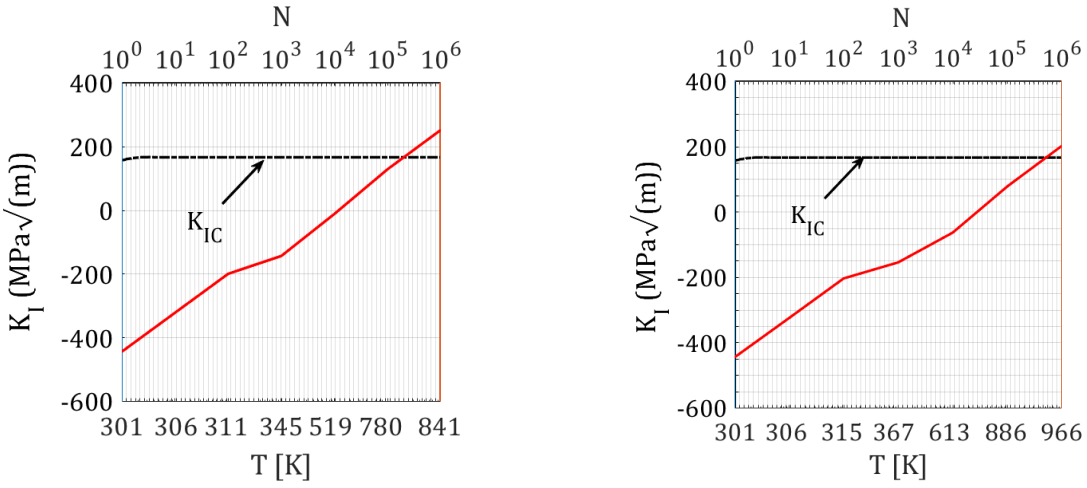

a) TDMP b) TIMP

Figure 4-14. Stress intensity factor versus number of cycles.

It is noteworthy to mention that the variation of critical stress intensity with respect to temperate for the utilized material is almost constant after 373 [K] [135]. Utilizing Table 4-8 and

4-9, the variation of stress intensity factor with respect to number of cycles and associated temperature are evaluated. Results for the stress intensity factor considering both TDMP and TIMP are shown in Figures 4-14 (a) and (b), respectively.

The failure point emerges when the stress intensity factor due to applied loads and residual stress converges towards the critical stress intensity factor. In this specific case, failure becomes apparent at around 3.8×10^5 cycles for TDMP and 7.5×10^5 cycles for TIMP, as displayed in Figure 4-14. This emphasizes the impact of cyclic thermomechanical loading conditions, in contrast to cyclic mechanical loading, which requires 88×10^6 cycles to induce failure for the same thick-walled cylinder. Moreover, this observation underscores the significance of considering TDMP. This is particularly crucial because TIMP tends to overestimate the fatigue lifetime when compared with TDMP, highlighting the necessity of considering the thermal and mechanical responses accurately.

4.5 Conclusion

In conclusion, this research paper utilizes the neural network (NN) regression method to investigate the optimal configuration and design parameters of thick-walled cylinders reinforced using shrink-fit, wire-winding, and autofrettage processes, aiming to enhance their fatigue life. The study initiates by generating various residual stress profiles across the thickness of single- or double-layer thick-walled cylinders, considering different combinations of the aforementioned reinforcement processes while adhering to consistent manufacturing sequences. In contrast to previous studies that derived a fitting function for each proposed configuration based on a single hoop residual stress value at either the inner or outer surface, followed by a comparison of optimum solutions to determine the best design, the proposed NN regression method derives a unique continuous fitting function that represents the hoop residual stress profiles for various thick-walled cylinder configurations. The obtained fitting function demonstrates a remarkable agreement with the calculated residual stress profiles, exhibiting a coefficient of determination error (R2) of over 0.97. Consequently, this approach eliminates the need for multiple fitting functions and enables a more comprehensive analysis of the distribution of residual stress.

Subsequently, the derived fitting function is utilized to implement the design optimization problem, aiming to enhance the beneficial compressive residual stress near the bore area and

minimize the detrimental tensile residual stress near the outer region. A genetic algorithm (GA) combined with sequential quadratic programming (SQP) optimization technique is effectively utilized to accurately capture the global optimal solution. The outcomes of the optimization process reveal that the sixth configuration emerges as the most favorable, offering a fatigue life of 88×10^6 lifetime cycles under cyclic pressure loads of 300MPa.

The proposed design methodology provides valuable insights into optimal design of reinforced thick-walled cylinders treated with shrink-fit, wire-winding, and autofrettage processes. The study also demonstrates the effectiveness of the NN regression method in accurately predicting residual stress profiles. By utilizing a single fitting function for multiple configurations, the present research study also offers an essential and practical guidance for enhancing the fatigue life of compound thick-walled cylinders in various engineering applications.

CHAPTER 5

CONCLUSIONS AND RECOMMENDATIONS

In this chapter, the key outcomes and conclusions of the present dissertation are presented, accompanied by recommendations for future research works. The primary aims of the dissertation revolved around the investigation of the behaviour of temperature-dependent thick-walled compound cylinders treated with combinations of reinforcement processes—namely, shrink-fit, hoop-winding, and autofrettage—and subjected to cyclic thermomechanical loads.

5.1 Conclusions

The significance of thick-walled cylinders in various industrial domains, ranging from petrochemical facilities and aerospace to military applications, underlines the motivation for ongoing and potential research efforts aimed to enhance their load-bearing capacities and durability. The challenges inherent in this realm revolve around the accurate evaluation of their behaviour when subjected to cyclic nonlinear thermomechanical loads, taking into consideration the temperature-dependent material properties. Notably, many existing models in this field exclusively account for temperature-independent material properties.

On this point, first, a solution method has been formulated to solve the coupled thermo-elasticity problem of temperature-dependent thick-walled cylinders subjected to cyclic thermomechanical loads. The proposed method has demonstrated its efficacy not only to precisely evaluate the thermal and mechanical responses but also to illuminate the necessity of incorporating temperature-dependent material properties rather than presuming temperature independence. In this context, the main significant takeaway can be summarized as follows:

- The proposed solution to the classical coupled thermo-elasticity problem for temperature-dependent thick-walled cylinders under cyclic nonlinear thermomechanical loads, which relies on the Crank-Nicolson method, offers a reasonably accurate outcome across various boundary conditions while being considerably time-efficient.
- Based on the experimental observation, it is shown that incorporating temperature-dependent material properties leads to an enhanced level of precision, specifically a 7% improvement, in comparison to the temperature-independent material properties

assumption. This improved accuracy highlights the significance of considering temperature-dependent material properties in the analysis.

Next, efficient analytical methodologies have been developed to accurately evaluate the induced residual stress profile through the thickness of compound cylinders treated with combinations of shrink-fit, hoop-winding, and autofrettage reinforcement processes. Compared with the computationally expensive finite element model, the proposed analytical methods allow for an efficient and accurate examination of the induced residual stress profile through the thickness of the compound cylinder and its dependence on the sequence of surface treatment processes as well as process parameters. Moreover, the proposed analytical methods permit the efficient formulation of a design optimization to identify the optimal configuration using machine learning. A central challenge in employing such advanced methods is the complicated task of generating extensive input-output datasets. These datasets necessitate the representation of residual hoop stress profiles across the thickness of the cylinder wall as outputs, accompanied by diverse design parameters as inputs. The complex nature of this challenge arises from the time-intensive process of generating these labelled datasets through finite element-based solutions. However, the proposed analytical solution can be effectively used to accelerate the generation of these labelled input-output datasets. The main related conclusions are:

- The developed analytical models can accurately and efficiently predict the residual stress profile in compound cylinders treated with any combination of shrink-fit, inner and outer autofrettage and wire-winding processes.
- The application of the machine learning approach exhibits promises in generating a continuous fitting function that accurately captures the residual stress profile through the cylinder wall.
- The central challenge in machine learning approach lies in the preliminary generation of accurately labelled datasets. This step is crucial to ensure the precision of the generated objective function and to mitigate the possibility of overfitting concerns. This aspect highlights the time-efficiency and significance of the proposed analytical solution.
- In contrast to previous methodologies, which required separate solutions for each distinct thick-walled cylinder configuration followed by subsequent comparisons to identify the

optimal design, the utilization of machine learning offers a more streamlined approach. This utilization enables the development of a singular objective function adaptable to various configurations, replacing the necessity for multiple solutions and comparisons.

- The machine learning approach also facilitates an efficient process to evaluate the fatigue life for the identified optimal design.
- The incorporation of temperature-dependent material properties contributes to a higher level of accuracy in estimating the lifetime of thick-walled cylinders subjected to cyclic thermomechanical loads. This inclusion enhances the reliability of the overall evaluation process.

In summation, this study contributes to the field by demonstrating the advantages of considering temperature-dependent material properties, unveiling insights into residual stress distributions, and showcasing the efficiency of a machine learning-guided optimization framework in enhancing accuracy and efficiency across various aspects of thick-walled cylinder analysis and design.

5.2 Recommendations for future works

This thesis has presented a comprehensive exploration of the evaluation of temperature-dependent thick-walled cylinders under cyclic nonlinear thermomechanical loading conditions, particularly those subjected to various reinforcement processes such as shrink-fit, hoop-winding, and autofrettage. While this research study has provided significant insights and essential guidance for efficient analysis and design optimization of compound cylinders treated with various combination of reinforcement processes, several recommendations are outlined for future research as:

- Exploring Generalized Thermo-elasticity Theories: While the present work is centered on the solution of classical coupled thermo-elasticity assuming infinite thermal wave propagation speeds, it is recommended to delve into generalized theories of thermo-elasticity that are founded on finite thermal wave speeds. Comparing these theories with classical formulations and experimental data would enrich our understanding.
- Investigating Multilayered Cylinders: This study primarily focuses on the design optimization of two-layered thick-walled cylinders. To provide a comprehensive

assessment of durability, further exploration is required for three- and multi-layered configurations and comparing their performance with the established two-layered configurations.

- Evaluating Swage Autofrettage: While hydraulic autofrettage with axisymmetric loads has been extensively investigated in this study, it is essential to investigate swage autofrettage, which relies on mechanical loads. A comparative analysis of residual stress profiles generated by the hydraulic and swage methods is recommended. Additionally, extending the design optimization framework to incorporate swage autofrettage and subsequent durability comparisons would enrich the study.
- In-Depth Exploration of Machine Learning: The novel machine learning-based design optimization approach discussed in this thesis demonstrates promising results, displaying superior time efficiency compared to prior methodologies. To further enhance its robustness, deeper investigations are suggested. These could include trying out neural network architectures with more than three hidden layers or looking into other regression models instead of neural network regression, like polynomial regression and surrogate models. A comprehensive analysis of the impacts of these alterations on the obtained results would provide valuable insights.

In brief, the outlined recommendations for future research efforts have the potential to advance the understanding of temperature-dependent compound thick-walled cylinders and their responses to complex thermomechanical loading scenarios.

REFERENCES

[1] K. Braun, "WHO DISCOVERED GUNPOWDER?" *Van Nostrand's Engineering Magazine (1879-1886)*, vol. 29, no. 176, p. 125, 1883.

[2] A. Partovi and S. S. Shamili, "Analysis of autofrettaged high pressure components," *Master Thesis, Department of Mechanical Engineering, Blekinge Institute of Technology, Kalskrona, Sweden*, 2012.

[3] G. Lamé, *Leçons sur la théorie mathématique de l'élasticité des corps solides (2nd ed.)*. Paris: Gauthier-Villars: Bachelier, 1866.

[4] M. Sedighi and A. H. Jabbari, "Investigation of residual stresses in thick-walled vessels with combination of autofrettage and wire-winding," *Int. J. Pressure Vessels Piping*, vol. 111–112, pp. 295–301, 2013, doi: 10.1016/j.ijpvp.2013.09.003.

[5] M. Sedighi and A. H. Jabbari, "A new analytical approach for wire-wound frames used to carry the loads of pressure vessel closures," *J Press Vessel Technol*, vol. 135, no. 6, p. 61206, 2013.

[6] L. E. Brownell and E. H. Young, *Process equipment design: vessel design*. John Wiley & Sons, 1959.

[7] L. Y. Maksimov, "Design of cylinder to withstand high internal pressure," *Russian Engineering Journal (Translation)*, vol. 44, no. 5, 1964.

[8] G. Harkegard, "A Procedure for the Analysis of Wire-Wound Structures and Its Application to the Optimum Design of Vessels for High Pressure," *Institution of Mechanical Engineers,* pp. 375–379, 1980.

[9] J. Talako, "Structure and analysis of wound pressure vessel." Chapman & Hall, New York, 1998.

[10] D. M. Fryer, J. F. Harvey, D. M. Fryer, and J. F. Harvey, *High pressure vessels*. Springer, 1998.

[11] A. Boiler and P. V. Committee, *Rules for Construction of Pressure Vessels: Alternative Rules for Construction of High-Pressure Vessels. VIII. Division 3*. American Society of Mechanical Engineers, 2007.

[12] Y. H. Song, Y. N. Yan, and R. J. Zhang, "Finite element analysis of the prestress wire-winding press," *J Mater Process Technol*, vol. 151, no. 1–3, pp. 255–257, 2004.

[13] J. M. Alegre, P. Bravo, M. Preciado, and M. Solaguren-Beascoa, "Simulation procedure of high-pressure vessels using the wire winding technique," *Eng Fail Anal*, vol. 17, no. 1, pp. 61–69, 2010.

[14] J. M. Alegre, P. M. Bravo, and I. I. Cuesta, "Fatigue design of wire-wound pressure vessels using ASME-API 579 procedure," *Eng Fail Anal*, vol. 17, no. 4, pp. 748–759, 2010.

[15] A. P. I. Api, “579-1/ASME FFS-1: Fitness-for-service.” American Petroleum Institute, 2007.

[16] K. E. Bett and D. J. Burns, “Paper 31: Design of Elastic Multi-Component Compound Cylinders,” in *Proceedings of the Institution of Mechanical Engineers, Conference Proceedings*, SAGE Publications Sage UK: London, England, 1967, pp. 22–29.

[17] S. J. Becker and L. Mollick, “The theory of the ideal design of a compound vessel,” 1960.

[18] C. Dimitriou, “Stresses in short thick compound cylinder,” *South African Mechanical Engineer*, vol. 19, no. 5, pp. 127–130, 1969.

[19] G. H. Majzoobi and A. Ghomi, “Optimisation of compound pressure cylinders,” *Journal of Achievements in Materials and Manufacturing Engineering*, vol. 15, no. 1–2, pp. 135–145, 2006.

[20] S. A. Patil, “Optimum design of compound cylinders used for storing pressurized fluids,” in *ASME International Mechanical Engineering Congress and Exposition*, 2005, pp. 713–716.

[21] S. A. Patil, “Fatigue analysis of compound cylinder subjected to repeated internal pressure,” in *ASME Pressure Vessels and Piping Conference*, 2006, pp. 553–557.

[22] R. D. Venter and M. C. De Malherbe, “The maximization of internal pressure in compound cylinders for a specified degree of plastic deformation,” *Int J Mech Sci*, vol. 12, no. 3, pp. 259–266, 1970.

[23] Y. Yong-Nian, Y. Xin-Lu, and G. He-De, “Optimum design of a cylinder under superhigh pressure by utilizing the complex method,” *Ching Hua Ta Hsueh Hsueh Pao/Journal of Ching Hua University*, vol. 22, no. 3, pp. 103–114, 1982.

[24] Y. Gexia, L. Hongzhao, and W. Zhongmin, “Optimum design for shrink-fit multi-layer vessels under ultrahigh pressure using different materials,” *Chinese journal of mechanical engineering*, no. 5, p. 582, 2010.

[25] Y. Ge-xia and L. I. U. Hong-zhao, “Optimum design of compound cylinders with sintered carbide inner liner under ultrahigh pressure,” 工程力学, vol. 28, no. 1, pp. 212–218, 2011.

[26] P. Pedersen, “On shrink fit analysis and design,” *Comput Mech*, vol. 37, no. 2, pp. 121–130, 2006, doi: 10.1007/s00466-005-0664-7.

[27] U. Güven, “Stress distribution in shrink fit with elastic-plastic hub exhibiting variable thickness,” *Int. J. Mech. Sci.*, vol. 35, no. 1, pp. 39–46, 1993, doi: 10.1016/0020-7403(93)90063-Z.

[28] U. Gamer, “The shrink-fit with nonlinearly hardening elastic-plastic hub,” *J. Appl. Mech.*, 1987, doi: 10.1115/1.3173048.

[29] U. Gamer and R. H. Lance, “Residual stress in shrink fits,” *Int. J. Mech. Sci.*, vol. 25, no. 7, pp. 465–470, 1983, doi: 10.1016/0020-7403(83)90039-5.

[30] M. Sharifi, J. Arghavani, and M. R. Hematiyan, “An analytical solution for optimum design of shrink-fit multi-layer compound cylinders,” *Int J Appl Mech*, vol. 4, no. 04, p. 1250043, 2012.

[31] T. E. Davidson, D. P. Kendall, and A. N. Reiner, “Residual Stresses in Thick-Walled Cylinders Resulting from Mechanically Induced Overstrain,” *Exp Mech*, vol. 3, pp. 253–262, 1963.

[32] G. P. O’Hara, “Analysis of the swage autofrettage process,” *US Army ARDEC Technical Report ARCCB-TR-92016, Benét Laboratories, Watervliet Arsenal, NY*, vol. 12189, 1992.

[33] M. J. Iremonger and G. S. Kalsi, “A numerical study of swage autofrettage,” *J. Pressure Vessel Technol.*, vol. 125, no. 3, pp. 347–351, 2003.

[34] B. Avitzur, “Determination of residual stress distributions in autofrettaged tubing,” *International journal of pressure vessels and piping*, vol. 38, no. 2, pp. 147–157, 1989.

[35] B. Avitzur, “Autofrettage—Stress distribution under load and retained stresses after depressurization,” *International journal of pressure vessels and piping*, vol. 57, no. 3, pp. 271–287, 1994.

[36] X. P. Huang and W. C. Cui, “Effect of Bauschinger effect and yield criterion on residual stress distribution of autofrettaged tube,” *J. Pressure Vessel Technol.*, 2006, doi: 10.1115/1.2172621.

[37] S.-C. Chu, “A more rational approach to the problem of an elastoplastic thick-walled cylinder,” *J Franklin Inst*, vol. 294, no. 1, pp. 57–65, 1972.

[38] H. Jahed, R. Sethuraman, and R. N. Dubey, “Variable Material Properties approach in Elastic-Plastic Solution of Thick-Walled Cylinders,” in *Mechanics in Design, Ed. Meguid, SA, CSME Forum, Toronto*, 1996, pp. 187–197.

[39] R. V Milligan, W. H. Koo, and T. E. Davidson, “The Bauschinger effect in a high-strength steel,” 1966.

[40] A. P. Parker, M. C. Gibson, A. Hameed, E. Troiano, and J. G. Hetherington, “Material Modeling for Autofrettage Stress Analysis Including the ‘Single Effective Material,’” in *ASME Pressure Vessels and Piping Conference*, 2008, pp. 49–61.

[41] P. C. T. Chen, “Generalized plane-strain problems in an elastic-plastic thick-walled cylinder,” in *Trans. 26th Conference of Army Mathematicians*, 1980, pp. 265–275.

[42] P. C. T. Chen, “Stress and deformation analysis of autofrettaged high pressure vessels,” *ASME special publication*, vol. 110, pp. 61–67, 1986.

[43] W. Y. Lu and H. S. U. YC, “ELASTIC-PLASTIC ANALYSIS OF A FLAT RING SUBJECT TO INTERNAL PRESSURE.,” 1977.

[44] J. Perry and J. Aboudi, “Elasto-plastic stresses in thick-walled cylinders,” *J. Pressure Vessel Technol.*, vol. 125, no. 3, pp. 248–252, 2003.

[45] T. E. Davidson, C. S. Barton, A. N. Reiner, and D. P. Kendall, “Overstrain of high-strength open-end cylinders of intermediate diameter ratio,” in *Experimental Mechanics*, Elsevier, 1963, pp. 335–352.

[46] A. S. Elder, R. C. Tomkins, and T. L. Mann, “Generalized Plane Strain in an Elastic, Perfectly Plastic Cylinder, With Reference to the Hydraulic Autofrettage Process,” in *Trans. 2l8t Conference of Army Mathematicians*, 1975, pp. 623–659.

[47] S. Alexandrov, W. Jeong, and K. Chung, “Descriptions of reversed yielding in internally pressurized tubes,” *J Press Vessel Technol*, vol. 138, no. 1, p. 011204, 2016.

[48] R. Hill, E. H. Lee, and S. J. Tupper, “The theory of combined plastic and elastic deformation with particular reference to a thick tube under internal pressure,” *Proc R Soc Lond A Math Phys Sci*, vol. 191, no. 1026, pp. 278–303, 1947.

[49] X.-L. Gao, J.-F. Wen, F.-Z. Xuan, and S.-T. Tu, “Autofrettage and shakedown analyses of an internally pressurized thick-walled cylinder based on strain gradient plasticity solutions,” *J Appl Mech*, vol. 82, no. 4, p. 041010, 2015.

[50] L. Jacob, “La Résistance et L’équilibre Élastique des tubes Frettés,” *Memorial de L’artillerie Navale*, vol. 1, no. 1907, pp. 43–155, 1907.

[51] T. E. Davidson, C. S. Barton, A. N. Reiner, and D. P. Kendall, “New approach to the autofrettage of high-strength cylinders,” *Exp Mech*, vol. 2, pp. 33–40, 1962.

[52] J. D. Mote, L. K. W. Ching, R. E. Knight, R. J. Fay, and M. A. Kaplan, “Explosive autofrettage of cannon barrels,” *Army Materials and Mechanics Research Center, Watertown, MA, Report No. AMMRC CR*, pp. 25–70, 1971.

[53] S. M. Kamal and U. S. Dixit, “Feasibility study of thermal autofrettage of thick-walled cylinders,” *J Press Vessel Technol*, vol. 137, no. 6, p. 061207, 2015.

[54] H. R. Zare and H. Darijani, “A novel autofrettage method for strengthening and design of thick-walled cylinders,” *Mater Des*, vol. 105, pp. 366–374, 2016.

[55] R. Shufen and U. S. Dixit, “A review of theoretical and experimental research on various autofrettage processes,” *J Press Vessel Technol*, vol. 140, no. 5, p. 050802, 2018.

[56] A. P. Parker, “Compound and Monobloc Cylinders Incorporating Reverse-Autofrettage to Reduce External Hoop Stresses,” in *Proceedings of ASME PVP2012 Pressure Vessels and Piping Division Conference*, American Society of Mechanical Engineers, p. July 15–19, Toronto, Ontario, Canada, Paper No. PV. doi: 10.1115/PVP2012-78298.

[57] J. Baushinger, “Ueber die Veranderung der Elasticitatsgrenze und des Elasticitatsmoduls verschuedener Metalle,” *zivilingenieur*, vol. 27, p. column-289, 1881.

[58] P. Lazzarin and P. Livieri, “Different solutions for stress and strain fields in autofrettaged thick-walled cylinders,” *International journal of pressure vessels and piping*, vol. 71, no. 3, pp. 231–238, 1997.

[59] A. Ghorbanpour, A. Loghman, H. Khademizadeh, and M. Moradi, “The bauschinger and hardening effect on residual stresses in thick-walled cylinders of SUS 304,” *Trans CSME*, vol. 26, no. 4, pp. 361–372, 2003, doi: 10.1139/tcsme-2002-0021.

[60] A. P. Parker and J. H. Underwood, “Influence of the bauschinger effect on residual stress and fatigue lifetimes in autofrettaged thick-walled cylinders,” Panontin Tl, Sheppard SD, editors, Fatigue and fracture mechanics, ASTM STP 1321, vol. 29, Philadelphia: ASTM, 1998.

[61] P. G. Hodge Jr and G. N. White Jr, “A quantitative comparison of flow and deformation theories of plasticity,” 1950.

[62] H. Jahed and R. N. Dubey, “An axisymmetric method of elastic-plastic analysis capable of predicting residual stress field,” 1997.

[63] A. P. Parker, “Autofrettage of open-end tubes—pressures, stresses, strains, and code comparisons,” *J. Pressure Vessel Technol.*, vol. 123, no. 3, pp. 271–281, 2001, doi: 10.1115/1.1359209.

[64] O. R. Abdelsalam, “IMPROVEMENT OF RESIDUAL STRESSES IN THICK WALL CYLINDERS USING MULTIPLE AUTOFRETTAGE,” in *The International Conference on Applied Mechanics and Mechanical Engineering*, Military Technical College, 2014, pp. 1–13.

[65] O. R. Abdelsalam, “The behavior of residual stress under cyclic thermo-mechanical loads in autofrettaged and shrink-fitted cylinders,” *IJIERT*, vol. 8, no. 6, 2021.

[66] J. A. Kapp, B. B. Brown, E. J. LaBombard, and H. A. Lorenz, “On the design of high durability high pressure vessels,” *Proceedings of ASME PVP Conference*, ASME, p. San Diego, July 1998, ASME PVP, Vol. 37, pp. 85–91, 1998.

[67] A. P. Parker, “Bauschinger effect design procedures for compound tubes containing an autofrettaged layer,” *J. Pressure Vessel Technol.*, vol. 123, no. 2, pp. 203–206, 2001, doi: 10.1115/1.1331281.

[68] D. P. Kendall, “The effect of material removal on the strength of autofrettaged cylinders.,” Benet R&E Laboratories, Watervliet Arsenal, New York, 1970.

[69] A. P. Parker, J. H. Underwood, and D. P. Kendall, “Bauschinger effect design procedures for autofrettaged tubes including material removal and Sachs’ method,” *J. Pressure Vessel Technol.*, 1999, doi: doi.org/10.1115/1.2883726.

[70] H. Jahed and G. Ghanbari, “Actual unloading behavior and its significance on residual stress in machined autofrettaged tubes,” *J. Pressure Vessel Technol.*, vol. 125, no. 3, pp. 321–325, 2003, doi: 10.1115/1.1593070.

[71] E.-Y. Lee, Y.-S. Lee, Q.-M. Yang, J.-H. Kim, K.-U. Cha, and S.-K. Hong, “Autofrettage process analysis of a compound cylinder based on the elastic-perfectly plastic and strain

hardening stress-strain curve," *Journal of Mechanical Science and Technology*, vol. 23, pp. 3153–3160, 2009.

[72] Y. Gexia and L. Hongzhao, "An analytical solution of residual stresses for shrink-fit two-layer cylinders after autofrettage based on actual material behavior," *J. Pressure Vessel Technol.*, vol. 134, no. 6, 2012, doi: 10.1115/1.4006121.

[73] O. R. Abdelsalam and R. Sedaghati, "Outer Surface Prior to Inner Surface Double Autofrettage Technique for a Compound Cylinder," in *Proceedings of ASME PVP2013 Pressure Vessels and Piping Division Conference*, American Society of Mechanical Engineers. doi: 10.1115/PVP2013-97035.

[74] A. Ayob and M. K. Elbasheer, "Optimum autofrettage pressure in thick cylinders," *Jurnal Mekanikal*, 2007.

[75] H. Jahed, B. Farshi, and M. Karimi, "Optimum autofrettage and shrink-fit combination in multi-layer cylinders," *J. Pressure Vessel Technol.*, 2006, doi: 10.1115/1.2172957.

[76] N. Kumar, S. C. Mondal, D. K. Mandal, and S. K. Acharyaa, "Optimum autofrettage pressure and shrink-fit combination for minimum stress in multilayer pressure vessel," *International Journal of Engineering, Science and Technology*, vol. 3, no. 5, pp. 4020–4030, 2011.

[77] O. R. Abdelsalam and R. Sedaghati, "Design optimization of compound cylinders subjected to autofrettage and shrink-fitting processes," *J. Pressure Vessel Technol.*, vol. 135, no. 2, 2013, doi: 10.1115/1.4007960.

[78] O. R. Abdelsalam, "Design optimization for a three-layers shrink-fitted pressure vessel exposed to very high pressure," in *IOP Conference Series: Materials Science and Engineering*, IOP Publishing, 2019, p. 12077.

[79] S. K. Koh, "Fatigue life simulation and estimation of an autofrettaged thick-walled pressure vessel with an external groove," *Int J Fatigue*, vol. 18, no. 1, pp. 49–56, 1996.

[80] J. H. Underwood and E. Troiano, "Critical fracture processes in army cannons: a review," *J. Pressure Vessel Technol.*, vol. 125, no. 3, pp. 287–292, 2003.

[81] E. Petitpas and B. Campion, "Crack propagation in a gun barrel due to the firing thermo-mechanical stresses," *J. Pressure Vessel Technol.*, vol. 125, no. 3, pp. 293–298, 2003.

[82] H. Jahed, B. Farshi, and M. Hosseini, "Life prediction of autofrettage tubes using actual material behavior," *Int J Pres Ves Pip*, 2005.

[83] J. M. Alegre, I. I. Cuesta, and P. M. Bravo, "Comparative Study of Different Fatigue Crack Growth Methods for the Design of Wire-Wound Vessels," *http://*, 2010.

[84] S. M. Nabavi and A. R. Shahani, "Thermal stress intensity factors for a cracked cylinder under transient thermal loading," *International Journal of Pressure Vessels and Piping*, vol. 86, no. 2–3, pp. 153–163, 2009.

[85] S. M. Nabavi and R. Ghajar, “Analysis of thermal stress intensity factors for cracked cylinders using weight function method,” *Int J Eng Sci*, vol. 48, no. 12, pp. 1811–1823, 2010.

[86] H. Jahed, B. Farshi, and M. Hosseini, “Fatigue life prediction of autofrettage tubes using actual material behaviour,” *International journal of pressure vessels and piping*, vol. 83, no. 10, pp. 749–755, 2006.

[87] A. P. Parker and D. P. Kendall, “Residual stresses and lifetimes of tubes subjected to shrink fit prior to autofrettage,” *J. Pressure Vessel Technol.*, vol. 125, no. 3, pp. 282–286, 2003.

[88] O. R. Abdelsalam and R. Sedaghati, “Coupled thermomechanical analysis of autofrettaged and shrink-fitted compound cylindrical shells,” *J Press Vessel Technol*, vol. 136, no. 1, p. 11204, 2014.

[89] O. R. Abdelsalam, “Analysis and optimization of autofrettaged and shrink-fitted compound cylinders under thermo-mechanical loads,” 2012.

[90] A. Şentürk, H. Işık, and C. Evci, “Thermo-mechanically coupled thermal and stress analysis of interior ballistics problem,” *International Journal of Thermal Sciences*, vol. 104, pp. 39–53, 2016.

[91] A. M. Farhan, A. M. Abd-Alla, and M. A. Khder, “Solution of a problem of thermal stresses in a non-homogeneous thermoelastic infinite medium of isotropic material by finite difference method,” *Journal of Ocean Engineering and Science*, vol. 4, no. 3, pp. 256–262, 2019.

[92] R. B. Hetnarski, M. R. Eslami, and G. M. L. Gladwell, *Thermal stresses: advanced theory and applications*, vol. 41. Springer, 2009.

[93] J. M. C. Duhamel, “Second memoire sur les phenomenes thermo-mecaniques,” *Journal de l’École polytechnique*, vol. 15, no. 25, pp. 1–57, 1837.

[94] M. Jabbari, H. Dehbani, and M. R. Eslami, “An exact solution for classic coupled thermoelasticity in cylindrical coordinates,” *J Press Vessel Technol*, vol. 133, no. 5, 2011.

[95] M. A. Kouchakzadeh and A. Entezari, “Analytical solution of classic coupled thermoelasticity problem in a rotating disk,” *Journal of Thermal Stresses*, vol. 38, no. 11, pp. 1267–1289, 2015.

[96] D. Haojiang, G. Fenglin, and H. Pengfei, “General solutions of coupled thermoelastic problem,” *Appl Math Mech*, vol. 21, pp. 631–636, 2000.

[97] R. B. Hetnarski, “Solution of the coupled problem of thermoelasticity in the form of series of functions,” *Archiwum Mechaniki Stosowanej*, vol. 16, no. 4, pp. 919–941, 1964.

[98] Z.-Y. Lee, C.-K. Chen, and C.-I. Hung, “Hybrid numerical method applied to multilayered hollow cylinder with time-dependent boundary conditions,” *Journal of Thermal Stresses*, vol. 28, no. 8, pp. 839–860, 2005.

[99] D. D. J. Tao, “A numerical technique for dynamic coupled thermoelasticity problems with relaxation times,” *Journal of Thermal Stresses*, vol. 12, no. 4, pp. 483–487, 1989.

[100] A. M. Abd-Alla, S. R. Mahmoud, and S. M. Abo-Dahab, “On problem of transient coupled thermoelasticity of an annular fin,” *Meccanica*, vol. 47, pp. 1295–1306, 2012.

[101] A. M. Zenkour and I. A. Abbas, “A generalized thermoelasticity problem of an annular cylinder with temperature-dependent density and material properties,” *Int J Mech Sci*, vol. 84, pp. 54–60, 2014.

[102] I. A. Abbas, “Nonlinear transient thermal stress analysis of thick-walled FGM cylinder with temperature-dependent material properties,” *Meccanica*, vol. 49, no. 7, pp. 1697–1708, 2014.

[103] M. Elfar, R. Sedaghati, and O. R. Abdelsalam, “Transient coupled thermo-elasticity analysis of a temperature-dependent thick-walled cylinder under cyclic thermo-mechanical loads,” *SN Appl Sci*, vol. 5, no. 1, p. 9, 2023.

[104] R. B. Hetnarski and J. Ignaczak, “Generalized thermoelasticity: closed-form solutions,” *Journal of Thermal Stresses*, vol. 16, no. 4, pp. 473–498, 1993.

[105] H. H. Sherief and M. N. Anwar, “Problem in generalized thermoelasticity,” *Journal of Thermal Stresses*, vol. 9, no. 2, pp. 165–181, 1986.

[106] Y. Y. LI, H. GRONEIM, Y. CHEN, and J. DAVIS, “A numerical method in solving a coupled thermoelasticity equation and some results [Final Report],” 1983.

[107] J.-H. Prevost and D. Tao, “Finite element analysis of dynamic coupled thermoelasticity problems with relaxation times,” 1983.

[108] B. A. Boley and J. H. Weiner, *Theory of thermal stresses*. Courier Corporation, 2012.

[109] N. Noda, *Thermal stresses*. Routledge, 2018.

[110] A. Kandil, A. A. El-Kady, and A. El-Kafrawy, “Transient thermal stress analysis of thick-walled cylinders,” *Int J Mech Sci*, vol. 37, no. 7, pp. 721–732, 1995.

[111] A. R. Shahani and S. M. Nabavi, “Analytical solution of the quasi-static thermoelasticity problem in a pressurized thick-walled cylinder subjected to transient thermal loading,” *Appl Math Model*, vol. 31, no. 9, pp. 1807–1818, 2007.

[112] A. H. Ghosn and M. Sabbaghian, “Quasi-static coupled problems of thermoelasticity for cylindrical regions,” *Journal of Thermal Stresses*, vol. 5, no. 3–4, pp. 299–313, 1982.

[113] A. E. Segall, “Thermoelastic analysis of thick-walled vessels subjected to transient thermal loading,” *J. Pressure Vessel Technol.*, vol. 123, no. 1, pp. 146–149, 2001.

[114] M. A. Kouchakzadeh, A. Entezari, and E. Carrera, “Exact solutions for dynamic and quasi-static thermoelasticity problems in rotating disks,” *Aerotecnica Missili & Spazio*, vol. 95, pp. 3–12, 2016.

[115] A. Entezari, “Solution of coupled thermoelasticity problem in rotating disks,” *Department of Mechanical and Aerospace Engineering, Politecnico di Torino, Turin, Italy*, 2017.

[116] L. D. Landau, E. M. Lifshitz, A. M. Kosevich, and L. P. Pitaevskii, *Theory of elasticity: volume 7*, vol. 7. Elsevier, 1986.

[117] J. P. Holman, “Heat transfer.” McGraw Hill Higher Education, 2010.

[118] F. P. Incropera, D. P. DeWitt, T. L. Bergman, and A. S. Lavine, *Fundamentals of heat and mass transfer*, vol. 6. Wiley New York, 1996.

[119] M. J. Moran, H. N. Shapiro, D. D. Boettner, and M. B. Bailey, *Fundamentals of engineering thermodynamics*. John Wiley & Sons, 2010.

[120] H. Cho, G. A. Kardomateas, and C. S. Valle, “Elastodynamic solution for the thermal shock stresses in an orthotropic thick cylindrical shell,” 1998.

[121] H. J. Ding, H. M. Wang, and W. Q. Chen, “A solution of a non-homogeneous orthotropic cylindrical shell for axisymmetric plane strain dynamic thermoelastic problems,” *J Sound Vib*, vol. 263, no. 4, pp. 815–829, 2003.

[122] S. (Ed.) Hoyt, *ASME Handbook, Metals Properties; McGraw Hill Book Company*. doi: 10.3390/met9050560.

[123] J. Corner, *Theory of the interior ballistics of guns*. Wiley, 1950.

[124] R. D. Hill and J. M. Conner, “Transient heat transfer model of machine gun barrels,” *Materials and Manufacturing Processes*, vol. 27, no. 8, pp. 840–845, 2012.

[125] D. P. Kendall, “A short history of high-pressure technology from bridgman to division 3,” *J. Pressure Vessel Technol.*, vol. 122, no. 3, pp. 229–233, 2000.

[126] M. Elfar, R. Sedaghati, and O. R. Abdelsalam, “Analytical Formulation to Predict Residual Stresses in Thick-walled Cylinders Subjected to Hoop Winding, Shrink-Fit, and Conventional and Reverse Autofrettages,” *J Press Vessel Technol*, vol. "Under Rev, Apr. 2023.

[127] J. Li, D. Zheng, Z. Zhang, F. Wang, Y. Wang, and X. Wang, “Simulation Analysis of Cylinder Winding Prestress Based on Ansys,” in *Proceedings of Journal of Physics: Conference Series*, IOP Publishing, 2022, p. 12006. doi: 10.1088/1742-6596/2185/1/012006.

[128] A. P. Parker, “Assessment and extension of an analytical formulation for prediction of residual stress in autofrettaged thick cylinders,” in *ASME Pressure Vessels and Piping Conference*, 2005, pp. 67–71. doi: 10.1115/PVP2005-71368.

[129] M. H. Hojjati and A. Hassani, “Theoretical and finite-element modeling of autofrettage process in strain-hardening thick-walled cylinders,” *Int. J. Pressure Vessels Piping*, vol. 84, no. 5, pp. 310–319, 2007, doi: 10.1016/j.ijpvp.2006.10.004.

[130] G. H. Farrahi, S. A. Faghidian, and D. J. Smith, “Reconstruction of residual stresses in autofrettaged thick-walled tubes from limited measurements,” *Int. J. Pressure Vessels Piping*, vol. 86, no. 11, pp. 777–784, 2009, doi: 10.1016/j.ijpvp.2009.03.010.

[131] E. Hosseinian, G. H. Farrahi, and M. R. Movahhedy, “An analytical framework for the solution of autofrettaged tubes under constant axial strain condition,” *J. Pressure Vessel Technol.*, vol. 131, no. 6, 2009, doi: 10.1115/1.3148082.

[132] W.-F. Chen and D.-J. Han, *Plasticity for structural engineers*. New York: Springer, 1988.

[133] and O. R. A. M. Elfar, R. Sedaghati, “Design Optimization of Compound Thick-Walled Cylinders Treated with Autofrettage, Shrink-Fit and Wire-Winding Processes using Neural Network Regression,” *J. Pressure Vessel Technol.*, vol. “Under Rev.

[134] A. P. Mouritz, *Introduction to aerospace materials*. Elsevier, 2012.

Appendices (A-C)

Appendix A

The Crank-Nicolson finite difference discretization for Eqs (2-4) and (2-9) with mixed boundary conditions (2-10) and (2-11) is given by:

(1) For the radial displacement $u(r,t)$ Eq.):

$$\frac{\partial^2 u_r}{\partial r^2}+\frac{1}{r}\frac{\partial u_r}{\partial r}-\frac{u_r}{r^2}-\frac{\alpha(1+\nu)}{(1-\nu)}\frac{\partial T}{\partial r}-\frac{\rho\,(1+\nu)(1-2\nu)}{\mathrm{E}\,(1-\nu)}\ddot{u}_r=0$$

Applying the Crank-Nicolson finite difference discretization,

$$\begin{aligned}&\frac{1}{2\Delta r^2}\left(u_{j+1}^{n+1}-2u_j^{n+1}+u_{j-1}^{n+1}+u_{j+1}^{n}-2u_j^{n}+u_{j-1}^{n}\right)\\&+\frac{1}{4\Delta r}\frac{1}{r_j}\left(u_{j+1}^{n+1}-u_{j-1}^{n+1}+u_{j+1}^{n}-u_{j-1}^{n}\right)\\&-\frac{1}{4{r_j}^2}\left(u_{j+1}^{n+1}+u_{j-1}^{n+1}+u_{j+1}^{n}+u_{j-1}^{n}\right)\\&-\frac{\alpha(1+\nu)}{(1-\nu)}\frac{1}{4\Delta r}\left(T_{j+1}^{n+1}-T_{j-1}^{n+1}+T_{j+1}^{n}-T_{j-1}^{n}\right)\\&-\frac{\rho\,(1+\nu)(1-2\nu)}{\mathrm{E}\,(1-\nu)}\frac{1}{\Delta t^2}\left(u_j^{n+1}-2u_j^{n}+u_j^{n-1}\right)=0\end{aligned}$$

After rearranging next time step (n+1) in one side and the previous time steps in the other sides the displacement equation will be,

$$\begin{aligned}\Rightarrow&\overbrace{\frac{\alpha(1+\nu)}{(1-\nu)}\frac{1}{4\Delta r}}^{A_j}T_{j-1}^{n+1}\overbrace{-\frac{\alpha(1+\nu)}{(1-\nu)}\frac{1}{4\Delta r}}^{B_j}T_{j+1}^{n+1}\\&+\overbrace{\left(\frac{1}{2\Delta r^2}-\frac{1}{4\Delta r}\frac{1}{r_j}-\frac{1}{4{r_j}^2}\right)}^{C_j}u_{j-1}^{n+1}\overbrace{-\left(\frac{1}{\Delta r^2}+\frac{\rho\,(1+\nu)(1-2\nu)}{\mathrm{E}\,(1-\nu)}\frac{1}{\Delta t^2}\right)}^{D_j}u_j^{n+1}\\&+\overbrace{\left(\frac{1}{2\Delta r^2}+\frac{1}{4\Delta r}\frac{1}{r_j}-\frac{1}{4{r_j}^2}\right)}^{E_j}u_{j+1}^{n+1}\\&=\overbrace{-\frac{\alpha(1+\nu)}{(1-\nu)}\frac{1}{4\Delta r}}^{-A_j}T_{j-1}^{n}+\overbrace{\frac{\alpha(1+\nu)}{(1-\nu)}\frac{1}{4\Delta r}}^{-B_j}T_{j+1}^{n}\overbrace{-\left(\frac{1}{2\Delta r^2}-\frac{1}{4\Delta r}\frac{1}{r_j}-\frac{1}{4{r_j}^2}\right)}^{-C_j}u_{j-1}^{n}\\&+\overbrace{\left(\frac{1}{\Delta r^2}-\frac{\rho\,(1+\nu)(1-2\nu)}{\mathrm{E}\,(1-\nu)}\frac{2}{\Delta t^2}\right)}^{Q_j}u_j^{n}\overbrace{-\left(\frac{1}{2\Delta r^2}+\frac{1}{4\Delta r}\frac{1}{r_j}-\frac{1}{4{r_j}^2}\right)}^{-E_j}u_{j+1}^{n}\\&+\overbrace{\frac{\rho\,(1+\nu)(1-2\nu)}{\mathrm{E}\,(1-\nu)}\frac{1}{\Delta t^2}}^{F_j}u_j^{n-1}\end{aligned}$$

$$A_j T_{j-1}^{n+1} + B_j T_{j+1}^{n+1} + C_j u_{j-1}^{n+1} + D_j u_j^{n+1} + E_j u_{j+1}^{n+1} = -A_j T_{j-1}^{n} - B_j T_{j+1}^{n} - C_j u_{j-1}^{n} + Q_j u_j^{n} - E_j u_{j+1}^{n} + F_j u_j^{n-1} \quad \text{(A.1)}$$

(2) For the radial temperature equation $T(r,t)$ (2-9):

$$\frac{\partial^2 T}{\partial r^2} + \left(\frac{1}{r} + \frac{1}{k}\frac{dk}{dr}\right)\frac{\partial T}{\partial r} - \frac{1}{\alpha^*}\frac{\partial T}{\partial t} - \frac{T_o E\alpha}{k(1-2\nu)}\left(\frac{\partial^2 u_r}{\partial t \partial r} + \frac{1}{r}\frac{\partial u_r}{\partial t}\right) = 0$$

Applying the Crank-Nicolson finite difference discretization,

$$\begin{aligned}
\Longrightarrow \frac{1}{2\Delta r^2}&\left(T_{j+1}^{n+1} - 2T_j^{n+1} + T_{j-1}^{n+1} + T_{j+1}^{n} - 2T_j^{n} + T_{j-1}^{n}\right) \\
&+ \left(\frac{1}{r_j} + \frac{1}{k_j}\frac{k_{j+1}-k_{j-1}}{2\Delta r}\right)\frac{1}{4\Delta r}\left(T_{j+1}^{n+1} - T_{j-1}^{n+1} + T_{j+1}^{n} - T_{j-1}^{n}\right) \\
&- \frac{1}{\alpha^*}\frac{1}{\Delta t}\left(T_j^{n+1} - T_j^{n}\right) \\
&- \frac{T_o E\alpha}{k(1-2\nu)}\frac{1}{\Delta t}\left[\frac{1}{2\Delta r}\left(u_{j+1}^{n+1} - u_{j-1}^{n+1} - u_{j+1}^{n} + u_{j-1}^{n}\right) + \frac{1}{r_j}\left(u_j^{n+1} - u_j^{n}\right)\right] = 0
\end{aligned}$$

After rearranging next time step (n+1) in one side and the previous time steps in the other sides the heat equation will be,

$$\begin{aligned}
&\overbrace{\left(\frac{1}{2\Delta r^2} - Z_j\frac{1}{4\Delta r}\right)}^{G_j} T_{j-1}^{n+1} \overbrace{- \left(\frac{1}{\Delta r^2} + \frac{1}{\alpha^*}\frac{1}{\Delta t}\right)}^{H_j} T_j^{n+1} + \overbrace{\left(\frac{1}{2\Delta r^2} + Z_j\frac{1}{4\Delta r}\right)}^{I_j} T_{j+1}^{n+1} \\
&+ \overbrace{\left(\frac{T_o E\alpha}{k(1-2\nu)}\frac{1}{2\Delta r\Delta t}\right)}^{K_j} u_{j-1}^{n+1} \overbrace{- \left(\frac{T_o E\alpha}{k(1-2\nu)}\frac{1}{\Delta t}\frac{1}{r_j}\right)}^{L_j} u_j^{n+1} \overbrace{- \left(\frac{T_o E\alpha}{k(1-2\nu)}\frac{1}{2\Delta r\Delta t}\right)}^{M_j} u_{j+1}^{n+1} \\
&= \overbrace{- \left(\frac{1}{2\Delta r^2} - Z_j\frac{1}{4\Delta r}\right)}^{-G_j} T_{j-1}^{n} + \overbrace{\left(\frac{1}{\Delta r^2} - \frac{1}{\alpha^*\Delta t}\right)}^{P_j} T_j^{n} - \overbrace{\left(\frac{1}{2\Delta r^2} + Z_j\frac{1}{4\Delta r}\right)}^{-I_j} T_{j+1}^{n} \\
&+ \overbrace{\left(\frac{T_o E\alpha}{k(1-2\nu)}\frac{1}{2\Delta r\Delta t}\right)}^{K_j} u_{j-1}^{n} \overbrace{- \left(\frac{T_o E\alpha}{k(1-2\nu)}\frac{1}{\Delta t}\frac{1}{r_j}\right)}^{L_j} u_j^{n} \overbrace{- \left(\frac{T_o E\alpha}{k(1-2\nu)}\frac{1}{2\Delta r\Delta t}\right)}^{M_j} u_{j+1}^{n} \\
&G_j T_{j-1}^{n+1} + H_j T_j^{n+1} + I_j T_{j+1}^{n+1} + K_j u_{j-1}^{n+1} + L_j u_j^{n+1} + M_j u_{j+1}^{n+1} \\
&\qquad = -G_j T_{j-1}^{n+1} + P_j T_j^{n+1} - I_j T_{j+1}^{n+1} + K_j u_{j-1}^{n+1} + L_j u_j^{n+1} + M_j u_{j+1}^{n+1} \qquad \text{(A.2)}
\end{aligned}$$

where, $Z_j = \frac{1}{k_j}\frac{k_{j+1}-k_{j-1}}{2\Delta r}$

(3) Internal boundary Conditions Eq. (2-10):

(3.1) Thermal boundary Conditions:

$$\mathrm{w}_{21}\frac{T_2 + T_0}{2} + \mathrm{w}_{22}\frac{T_2 - T_0}{2\Delta r} = \mathrm{f}_2(t)$$

$$T_0 = Y_1 - Y_2 T_2 \qquad \text{(A.3)}$$

(3.2) Mechanical boundary Conditions:

$$\mathrm{w}_{11}\frac{u_2+u_0}{2R_i}+\mathrm{w}_{12}\frac{u_2-u_0}{2\Delta r}+\mathrm{w}_{13}\frac{T_2+T_0}{2}=\mathrm{f}_1(t)$$

Using the expression of T_0 from Eq.(A.3)

$$u_0=X_1+X_2T_2-X_3u_2 \tag{A.4}$$

where, $X_1=(2\mathrm{f}_1(t)-\mathrm{w}_{13}Y_1)/\left(\frac{\mathrm{w}_{11}}{R_i}-\frac{\mathrm{w}_{12}}{\Delta r}\right), X_2=\mathrm{w}_{13}(Y_2-1)/\left(\frac{\mathrm{w}_{11}}{R_i}-\frac{\mathrm{w}_{12}}{\Delta r}\right), X_3=\left(\frac{\mathrm{w}_{11}}{R_i}+\frac{\mathrm{w}_{12}}{\Delta r}\right)/\left(\frac{\mathrm{w}_{11}}{R_i}-\frac{\mathrm{w}_{12}}{\Delta r}\right),\ Y_1=2\mathrm{f}_2(t)/\left(\mathrm{w}_{21}-\frac{\mathrm{w}_{22}}{\Delta r}\right),\ Y_2=\left(\mathrm{w}_{21}+\frac{\mathrm{w}_{22}}{\Delta r}\right)/\left(\mathrm{w}_{21}-\frac{\mathrm{w}_{22}}{\Delta r}\right),$

(4) External boundary Conditions Eq. (2-11):

(4.1) Thermal boundary Conditions:

$$\mathrm{w}_{41}\frac{T_{M+1}+T_{M-1}}{2}+\mathrm{w}_{42}\frac{T_{M+1}-T_{M-1}}{2\Delta r}=\mathrm{f}_4(t)$$

$$T_{M+1}=Y_3-Y_4T_{M-1} \tag{A.5}$$

(4.2) Mechanical boundary Conditions:

$$\mathrm{w}_{31}\frac{u_{M+1}+u_{M-1}}{2R_o}+\mathrm{w}_{32}\frac{u_{M+1}-u_{M-1}}{2\Delta r}+\mathrm{w}_{33}\frac{T_{M+1}+T_{M-1}}{2}=\mathrm{f}_3(t)$$

Using the expression of $\boldsymbol{T_{M+1}}$ from Eq. (A.5)

$$u_{M+1}=X_4+X_5T_{M-1}-X_6u_{M-1} \tag{A.6}$$

where, $X_5=\mathrm{w}_{33}(Y_4-1)/\left(\frac{\mathrm{w}_{31}}{R_o}+\frac{\mathrm{w}_{32}}{\Delta r}\right), X_6=\left(\frac{\mathrm{w}_{31}}{R_o}-\frac{\mathrm{w}_{32}}{\Delta r}\right)/\left(\frac{\mathrm{w}_{31}}{R_o}+\frac{\mathrm{w}_{32}}{\Delta r}\right),\ Y_3=2\mathrm{f}_4(t)/\left(\mathrm{w}_{41}+\frac{\mathrm{w}_{42}}{\Delta r}\right),\ Y_4=\left(\mathrm{w}_{41}-\frac{\mathrm{w}_{42}}{\Delta r}\right)/\left(\mathrm{w}_{41}+\frac{\mathrm{w}_{42}}{\Delta r}\right),\ and\ X_4=(2\mathrm{f}_3(t)-\mathrm{w}_{33}Y_3)/\left(\frac{\mathrm{w}_{31}}{R_o}+\frac{\mathrm{w}_{32}}{\Delta r}\right)$

The boundary conditions are applied for left side (next time step) and right side (current step) for the displacement and radial Eqs. (A.1) and (A.2), as follows.

a) At the thick-walled cylinder inner surface R_i (j=1):

For the radial displacement,

$$A_1T_0^{n+1}+B_1T_2^{n+1}+C_1u_0^{n+1}+D_1u_1^{n+1}+E_1u_2^{n+1}$$
$$=-A_1T_0^{n}-B_1T_2^{n}-C_1u_0^{n}+Q_1u_1^{n}-E_1u_2^{n}+F_1u_1^{n-1}$$

Substituting by the expressions of $\boldsymbol{T_0}$ ***and*** $\boldsymbol{u_0}$ using Eqs (A.3) and (A.4) into the radial displacement equation and heat equation at the inner surface of the thick-walled cylinder can be written as,

$$\overbrace{(B_1 + C_1X_2 - A_1Y_2)}^{b_1} T_2^{n+1} + \overbrace{D_1}^{d_1} u_1^{n+1} + \overbrace{(E_1 - C_1X_3)}^{e_1} u_2^{n+1}$$
$$= -(B_1 + C_1X_2 - A_1Y_2)T_2^n + \overbrace{Q_1}^{q_1} u_1^n - (E_1 - C_1X_3)u_2^n$$
$$+ \overbrace{F_1u_1^{n-1} - C_1(\mathrm{X}_1^{n+1} + \mathrm{X}_1^n) - A_1(\mathrm{Y}_1^{n+1} + \mathrm{Y}_1^n)}^{f_1}$$

$$b_1T_2^{n+1} + d_1u_1^{n+1} + e_1u_2^{n+1} = -b_1T_2^n + q_1u_1^n - e_1u_2^n + f_1 \qquad \text{(A.7)}$$

Similarly for heat equation,

$$\Rightarrow \overbrace{H_1}^{h_1} T_1^{n+1} + \overbrace{(I_1 - G_1Y_2 + K_1X_2)}^{i_1} T_2^{n+1} + \overbrace{L_1}^{l_1} u_1^{n+1} + \overbrace{(M_1 - K_1X_3)}^{m_1} u_2^{n+1}$$
$$= \overbrace{P_1}^{p_1} T_1^n + \overbrace{(G_1Y_2 - I_1 + K_1X_2)}^{v_1} T_2^n + L_1u_1^n$$
$$+ (M_1 - K_1X_3)u_2^n \overbrace{-G_1(\mathrm{Y}_1^{n+1} + \mathrm{Y}_1^n) - K_1(\mathrm{X}_1^{n+1} - \mathrm{X}_1^n)}^{s_1}$$

$$h_1T_1^{n+1} + i_1T_2^{n+1} + l_1u_1^{n+1} + m_1u_2^{n+1}$$
$$= p_1T_1^n + v_1T_2^n + l_1u_1^n + m_1u_2^n + s_1 \qquad \text{(A.8)}$$

b) At the thick-walled cylinder outer surface R_j (j=J):

For the radial displacement,

$$A_JT_{J-1}^{n+1} + B_JT_{J+1}^{n+1} + C_Ju_{J-1}^{n+1} + D_Ju_J^{n+1} + E_Ju_{J+1}^{n+1}$$
$$= -A_JT_{J-1}^n - B_JT_{J+1}^n - C_Ju_{J-1}^n + Q_Ju_J^n - E_Ju_{J+1}^n + F_Ju_J^{n-1}$$

Substituting by the expressions of $\boldsymbol{T_{J+1}}$ ***and*** $\boldsymbol{u_{J+1}}$ using Eqs (A.5) and (A.6) into the radial displacement equation at the outer surface of the thick-walled cylinder can be written as,

$$\overbrace{(A_J - Y_4B_J + X_5E_J)}^{a_J} T_{J-1}^{n+1} + \overbrace{(C_J - X_6E_J)}^{c_J} u_{J-1}^{n+1} + \overbrace{D_J}^{d_J} u_J^{n+1}$$
$$= -(A_J - Y_4B_J + X_5E_J)T_{J-1}^n - (C_J - X_6E_J)u_{J-1}^n + \overbrace{Q_J}^{q_J} u_J^n$$
$$+ \overbrace{F_Ju_J^{n-1} - E_J(\mathrm{X}_4^{n+1} + \mathrm{X}_4^n) - B_J(\mathrm{Y}_3^{n+1} + \mathrm{Y}_3^n)}^{f_J}$$

$$a_JT_{J-1}^{n+1} + c_Ju_{J-1}^{n+1} + d_Ju_J^{n+1} = -a_JT_{J-1}^n - c_Ju_{J-1}^n + q_Ju_J^n + f_J \qquad \text{(A.9)}$$

Similarly for heat equation,

$$\overbrace{\left(G_J - Y_4 I_J + X_5 M_J\right)}^{g_J} T_{J-1}^{n+1} + \overbrace{\widetilde{H_J}}^{h_J} T_J^{n+1} + \overbrace{\left(K_J - X_6 M_J\right)}^{k_J} u_{J-1}^{n+1} + \overbrace{\widetilde{L_J}}^{l_J} u_J^{n+1}$$
$$= \overbrace{\left(Y_4 I_J - G_J + X_5 M_J\right)}^{v_J} T_{J-1}^{n} + \overbrace{\widetilde{P_J}}^{p_J} T_J^{n} + \left(K_J - X_6 M_J\right) u_{J-1}^{n}$$
$$+ L_J u_J^n \overbrace{-I_J(\mathrm{Y}_3^{n+1} + \mathrm{Y}_3^n) - M_J(\mathrm{X}_4^{n+1} - \mathrm{X}_4^n)}^{s_J}$$

$$g_J T_{J-1}^{n+1} + h_J T_J^{n+1} + k_J u_{J-1}^{n+1} + l_J u_J^{n+1} = v_J T_{J-1}^{n} + p_J T_J^{n} + k_J u_{J-1}^{n} + l_J u_J^{n} + s_J \quad \text{(A.10)}$$

The radial displacement and heat equations can be written in a very convenient structure written in a matrix form, as:

$$\begin{bmatrix} [\boldsymbol{A}]_{JxJ} & [\boldsymbol{B}]_{JxJ} \\ [\boldsymbol{E}]_{JxJ} & [\boldsymbol{F}]_{JxJ} \end{bmatrix}_{2Jx2J} \begin{Bmatrix} \{v_1\}_{Jx1} \\ \{v_2\}_{Jx1} \end{Bmatrix}_{2JX1}^{n+1} = \begin{bmatrix} [\boldsymbol{C}]_{JxJ} & [\boldsymbol{D}]_{JxJ} \\ [\boldsymbol{G}]_{JxJ} & [\boldsymbol{H}]_{JxJ} \end{bmatrix}_{2Jx2J} \begin{Bmatrix} \{v_1\}_{Jx1} \\ \{v_2\}_{Jx1} \end{Bmatrix}_{2JX1}^{n} + \begin{Bmatrix} \{c_1\}_{Jx1} \\ \{c_2\}_{Jx1} \end{Bmatrix}$$

Where $[\boldsymbol{X}]$, $\boldsymbol{X} \in \{\boldsymbol{A} - \boldsymbol{H}\}$, $\{v_1\}, \{v_2\}, \{c_1\}, \{c_2\}$ values are as follows:

$$
\begin{bmatrix}
Eq.(4)\begin{cases} R_i \longrightarrow \\ R_o \longrightarrow \end{cases} & \left(\begin{array}{c|c} \overbrace{\begin{matrix} 0 & b_1 & & \\ A_2 & 0 & B_2 & \\ & \ddots & \ddots & \ddots \\ & A_{J-1} & 0 & B_{J-1} \\ & & a_J & 0 \end{matrix}}^{[A]_{JxJ}} & \overbrace{\begin{matrix} d_1 & e_1 & & \\ C_2 & D_2 & E_2 & \\ & \ddots & \ddots & \ddots \\ & C_{J-1} & D_{J-1} & E_{J-1} \\ & & c_J & d_J \end{matrix}}^{[B]_{JxJ}} \end{array}\right)_{Jx2J} \\
Eq.(9)\begin{cases} R_i \longrightarrow \\ R_o \longrightarrow \end{cases} & \left(\begin{array}{c|c} \overbrace{\begin{matrix} h_1 & i_1 & & \\ G_2 & H_2 & I_2 & \\ & \ddots & \ddots & \ddots \\ & G_{J-1} & H_{J-1} & I_{J-1} \\ & & g_J & h_J \end{matrix}}^{[E]_{JxJ}} & \overbrace{\begin{matrix} l_1 & m_1 & & \\ K_2 & L_2 & M_2 & \\ & \ddots & \ddots & \ddots \\ & K_{J-1} & L_{J-1} & M_{J-1} \\ & & k_J & l_J \end{matrix}}^{[F]_{JxJ}} \end{array}\right)_{Jx2J}
\end{bmatrix}_{2Jx2J}
\begin{Bmatrix} \overbrace{\begin{Bmatrix} T_1 \\ T_2 \\ \vdots \\ T_{J-1} \\ T_J \end{Bmatrix}}^{\{v_1\}_{Jx1}} \\ \overbrace{\begin{Bmatrix} u_1 \\ u_2 \\ \vdots \\ u_{J-1} \\ u_J \end{Bmatrix}}^{\{v_2\}_{Jx1}} \end{Bmatrix}_{2JX1}^{n+1} =
$$

$$
= \begin{bmatrix}
\left(\begin{array}{c|c} \overbrace{\begin{matrix} 0 & -b_1 & & \\ -A_2 & 0 & -B_2 & \\ & \ddots & \ddots & \ddots \\ & -A_{J-1} & 0 & -B_{J-1} \\ & & -a_J & 0 \end{matrix}}^{[C]_{JxJ}} & \overbrace{\begin{matrix} q_1 & -e_1 & & \\ -C_2 & Q_2 & -E_2 & \\ & \ddots & \ddots & \ddots \\ & -C_{J-1} & Q_{J-1} & -E_{J-1} \\ & & -c_J & q_J \end{matrix}}^{[D]_{JxJ}} \end{array}\right)_{Jx2J} \\
\left(\begin{array}{c|c} \overbrace{\begin{matrix} p_1 & -i_1 & & \\ -G_2 & P_2 & -I_2 & \\ & \ddots & \ddots & \ddots \\ & -G_{J-1} & P_{J-1} & -I_{J-1} \\ & & -g_J & p_J \end{matrix}}^{[G]_{JxJ}} & \overbrace{\begin{matrix} l_1 & m_1 & & \\ K_2 & L_2 & M_2 & \\ & \ddots & \ddots & \ddots \\ & K_{J-1} & L_{J-1} & M_{J-1} \\ & & k_J & l_J \end{matrix}}^{[H]_{JxJ}} \end{array}\right)_{Jx2J}
\end{bmatrix}_{2Jx2J}
\begin{Bmatrix} \overbrace{\begin{Bmatrix} T_1 \\ T_2 \\ \vdots \\ T_{J-1} \\ T_J \end{Bmatrix}}^{\{v_1\}_{Jx1}} \\ \overbrace{\begin{Bmatrix} u_1 \\ u_2 \\ \vdots \\ u_{J-1} \\ u_J \end{Bmatrix}}^{\{v_2\}_{Jx1}} \end{Bmatrix}_{2JX1}^{n}
$$

$$
+ \begin{Bmatrix} \overbrace{\begin{Bmatrix} f_1 \\ F_2 \\ \vdots \\ F_{J-1} \\ f_J \end{Bmatrix}}^{\{c_1\}_{Jx1}} \\ \overbrace{\begin{Bmatrix} s_1 \\ 0 \\ \vdots \\ 0 \\ s_J \end{Bmatrix}}^{\{c_2\}_{Jx1}} \end{Bmatrix}_{2Jx1}
$$

Appendix B

The corresponding summation of the total strains is purely elastic, according to Eq. (3-9), and using the elastic strain-displacement relationships and total strain-displacement relations in Eqs. (3-1) and (3-2), leads to:

$$\frac{u}{r}+\frac{du}{dr}=\frac{1}{E}(1+\upsilon)(1-2\upsilon)[\sigma_\theta+\sigma_r] \tag{B.1}$$

From equilibrium Eq. (3-3), $(\sigma_\theta+\sigma_r)$ can be written in the differential from as $\frac{1}{r}\frac{d}{dr}(r^2\sigma_r)$. Therefore, Eq. (B.1) can be written as:

$$\frac{1}{r}\frac{d}{dr}(ur)=\frac{1}{E}(1+\upsilon)(1-2\upsilon)\frac{1}{r}\frac{d}{dr}(r^2\sigma_r) \tag{B.2}$$

Through integrating Eq. (B.2), the total hoop strain can be written as:

$$\varepsilon_\theta=\frac{u}{r}=\frac{1}{E}(1+\upsilon)(1-2\upsilon)\sigma_r+\frac{D_2}{r^2} \tag{B.3}$$

As the total hoop strain (ε_θ) is simply equals the summation of the elastic and plastic components of the hoop strain $({\varepsilon_\theta}^e, {\varepsilon_\theta}^p)$, this leads to:

$${\varepsilon_\theta}^p=\varepsilon_\theta-{\varepsilon_\theta}^e$$

Using Eq. (B.4), the elastic strain-displacement relationships in Eq. (3-1), and the von Mises yielding criteria in Eq. (3-5) (to eliminate the radial stress component). The plastic hoop strain as a function of the equivalent stress can be written as:

$${\varepsilon_\theta}^p=\frac{D_2}{r^2}-\frac{2}{\sqrt{3}}\frac{(1-\nu^2)}{E}\sigma_{eq} \tag{B.4}$$

Now, the equivalent plastic strain can be expressed in terms of the equivalent stress using the Prandtl-Reuss Eq. (3-4), as:

$$\varepsilon_{eq}^p=\frac{2}{\sqrt{3}}\frac{D_2}{r^2}-\frac{4}{3}\frac{(1-\nu^2)}{E}\sigma_{eq} \tag{B.5}$$

The integration constant D_2 is determined by considering that at the interference radius R_c (the radius between the elastic and plastic zones), the equivalent stress is equal to the yield strength of the material $\left(\sigma_{eq}=\sigma_Y\right)$ and the equivalent plastic strain is vanished $\left(\varepsilon_{eq}^p=0\right)$. Then the ε_{eq}^p is directly written as:

$$\varepsilon_{eq}^p=A\frac{R_c^2}{r^2}\sigma_Y-A\sigma_{eq};\quad A=\frac{4}{3}\frac{(1-\nu^2)}{E} \tag{B.6}$$

Finally, substitute the plastic equivalent strain Eq. (B.6) into the linear work hardening material model Eq. (3-6), the equivalent stress is expressed in terms radial position as:

$$\sigma_{eq}=\frac{\sigma_Y}{(1+AE_P)}\left(1+AE_P\frac{R_c^2}{r^2}\right) \tag{B.7}$$

Appendix C

The weight matrices denoted as W_{1-4} and the corresponding bias vectors denoted as b_{1-4} in Eq. (2), have the following values corresponding to the stated data in Section 4.

$$\{\sigma_\theta\}_{40\times1} = [W_4]_{40\times25} f_3\{[W_3]_{25\times50} f_2([W_2]_{50\times25} f_1\langle[W_1]_{25\times5}\{x\}_{5\times1} + \{b_1\}_{25\times1}\rangle + \{b_2\}_{50\times1}) + \{b_3\}_{25\times1}\} + \{b_4\}_{40\times1}$$

$[W_1]_{25\times5}$ =					
	0.241	-0.365	-0.376	-0.049	-0.485
	1.398	-1.394	0.073	-0.623	1.204
	-0.624	-0.304	3.220	-0.537	-0.161
	-0.188	-0.699	-1.696	0.010	-0.026
	-0.305	0.305	-1.671	-0.448	-0.123
	3.232	0.654	-0.810	0.193	-0.031
	0.689	-0.932	0.240	0.903	-0.308
	-0.718	-0.059	-0.909	-1.087	-0.364
	-1.657	0.962	-1.720	0.803	0.600
	0.040	1.269	-0.933	0.304	0.623
	4.556	0.791	-1.349	0.734	-0.287
	0.953	-1.277	1.159	0.158	0.121
	-1.770	-0.174	-0.060	1.875	-0.426
	-1.997	0.485	-0.670	-0.620	0.968
	0.860	-1.240	-2.105	-0.111	-0.314
	-0.438	0.472	-0.554	-0.200	-0.968
	2.738	-0.088	0.881	-1.774	-0.222
	-0.490	0.322	2.122	-0.091	0.046
	-1.356	1.224	-0.597	-0.632	-0.915
	0.868	-0.007	0.626	0.420	0.694
	-0.887	-0.316	-0.400	2.218	-0.268
	-0.071	-0.329	-1.594	-0.607	0.398
	0.033	0.464	-1.334	1.235	0.414
	-1.368	-0.417	-0.362	-0.511	0.119
	-1.813	0.666	0.134	-0.405	0.456

$\{b_1\}_{25\times1}$ =	
	0.124
	-0.196
	-1.571
	1.189
	1.200
	-0.530
	-0.072
	1.388
	0.273
	-0.327
	-0.774
	-0.388
	-0.773
	0.401
	0.744
	0.570
	0.424
	-1.023
	0.544
	-0.824
	-0.931
	0.895
	-0.233
	0.124
	-0.196

$\{b_2\}_{50\times1} =$	-0.002
	-0.037
	0.014
	0.025
	-0.035
	0.036
	0.010
	0.015
	0.028
	-0.045
	-0.093
	-0.001
	0.005
	0.024
	-0.040
	-0.006
	0.121
	-0.053
	-0.049
	0.027
	-0.003
	0.155
	-0.056
	0.006
	-0.038
	-0.213
	-0.008
	0.069
	-0.041
	0.011
	0.105
	0.014
	0.315
	-0.004
	-0.018
	0.011
	-0.004
	-0.004
	0.025
	0.009
	-0.024
	0.004
	-0.023
	0.034
	0.101
	-0.010
	0.012
	0.008
	0.020
	0.008

$\{b_3\}_{25\times1} =$	-0.001
	0.000
	0.005
	0.025
	0.013
	0.006
	-0.083
	0.040
	-0.003
	0.009
	-0.168
	0.024
	0.023
	-0.034
	-0.042
	0.109
	-0.094
	-0.027
	0.013
	0.014
	0.062
	0.022
	-0.001
	0.050
	0.023

$[W_2]_{50\times25}$ =

-0.06	-0.08	0.05	-0.09	-0.06	0.06	-0.01	-0.13	0.14	0.11	0.10	-0.03	0.08	0.02	-0.06	-0.08	0.05	-0.09	-0.06	0.06	-0.01	-0.13	0.14	0.11	0.10
-0.05	-0.16	-0.22	0.14	0.23	-0.15	-0.19	0.15	0.43	0.13	-0.08	-0.34	-0.05	0.23	-0.05	-0.16	-0.22	0.14	0.23	-0.15	-0.19	0.15	0.43	0.13	-0.08
0.04	0.38	0.05	0.10	-0.03	-0.30	0.04	0.10	-0.37	-0.25	-0.46	0.23	-0.11	0.10	0.04	0.38	0.05	0.10	-0.03	-0.30	0.04	0.10	-0.37	-0.25	-0.46
0.01	0.29	0.18	0.01	-0.12	-0.32	0.08	-0.03	-0.33	-0.22	-0.47	0.26	0.03	0.07	0.01	0.29	0.18	0.01	-0.12	-0.32	0.08	-0.03	-0.33	-0.22	-0.47
-0.05	-0.16	-0.17	0.03	0.12	0.20	-0.12	0.02	0.38	0.21	0.38	-0.24	-0.06	0.07	-0.05	-0.16	-0.17	0.03	0.12	0.20	-0.12	0.02	0.38	0.21	0.38
-0.04	-0.19	0.29	-0.19	-0.14	0.04	0.03	-0.13	-0.00	0.03	0.02	0.04	0.10	-0.08	-0.04	-0.19	0.29	-0.19	-0.14	0.04	0.03	-0.13	-0.00	0.03	0.02
0.05	-0.13	0.11	0.04	0.04	-0.08	0.02	0.14	-0.10	-0.16	-0.05	-0.01	-0.03	-0.11	0.05	-0.13	0.11	0.04	0.04	-0.08	0.02	0.14	-0.10	-0.16	-0.05
0.27	-0.42	-0.37	0.42	0.38	0.26	0.16	0.46	0.10	-0.23	0.63	-0.20	0.01	-0.44	0.27	-0.42	-0.37	0.42	0.38	0.26	0.16	0.46	0.10	-0.23	0.63
-0.19	-0.21	0.32	-0.32	-0.05	0.20	-0.30	-0.07	0.32	0.34	0.20	-0.22	-0.25	0.24	-0.19	-0.21	0.32	-0.32	-0.05	0.20	-0.30	-0.07	0.32	0.34	0.20
0.01	-0.17	-0.06	-0.06	-0.24	-0.07	0.31	-0.42	0.05	-0.02	-0.04	0.12	0.64	-0.27	0.01	-0.17	-0.06	-0.06	-0.24	-0.07	0.31	-0.42	0.05	-0.02	-0.04
-0.09	-0.34	1.46	-0.86	-0.68	0.17	-0.01	-0.27	-0.84	-0.58	0.22	0.24	-0.54	-0.81	-0.09	-0.34	1.46	-0.86	-0.68	0.17	-0.01	-0.27	-0.84	-0.58	0.22
-0.02	0.04	-0.12	0.03	0.02	0.07	-0.00	-0.06	0.15	0.11	0.13	-0.03	0.04	0.06	-0.02	0.04	-0.12	0.03	0.02	0.07	-0.00	-0.06	0.15	0.11	0.13
-0.05	-0.32	0.05	-0.15	-0.05	0.23	0.01	-0.17	0.23	0.20	0.33	-0.12	0.15	-0.10	-0.05	-0.32	0.05	-0.15	-0.05	0.23	0.01	-0.17	0.23	0.20	0.33
0.06	-0.55	-0.09	0.04	0.10	0.26	0.11	-0.01	0.38	0.12	0.52	-0.22	0.28	-0.27	0.06	-0.55	-0.09	0.04	0.10	0.26	0.11	-0.01	0.38	0.12	0.52
-0.10	0.03	-0.14	-0.04	0.09	0.23	-0.23	0.03	0.24	0.25	0.29	-0.19	-0.28	0.21	-0.10	0.03	-0.14	-0.04	0.09	0.23	-0.23	0.03	0.24	0.25	0.29
-0.05	0.35	0.11	-0.08	-0.14	-0.17	-0.02	-0.09	-0.28	-0.06	-0.37	0.21	-0.10	0.16	-0.05	0.35	0.11	-0.08	-0.14	-0.17	-0.02	-0.09	-0.28	-0.06	-0.37
-0.29	-0.12	2.95	-1.72	-1.56	-0.13	0.20	-1.05	-0.90	-0.43	-0.32	0.80	0.24	-0.55	-0.29	-0.12	2.95	-1.72	-1.56	-0.13	0.20	-1.05	-0.90	-0.43	-0.32
-0.00	-0.22	-0.06	-0.06	-0.24	-0.06	0.32	-0.45	0.12	0.00	0.01	0.09	0.67	-0.29	-0.00	-0.22	-0.06	-0.06	-0.24	-0.06	0.32	-0.45	0.12	0.00	0.01
-0.22	0.24	0.16	-0.20	0.00	0.02	-0.44	0.05	0.13	0.24	-0.10	-0.16	-0.56	0.47	-0.22	0.24	0.16	-0.20	0.00	0.02	-0.44	0.05	0.13	0.24	-0.10
0.06	-0.44	0.49	-0.17	-0.04	-0.04	-0.02	0.19	-0.22	-0.26	-0.01	-0.05	-0.12	-0.32	0.06	-0.44	0.49	-0.17	-0.04	-0.04	-0.02	0.19	-0.22	-0.26	-0.01
0.04	0.21	-0.06	0.06	0.06	-0.00	-0.06	0.17	-0.26	-0.09	-0.09	0.08	-0.26	0.07	0.04	0.21	-0.06	0.06	0.06	-0.00	-0.06	0.17	-0.26	-0.09	-0.09
0.19	-0.41	-1.06	0.59	0.88	0.13	-0.29	0.80	0.57	0.45	0.10	-0.56	-0.09	0.50	0.19	-0.41	-1.06	0.59	0.88	0.13	-0.29	0.80	0.57	0.45	0.10
0.09	-0.00	-0.51	0.26	0.16	0.17	0.12	0.02	0.15	0.04	0.34	-0.08	0.15	-0.12	0.09	-0.00	-0.51	0.26	0.16	0.17	0.12	0.02	0.15	0.04	0.34
-0.01	0.12	-0.09	0.05	0.02	-0.01	0.00	-0.03	0.07	0.05	-0.00	0.01	0.02	0.10	-0.01	0.12	-0.09	0.05	0.02	-0.01	0.00	-0.03	0.07	0.05	-0.00
0.02	-0.08	-0.08	0.01	-0.20	-0.11	0.31	-0.37	0.03	-0.07	-0.05	0.14	0.58	-0.25	0.02	-0.08	-0.08	0.01	-0.20	-0.11	0.31	-0.37	0.03	-0.07	-0.05
-0.27	-1.57	-0.42	-0.24	0.31	-1.03	-0.75	0.02	1.09	0.60	-1.91	-1.18	0.83	0.86	-0.27	-1.57	-0.42	-0.24	0.31	-1.03	-0.75	0.02	1.09	0.60	-1.91
0.12	0.41	-0.21	0.18	-0.14	-0.28	0.35	-0.17	-0.46	-0.29	-0.42	0.41	0.35	-0.14	0.12	0.41	-0.21	0.18	-0.14	-0.28	0.35	-0.17	-0.46	-0.29	-0.42
0.20	0.14	0.29	-0.04	-0.00	-0.06	0.09	0.34	-0.88	-0.45	-0.33	0.29	-0.38	-0.33	0.20	0.14	0.29	-0.04	-0.00	-0.06	0.09	0.34	-0.88	-0.45	-0.33
-0.04	-0.45	-0.05	-0.13	0.05	0.42	-0.09	-0.04	0.30	0.24	0.64	-0.27	-0.03	-0.17	-0.04	-0.45	-0.05	-0.13	0.05	0.42	-0.09	-0.04	0.30	0.24	0.64
0.05	-0.27	0.22	-0.05	0.04	-0.01	-0.04	0.19	-0.15	-0.16	0.01	-0.06	-0.14	-0.17	0.05	-0.27	0.22	-0.05	0.04	-0.01	-0.04	0.19	-0.15	-0.16	0.01
-0.16	-1.19	-0.01	0.16	0.43	-1.49	-0.44	0.38	1.54	0.26	-1.75	-0.91	1.07	1.06	-0.16	-1.19	-0.01	0.16	0.43	-1.49	-0.44	0.38	1.54	0.26	-1.75
0.01	-0.22	0.28	-0.09	-0.02	-0.03	-0.04	0.10	-0.08	-0.11	-0.01	-0.04	-0.10	-0.12	0.01	-0.22	0.28	-0.09	-0.02	-0.03	-0.04	0.10	-0.08	-0.11	-0.01
0.33	-0.05	-0.11	0.55	0.73	-0.78	-0.21	1.20	-0.48	-0.30	-1.43	0.02	-0.38	0.65	0.33	-0.05	-0.11	0.55	0.73	-0.78	-0.21	1.20	-0.48	-0.30	-1.43
0.04	0.07	-0.17	0.14	0.12	0.01	-0.02	0.14	-0.01	-0.03	0.04	-0.03	-0.09	0.05	0.04	0.07	-0.17	0.14	0.12	0.01	-0.02	0.14	-0.01	-0.03	0.04
-0.17	-0.10	0.10	-0.24	-0.05	0.20	-0.23	-0.14	0.30	0.34	0.20	-0.18	-0.17	0.21	-0.17	-0.10	0.10	-0.24	-0.05	0.20	-0.23	-0.14	0.30	0.34	0.20
-0.03	-0.13	0.10	0.00	0.17	0.07	-0.24	0.28	0.14	0.05	0.14	-0.21	-0.36	0.13	-0.03	-0.13	0.10	0.00	0.17	0.07	-0.24	0.28	0.14	0.05	0.14
-0.04	0.32	-0.25	0.09	-0.02	-0.02	0.06	-0.17	0.12	0.14	-0.03	0.09	0.12	0.20	-0.04	0.32	-0.25	0.09	-0.02	-0.02	0.06	-0.17	0.12	0.14	-0.03
-0.01	-0.01	-0.07	0.06	0.13	0.08	-0.12	0.14	0.13	0.06	0.16	-0.12	-0.19	0.09	-0.01	-0.01	-0.07	0.06	0.13	0.08	-0.12	0.14	0.13	0.06	0.16
0.21	0.03	-0.24	0.30	0.06	-0.18	0.34	0.10	-0.31	-0.33	-0.16	0.21	0.33	-0.28	0.21	0.03	-0.24	0.30	0.06	-0.18	0.34	0.10	-0.31	-0.33	-0.16
0.05	0.16	0.02	0.03	-0.20	-0.23	0.31	-0.26	-0.21	-0.18	-0.28	0.29	0.45	-0.18	0.05	0.16	0.02	0.03	-0.20	-0.23	0.31	-0.26	-0.21	-0.18	-0.28
0.16	-0.23	-0.39	0.21	0.03	0.17	0.35	-0.12	0.07	-0.06	0.38	0.03	0.50	-0.40	0.16	-0.23	-0.39	0.21	0.03	0.17	0.35	-0.12	0.07	-0.06	0.38
0.04	0.15	-0.07	0.10	0.04	-0.09	0.03	0.09	-0.14	-0.10	-0.12	0.07	-0.05	0.03	0.04	0.15	-0.07	0.10	0.04	-0.09	0.03	0.09	-0.14	-0.10	-0.12
-0.01	-0.15	0.69	0.52	0.08	-2.49	-0.09	0.63	0.36	-0.82	-3.22	0.07	1.06	1.15	-0.01	-0.15	0.69	0.52	0.08	-2.49	-0.09	0.63	0.36	-0.82	-3.22
-0.15	-0.24	0.32	-0.27	-0.01	0.17	-0.27	-0.01	0.29	0.28	0.18	-0.21	-0.25	0.19	-0.15	-0.24	0.32	-0.27	-0.01	0.17	-0.27	-0.01	0.29	0.28	0.18
0.07	0.30	0.05	0.12	0.34	0.12	-0.34	0.63	-0.28	-0.05	0.02	-0.06	-0.87	0.30	0.07	0.30	0.05	0.12	0.34	0.12	-0.34	0.63	-0.28	-0.05	0.02
-0.08	0.01	0.18	-0.22	-0.34	-0.12	0.21	-0.49	-0.04	0.05	-0.23	0.21	0.50	-0.09	-0.08	0.01	0.18	-0.22	-0.34	-0.12	0.21	-0.49	-0.04	0.05	-0.23
0.02	0.04	0.05	0.03	0.02	-0.08	-0.00	0.09	-0.10	-0.09	-0.09	0.03	-0.06	0.01	0.02	0.04	0.05	0.03	0.02	-0.08	-0.00	0.09	-0.10	-0.09	-0.09
-0.01	-0.00	0.03	0.00	0.01	-0.00	-0.02	0.03	0.01	-0.00	0.02	-0.01	-0.04	0.02	-0.01	-0.00	0.03	0.00	0.01	-0.00	-0.02	0.03	0.01	-0.00	0.02
0.06	-0.13	0.23	-0.04	-0.01	-0.13	0.01	0.15	-0.24	-0.21	-0.18	0.04	-0.07	-0.13	0.06	-0.13	0.23	-0.04	-0.01	-0.13	0.01	0.15	-0.24	-0.21	-0.18
-0.02	-0.40	0.38	-0.24	-0.32	-0.38	0.25	-0.41	0.02	-0.11	-0.49	0.08	0.74	-0.19	-0.02	-0.40	0.38	-0.24	-0.32	-0.38	0.25	-0.41	0.02	-0.11	-0.49

$[W_3]^T_{25\times50} =$

0.11	0.13	0.01	-0.09	0.01	0.02	-0.03	0.04	0.19	0.10	0.07	0.03	-0.10	-0.15	-0.06	-0.08	0.19	-0.06	0.02	0.02	-0.03	0.02	0.08	0.15	-0.03
-0.02	-0.11	0.10	0.04	-0.10	0.25	0.04	-0.19	0.57	0.24	-0.14	0.05	-0.06	0.14	-0.30	0.08	-0.04	0.19	-0.08	-0.02	-0.31	-0.08	0.03	-0.18	0.05
-0.14	-0.11	-0.02	0.23	0.30	-0.04	-0.03	0.17	-0.59	-0.29	-0.22	0.11	0.24	0.10	-0.20	0.38	-0.35	-0.02	0.06	0.01	0.02	0.09	-0.11	0.02	0.14
-0.04	0.01	-0.03	0.16	0.26	-0.08	0.09	0.25	-0.55	-0.30	-0.10	0.17	0.17	-0.03	-0.25	0.32	-0.12	-0.08	0.08	0.02	-0.07	0.13	-0.08	0.17	0.14
0.05	0.01	0.05	-0.11	-0.08	0.13	-0.22	-0.17	0.61	0.30	-0.08	-0.09	-0.14	-0.00	0.08	-0.15	0.05	0.05	-0.06	-0.00	0.02	-0.09	0.08	-0.09	-0.08
0.18	0.29	-0.02	-0.15	-0.06	-0.10	0.27	0.13	0.11	-0.04	0.21	0.06	-0.13	-0.24	-0.04	-0.07	0.11	-0.11	0.02	0.01	-0.03	0.08	0.06	0.26	-0.03
-0.03	0.01	-0.00	0.01	-0.22	-0.07	0.23	-0.00	-0.02	-0.10	-0.11	0.00	0.04	0.02	0.08	0.12	-0.23	0.03	-0.03	-0.01	-0.02	0.01	-0.07	-0.03	0.03
-0.25	-0.38	0.02	-0.01	-1.03	-0.06	0.08	-0.38	0.43	0.21	-0.63	-0.29	0.09	0.23	0.71	-0.08	-0.16	0.24	-0.15	-0.04	0.20	-0.21	-0.13	-0.53	-0.11
0.32	0.51	0.03	-0.29	0.33	0.03	0.18	0.02	0.78	0.14	0.34	0.01	-0.33	-0.18	-0.22	-0.19	-0.32	-0.06	-0.05	-0.00	-0.07	0.03	0.16	0.24	-0.10
0.08	-0.03	-0.02	-0.02	-0.41	-0.03	-0.01	0.16	-0.35	0.12	0.04	0.12	-0.04	-0.33	0.01	-0.17	1.17	-0.15	0.11	0.05	-0.02	0.05	0.10	0.27	-0.01
0.25	0.74	0.05	-0.17	-0.33	-0.26	1.49	0.18	1.27	-0.26	1.21	-0.11	-0.11	0.12	-0.86	-0.01	-0.42	0.18	-0.03	-0.01	0.16	0.08	0.05	0.02	-0.05
0.01	-0.02	0.01	-0.01	0.03	0.07	-0.23	-0.02	0.14	0.15	-0.10	-0.01	-0.03	-0.04	-0.03	-0.04	0.15	-0.02	0.01	0.02	0.05	-0.02	0.06	0.02	-0.02
0.18	0.20	0.01	-0.21	-0.23	-0.01	0.05	-0.02	0.42	0.22	0.15	-0.03	-0.22	-0.23	0.10	-0.26	0.32	-0.08	-0.01	0.01	0.05	-0.01	0.13	0.16	-0.11
0.10	-0.06	0.04	-0.21	-0.77	0.03	0.07	-0.19	0.59	0.32	-0.05	-0.08	-0.20	-0.16	0.37	-0.31	0.44	0.03	-0.08	-0.01	0.02	-0.09	0.07	-0.02	-0.12
0.06	0.08	0.03	-0.09	0.29	0.11	-0.30	-0.12	0.50	0.21	-0.00	-0.10	-0.12	0.04	-0.04	-0.10	-0.29	0.02	-0.04	0.00	0.13	-0.06	0.09	-0.05	-0.08
0.02	0.07	-0.03	0.11	0.51	-0.04	-0.10	0.24	-0.43	-0.21	0.01	0.11	0.10	-0.05	-0.29	0.22	-0.21	-0.12	0.10	0.03	0.08	0.12	-0.00	0.20	0.08
-0.21	3.57	0.02	0.15	-0.09	-0.07	-0.38	-0.01	0.27	0.14	2.96	-0.02	0.18	0.13	-0.16	0.07	0.11	0.09	0.02	0.01	-0.21	-0.06	-0.04	-0.24	0.01
0.10	-0.01	-0.01	-0.04	-0.47	-0.02	0.00	0.13	-0.27	0.16	0.05	0.12	-0.06	-0.35	0.04	-0.21	1.26	-0.15	0.11	0.05	-0.08	0.04	0.11	0.27	-0.02
0.14	0.29	0.04	-0.06	0.87	0.11	-0.11	0.03	0.50	-0.00	0.20	0.00	-0.11	0.09	-0.45	0.10	-0.81	0.01	-0.03	-0.00	0.02	0.03	0.08	0.06	0.00
0.09	0.27	-0.01	-0.15	-0.46	-0.22	0.82	0.02	0.22	-0.24	0.22	-0.03	-0.07	-0.04	0.13	0.06	-0.47	0.05	-0.08	-0.04	-0.05	0.05	-0.10	0.03	-0.02
-0.10	-0.07	-0.02	0.09	0.25	-0.04	-0.15	0.02	-0.24	-0.13	-0.18	-0.06	0.12	0.13	0.02	0.18	-0.56	0.00	0.00	-0.00	0.28	0.01	-0.06	-0.07	0.02
-0.07	-1.03	0.03	-0.08	-0.29	0.32	-0.72	-0.53	-0.45	0.18	-1.10	-0.11	-0.13	0.06	1.10	-0.07	-0.63	0.01	-0.19	-0.05	0.12	-0.13	-0.09	-0.17	-0.03
-0.17	-0.36	0.02	0.08	-0.33	0.11	-0.51	-0.19	0.03	0.29	-0.42	-0.13	0.07	0.08	0.29	-0.09	0.37	0.06	-0.01	0.01	0.20	-0.12	0.02	-0.23	-0.05
-0.01	-0.05	0.01	0.05	0.11	0.06	-0.21	0.01	0.02	0.07	-0.13	0.02	0.02	-0.01	-0.09	0.05	0.06	-0.02	0.02	0.01	0.02	0.00	0.03	0.02	0.02
0.04	-0.09	-0.02	0.03	-0.36	-0.03	-0.04	0.17	-0.33	0.08	-0.06	0.13	0.02	-0.28	0.00	-0.09	1.07	-0.14	0.11	0.04	-0.07	0.06	0.07	0.23	0.02
0.11	-0.68	0.14	0.11	0.18	0.39	0.85	-0.25	-1.85	0.57	1.00	-0.34	-0.09	0.23	-1.83	-1.04	0.43	0.40	0.29	0.10	1.40	-0.19	0.57	-0.23	-0.18
-0.19	-0.34	-0.06	0.30	0.01	-0.07	-0.28	0.26	-1.07	-0.20	-0.34	0.14	0.31	-0.07	-0.08	0.26	0.48	-0.14	0.17	0.05	0.20	0.10	-0.06	0.13	0.14
-0.15	-0.20	-0.06	0.17	-0.03	-0.24	0.62	0.08	-0.96	-0.59	-0.07	-0.12	0.27	0.25	0.02	0.36	-0.99	0.05	0.01	-0.03	0.42	0.09	-0.22	-0.11	0.08
0.15	0.22	0.01	-0.28	-0.35	-0.02	-0.02	-0.17	0.73	0.30	0.09	-0.17	-0.26	-0.14	0.36	-0.35	0.07	-0.01	-0.08	-0.01	0.14	-0.09	0.10	-0.01	-0.18
0.03	0.10	-0.01	-0.08	-0.27	-0.13	0.44	-0.03	0.11	-0.15	0.03	-0.04	-0.03	0.02	0.14	0.07	-0.47	0.04	-0.07	-0.03	0.05	0.02	-0.08	-0.03	-0.01
-0.50	0.06	0.15	0.71	-0.17	-0.01	0.58	0.26	0.31	0.00	-0.28	0.38	0.70	0.23	-1.00	0.92	0.20	0.33	0.10	0.07	-2.28	0.06	-0.24	-0.44	0.43
0.07	0.20	-0.01	-0.08	-0.17	-0.11	0.40	0.03	0.15	-0.13	0.09	0.00	-0.05	-0.04	0.05	0.06	-0.33	0.00	-0.04	-0.02	-0.02	0.04	-0.05	0.05	-0.00
-0.18	-0.62	0.03	0.27	0.42	0.18	-0.01	-0.06	-1.71	-0.22	-0.24	0.11	0.20	0.25	-0.17	0.30	-2.54	0.08	0.07	0.00	0.38	0.01	-0.09	-0.06	0.16
-0.10	-0.16	0.01	0.07	-0.01	0.05	-0.18	-0.08	-0.00	0.04	-0.25	-0.04	0.07	0.11	0.05	0.10	-0.22	0.05	-0.02	-0.00	0.10	-0.04	-0.03	-0.13	0.02
0.24	0.31	0.03	-0.21	0.33	0.08	-0.06	0.00	0.59	0.21	0.26	-0.00	-0.26	-0.16	-0.20	-0.19	-0.10	-0.07	-0.01	0.01	0.00	0.01	0.17	0.20	-0.09
0.01	0.13	0.04	-0.07	0.05	0.03	0.12	-0.15	0.51	0.02	-0.05	-0.09	-0.07	0.15	0.03	0.07	-0.72	0.11	-0.11	-0.03	0.00	-0.05	-0.04	-0.15	-0.02
-0.04	-0.12	0.01	0.11	0.30	0.13	-0.55	0.07	-0.15	0.16	-0.20	0.06	0.06	-0.05	-0.17	0.04	0.34	-0.08	0.08	0.04	0.05	0.01	0.08	0.08	0.03
-0.02	-0.01	0.02	-0.01	0.05	0.06	-0.12	-0.10	0.31	0.09	-0.14	-0.06	-0.02	0.08	0.03	0.03	-0.31	0.05	-0.05	-0.01	0.06	-0.05	0.00	-0.10	-0.02
-0.24	-0.41	-0.03	0.22	-0.49	-0.08	-0.09	0.02	-0.69	-0.11	-0.47	0.02	0.26	0.05	0.28	0.20	0.25	0.01	0.04	0.01	0.16	-0.00	-0.14	-0.12	0.08
-0.03	-0.08	-0.04	0.13	-0.15	-0.09	-0.02	0.26	-0.64	-0.12	-0.12	0.17	0.14	-0.21	-0.08	0.10	0.73	-0.15	0.14	0.04	-0.04	0.11	-0.00	0.24	0.09
-0.11	-0.27	-0.02	0.02	-0.75	-0.01	-0.30	-0.09	-0.20	0.24	-0.34	-0.06	0.04	-0.14	0.48	-0.18	0.87	-0.04	0.03	0.02	0.12	-0.08	0.01	-0.07	-0.06
-0.09	-0.11	-0.01	0.11	0.07	0.00	-0.12	0.03	-0.22	-0.07	-0.21	0.02	0.11	0.07	-0.02	0.17	-0.18	0.00	0.02	0.00	0.09	0.01	-0.05	-0.04	0.05
0.26	-0.02	-0.06	-0.66	-0.18	-0.39	-0.90	-0.09	0.35	-0.14	0.04	-0.19	-0.22	-0.23	1.77	-1.07	-0.56	-0.15	-0.28	-0.09	2.65	-0.03	-0.10	0.20	-0.35
0.27	0.44	0.03	-0.26	0.21	0.02	0.22	-0.01	0.73	0.11	0.30	-0.01	-0.29	-0.14	-0.15	-0.14	-0.38	-0.03	-0.06	-0.01	-0.07	0.02	0.12	0.18	-0.08
-0.14	0.00	0.00	0.08	0.55	-0.03	-0.12	-0.09	0.34	-0.18	-0.33	-0.11	0.12	0.37	-0.02	0.41	-1.83	0.13	-0.11	-0.04	0.21	-0.03	-0.15	-0.29	0.03
0.18	0.23	-0.03	-0.03	-0.03	-0.05	0.05	0.30	-0.39	-0.01	0.30	0.21	-0.06	-0.39	-0.24	-0.09	0.94	-0.23	0.15	0.06	-0.08	0.14	0.13	0.46	0.03
-0.03	-0.00	-0.00	0.05	0.02	-0.03	0.05	0.03	-0.08	-0.08	-0.11	0.02	0.06	0.03	-0.02	0.13	-0.22	0.00	0.00	-0.00	0.03	0.02	-0.04	0.00	0.04
0.01	0.04	0.00	-0.00	0.02	-0.00	-0.01	0.02	0.07	0.00	-0.06	0.01	-0.00	-0.02	-0.02	0.05	-0.10	-0.01	-0.00	0.00	0.03	0.01	0.00	0.02	0.00
-0.00	0.07	-0.02	-0.01	-0.17	-0.13	0.39	0.05	-0.15	-0.22	-0.02	0.02	0.04	0.01	0.05	0.16	-0.40	0.01	-0.03	-0.02	0.01	0.05	-0.09	0.03	0.04
0.08	0.21	0.01	0.07	-0.55	-0.02	0.41	0.22	-0.76	-0.03	0.32	0.26	0.02	-0.36	-0.13	-0.06	1.00	-0.13	0.15	0.05	-0.34	0.13	0.05	0.35	0.11